Optical Diagnostics of Reactive Flows

Application of 3D emission tomography and laser-based methods

Sanned, David

2023

Document Version:
Publisher's PDF, also known as Version of record

[Link to publication]

Total number of authors:
1

LUND UNIVERSITY

PO Box 117
221 00 Lund
+46 46-222 00 00

Optical Diagnostics of Reactive Flows

Application of 3D emission tomography and laser-based methods

DAVID SANNED
DEPARTMENT OF PHYSICS | FACULTY OF ENGINEERING | LUND UNIVERSITY

Optical Diagnostics of Reactive Flows

Application of 3D emission tomography
and laser-based methods

By David Sanned

LUND
UNIVERSITY

DOCTORAL DISSERTATION

Doctoral dissertation for the degree of Doctor of Philosophy (PhD) at the Faculty of Engineering at Lund University to be publicly defended on 24th of November 2023 at 09.15 in the Rydberg Hall, Department of Physics, Professorsgatan 1, Lund.

Faculty opponent

Dr. Aaron Skiba

Organization: LUND UNIVERSITY

Document name: DOCTORAL DISSERTATION   **Date of issue:** 2023-10-31

Author: David Sanned   **Sponsoring organization:**

Title and subtitle: Optical Diagnostics of Reactive Flows

Application of 3D emission tomography and laser based-methods

Abstract:

Nowadays, numerous specialized systems, ranging from electronics to energy production processes can be found both in science and industry. However due to their specialized nature they often exhibit high sensitivity to intrusive measurements, which can potentially perturb the sought-after characteristics or quantity and consequently compromise overall accuracy. In these scenarios, optical measurements can offer a potential solution owing to their often-non-intrusive nature based on the photon-in-photon-out concept. The application of different optical techniques does not only enable the achievement of non-invasiveness but can also offer the capability to measure and quantify observable phenomena that may not always be accessible through conventional probing methods.

The work within this thesis centers on three-dimensional (3D) emission tomography and its application in the context of reactive flows. Many reactive flows, such as those found in combustion processes, inherently exhibit three-dimensional characteristics, necessitating measurement techniques that can perform measurements in all three dimensions. The work covers the fundamentals of emission tomography and showcases the techniques application in both combustion and plasma research.

The application in combustion diagnostics yielded volumetric flame reconstructions and investigated the use of arbitrary sensor positions to overcome limitations in optical access. Similarly, plasma diagnostic application allowed for volumetric gliding arc reconstructions facilitating quantification of 3D characteristics such as 3D arc length and arc volume. This is followed by stereoscopic 3D particle tracking applied in iron combustion, looking at particle micro explosions and 3D velocities.

Subsequently, various optical laser-based techniques applied in the work within this thesis are presented, each accompanied by an experimental application. These techniques include particle image velocimetry (PIV), for flow field analysis, and laser-induced fluorescence (LIF), for hydroxide (OH) analysis, both applied in a model lab-scale gas turbine swirl combustor. Additionally, fluorescence lifetime imaging (FLI) was utilized in gliding arc plasma investigations in combination with 3D emission tomography to investigate OH fluorescence lifetimes.

Investigation of potential nanoparticle release during iron combustion was carried out using shadowgraphy, enabling the visualization of release trails produced by individual iron particles. Moreover, work within phosphor thermometry was performed, investigating the impact of PMT non-linearity effects on measured phosphorescence lifetimes and applied for in-situ surface temperature measurements on heat exchanger pipes in a multi-fuel Stirling engine.

Signature   Date: 2023-10-05

Optical Diagnostics of Reactive Flows

Application of 3D emission tomography
and laser-based methods

By David Sanned

LUND
UNIVERSITY

Faculty of Engineering, Department of Physics

Media-Tryck is a Nordic Swan Ecolabel
certified provider of printed material.
Read more about our environmental
work at www.mediatryck.lu.se

MADE IN SWEDEN

"There must be some way out of here" said the joker to the thief
-Bob Dylan

Table of Contents

Abstract

Nowadays, numerous specialized systems, ranging from electronics to energy production processes can be found both in science and industry. However due to their specialized nature they often exhibit high sensitivity to intrusive measurements, which can potentially perturb the sought-after characteristics or quantity and consequently compromise overall accuracy. In these scenarios, optical measurements can offer a potential solution owing to their often-non-intrusive nature based on the photon-in-photon-out concept. The application of different optical techniques does not only enable the achievement of non-invasiveness but can also offer the capability to measure and quantify observable phenomena that may not always be accessible through conventional probing methods.

The work within this thesis centers on three-dimensional (3D) emission tomography and its application in the context of reactive flows. Many reactive flows, such as those found in combustion processes, inherently exhibit three-dimensional characteristics, benefitting from measurement techniques that can perform measurements in all three dimensions. The work covers the fundamentals of emission tomography and showcases the techniques application in both combustion and plasma research.

The application in combustion diagnostics yielded volumetric flame reconstructions and investigated the use of arbitrary sensor positions to overcome limitations in optical access. Similarly, plasma diagnostic application allowed for volumetric gliding arc reconstructions facilitating quantification of 3D characteristics such as 3D arc length and arc volume. This is followed by stereoscopic 3D particle tracking applied in iron combustion, looking at particle micro explosions and 3D velocities.

Subsequently, various optical laser-based techniques applied in the work within this thesis are presented, each accompanied by an experimental application. These techniques include particle image velocimetry (PIV), for flow field analysis, and laser-induced fluorescence (LIF), for hydroxide (OH) analysis, both applied in a model lab-scale gas turbine swirl combustor. Additionally, fluorescence lifetime imaging (FLI) was utilized in gliding arc plasma investigations in combination with 3D emission tomography to investigate OH fluorescence lifetimes.

Investigation of potential nanoparticle release during iron combustion was carried out using shadowgraphy, enabling the visualization of release trails produced by individual iron particles. Moreover, work within phosphor thermometry was performed, investigating the impact of PMT non-linearity effects on measured phosphorescence lifetimes and applied for in-situ surface temperature measurements on heat exchanger pipes in a multi-fuel Stirling engine.

Populärvetenskaplig Sammanfattning

Tack vare en mängd olika teknologiska framsteg under de senaste decennierna så finns det idag många system och enheter, särskilt inom industrin, som kan utföra väldigt specialiserade uppgifter till en nivå som tidigare inte vart tänkbart. Exempel på användning av specialiserade system kan vara inom produktion av elektronik eller mat, där den automatiserade tillverkningen beröringsfritt behöver kvalitetstesta de producerade produkterna för att inte skada eller kontaminera dem. Likaså finns det system i den medicinska vården där man behöver utföra tester av prov utan att skada eller påverka provet. Även inom energisektorn finns det många avancerade system till exempel gasturbiner för energiproduktion, där det är mycket svårtillgängligt att utföra tester och mätningar för att få fram viktiga faktorer som temperaturer och utsläpp för att förbättra effektiviteten och miljön.

I dessa fall behövs mättekniker som kan komma åt att mäta i svårtillgängliga miljöer samt få ut bra mätdata med hög kvalitet utan att själv påverka systemet och det som ska mätas. Optiska mättekniker kan ibland erbjuda en potentiell lösning då man mäter med hjälp av fotoner vilket gör teknikerna oftast beröringsfria. Förutom sin icke-invasivitet kan optiska tekniker erbjuda möjligheter att mäta och kvantifiera fenomen som kanske inte alltid är tillgängliga genom mer konventionella mätmetoder.

Då många av fenomenen man studerar är tre-dimensionella (3D) i sin natur så har en ökning skett av optiska tekniker som kan göra mätningar i alla tre dimensionerna.

Denna ökning ses inte bara inom olika forskningsområden utan också på den kommersiella marknaden så som i spel och filmindustrin där optisk skanning används för att skapa digitala 3D modeller av landskap eller för att detektera rörelsemönster hos människor och djur.

I forskningsområden relaterade till energiproduktion och reaktiva flöden, såsom eld eller plasmabågar, kan 3D mätningar göras med hjälp av olika metoder. Arbetet i den här avhandlingen, med avseende på 3D mätningar i reaktiva flöden, fokuserar främst på emissions-tomografi. Emissions-tomografi är en flexibel och icke-invasiv optisk teknik som genom mätningar av ljusutsläppet från reaktiva flöden (eldsflammor och plasmabågar) kan återskapa det ursprungliga mätobjektet i 3D.

Denna typ av forskning är viktig då förbränningsprocesser fortfarande bidrar betydligt till den globala energiförsörjningen. Fram till 2020 rapporterade internationella energiorganet International Energy Agency (IEA) att dessa processer stod för ungefär 90% av den globala energiförsörjningen, där 80% av bränslet härstammade från fossila källor [1]. Dessutom visar IEA:s prognoser från 2022 att trots en minskad användning av fossila bränslen förväntas dessa resurser behålla en betydande närvaro i den globala energiförsörjningen och uppgå till cirka 75% år 2030 och 60% år 2050 [2]. Detta tillsammans med nya utmaningar i kombination

med införandet av nya förnybara bränslen visar på behovet av ytterligare effektivisering och utsläppsreducering.

Denna avhandling beskriver grunderna för applicerad 3D emissions-tomografi med särskilt fokus på den specifika metod som har utvecklats och tillämpats i den presenterade forskningen. Detta inkluderar information och detaljer kopplat till själva rekonstruktionsprocessen samt olika tillämpning där särskilt fokus har lagts vid teknikens effektivitet för visualisering av reaktiva flöden. Därefter presenteras akademiska bidrag rörande 3D-mätningar där utveckling och tillämpning av framför allt emissions-tomografi i studier av reaktiva flöden visas. Sådana exempel inkluderar 3D mätningar av olika typer av eldsflammor, plasmabågar och brinnande järnpartiklar vid metallförbränning.

Därefter introduceras andra laserbaserade optiska tekniker som används i denna avhandling, dessa tekniker användes för punktmätningar och två-dimensionella (2D) mätningar. De första laserbaserade teknikerna som beskrivs är Particle Image Velocimetry (PIV) och Laser Inducerad Flourescens (LIF) som båda tillämpades i en laboratoriemodell av en gasturbin för energiproduktion. Därefter presenteras mätningar och avbildning av flourescenslivstid (FLI) i en plasmabåge för att undersöka den fluorescerande tiden av molekyler i plasman, denna teknik kombineras också med 3D emissions-tomografi.

Vidare presenteras Shadowgraphy studier som undersöker om det skapas nanopartiklar vid förbränning av järnpulver. Nanopartiklar är viktigt att undvika i metallförbränning för att bland annat möjliggöra bättre bränsleåtervinning. Sist men inte minst gjordes yttemperaturmätningar med hjälp av fosfortermometri på en värmeväxlare i en Stirlingmotor. Mätningar utfördes både vid diesel och vätgaskörning. Även undersökningar på inverkan av icke-linjära effekter i detektorer på uppmätta temperaturer när de används i fosfortermometri presenteras.

List of Papers

I. **D. Sanned**, S. Nilsson, A. Roth, E. Berrocal, A. Ehn, and M. Richter, "3D-tomographic reconstruction of gliding arc plasma," *Applied Physics Letters,* vol. 123, no. 7, p. 071104, 2023.

II. **D. Sanned**, J. Lindström, A. Roth, M. Aldén, and M. Richter, "Arbitrary position 3D tomography for practical application in combustion diagnostics," *Measurement Science and Technology,* vol. 33, no. 12, p. 125206, 2022/09/28 2022.

III. S. Li, **D. Sanned**, J. Huang, E. Berrocal, W. Cai, M. Aldén, M. Richter, and Z. Li, "Stereoscopic high-speed imaging of iron microexplosions and nanoparticle-release," *Optics Express,* vol. 29, no. 21, pp. 34465-34476, 2021/10/11 2021.

IV. H. Feuk, **D. Sanned**, M. Richter, and M. Aldén, "Sources of error for single-shot PMT-based phosphor thermometry in harsh conditions," *Measurement Science and Technology,* vol. 32, no. 8, p. 084003, 2021/05/13 2021.

V. F. Pignatelli, S. Derafshzan, **D. Sanned**, N. Papafilippou, R. Z. Szasz, M. A. Chishty, P. Petersson, X. S. Bai, R. Gebart, A. Ehn, M. Richter, D. Lörstad, and A. A. Subash, "Effect of CO2 dilution on structures of premixed syngas/air flames in a gas turbine model combustor," *Combustion and Flame,* vol. 255, p. 112912, 2023/09/01/ 2023.

VI. S. Nilsson, **D. Sanned**, A. Roth, E. Berrocal, M. Richter, and A. Ehn, " Fluorescence Lifetime Imaging of OH Radical in Volumetrically Resolved Gliding Arc Plasma," *Submitted for peer review.*

VII. F. Pignatelli, **D. Sanned**, S. Derafshzan, R. Z. Szasz, X. S. Bai, M. Richter, A. Ehn, D. Lörstad , P. Petersson, and A. A. Subash, "Impact of pilot flame and hydrogen enrichment on turbulent methane/hydrogen/air swirling premixed flames in a model gas turbine combustor," *Submitted for peer review.*

VIII. J. Huang, S. Li, **D. Sanned**, L. Xu, S. Xu, Q. Wang, M. Stiti, Y. Qian, W. Cai, E. Berrocal, M. Richter, M. Aldén, and Z. Li, "A detailed study on the micro-explosion of burning iron particles in hot oxidizing environments," *Combustion and Flame,* vol. 238, p. 111755, 2022/04/01/ 2022.

Author contributions

Paper I: 3D-tomographic reconstruction of gliding arc plasma
D. Sanned, S. Nilsson, A. Roth, E. Berrocal, A. Ehn, and M. Richter
Applied Physics Letters*, vol. 123, no. 7, p. 071104, 2023.

I and Sebastian conducted the experimental activities together. Me, Sebastian, and Adrian performed the data analysis together. I did the data visualization, figures and wrote the manuscript. All co-authors provided feedback on the manuscript.

Paper II: Arbitrary position 3D tomography for practical application in combustion diagnostics
D. Sanned, J. Lindström, A. Roth, M. Aldén, and M. Richter
Measurement Science and Technology, vol. 33, no. 12, p. 125206, 2022/09/28 2022.

I initiated the study. I performed technique development with feedback from Johan Lindström and Adrian Roth. I performed all experimental activities. I conducted the data analysis and did the data visualization and figures. I wrote the manuscript, all co-authors provided feedback on the manuscript.

Paper III: Stereoscopic high-speed imaging of iron microexplosions and nanoparticle-release
S. Li, **D. Sanned**, J. Huang, E. Berrocal, W. Cai, M. Aldén, M. Richter, and Z. Li
Optics Express, vol. 29, no. 21, pp. 34465-34476, 2021/10/11 2021.

I conducted the experimental activities together with Shen Li and Jianqing Huang. Shen Li performed the SEM experiments. I performed the release trail and 3D data analysis. I and Shen Li wrote the manuscript, all co-authors provided feedback on the manuscript.

Paper IV: Sources of error for single-shot PMT-based phosphor thermometry in harsh conditions
H. Feuk, **D. Sanned**, M. Richter, and M. Aldén
Measurement Science and Technology, vol. 32, no. 8, p. 084003, 2021/05/13 2021.

I performed the experimental measurement together with Henrik Feuk. I aided in the analysis and discussion of results. Henrik Feuk wrote the majority of the manuscript. I provided feedback during the writing of the manuscript and contributed to the editing.

Paper V: Effect of CO2 dilution on structures of premixed syngas/air flames in a gas turbine model combustor Combustion and Flame
F. Pignatelli, S. Derafshzan, **D. Sanned**, N. Papafilippou, R. Z. Szasz, M. A. Chishty, P. Petersson, X. S. Bai, R. Gebart, A. Ehn, M. Richter, D. Lörstad, and A. A. Subash

Arman, Francesco, Saeed, and I conducted the experimental activities together. Francesco performed the majority of the data analysis with input from co-authors. I aided in the analysis and visualization of the PIV results. Francesco wrote the manuscript, I and all co-authors provided feedback on the manuscript.

Paper VI: Fluorescence Lifetime Imaging of OH Radical in Volumetrically Resolved Gliding Arc Plasma
S. Nilsson, **D. Sanned**, A. Roth, E. Berrocal, M. Richter, and A. Ehn
Manuscript submitted for peer review.

Sebastian and I conducted the experimental activities together. Sebastian, Adrian, and I performed the data analysis together, where I focused on tomography. Sebastian did the data visualization, figures and wrote the manuscript. I provided feedback during the writing of the manuscript and contributed to the editing. All co-authors provided feedback on the manuscript.

Paper VII: Impact of pilot flame and hydrogen enrichment on turbulent methane/hydrogen/air swirling premixed flames in a model gas turbine combustor
F. Pignatelli, **D. Sanned**, S. Derafshzan, R. Z. Szasz, X. S. Bai, M. Richter, A. Ehn, D. Lörstad, P. Petersson, and A. A. Subash
Manuscript submitted for peer review.

Arman, Francesco, Saeed, and I conducted the experimental activities together. Francesco performed the data analysis with input from co-author and wrote the manuscript. I and all co-authors provided feedback on the manuscript.

Paper VIII: A detailed study on the micro-explosion of burning iron particles in hot oxidizing environments
J. Huang, S. Li, **D. Sanned**, L. Xu, S. Xu, Q. Wang, M. Stiti, Y. Qian, W. Cai, E. Berrocal, M. Richter, M. Aldén, and Z. Li

I, together with Shen Li and Jianqing Huang conducted the experimental activities related to micro explosions and velocity. Jianqing Huang wrote the manuscript. I performed the analysis of the 3D position and velocity measurement data and produced the figure showcasing this. I, together with the other co-authors provided feedback on the manuscript.

1 Introduction

Optical diagnostic methods have found widespread applications across a broad range of fields. One advantage of these methods is their applicability to sensitive systems that necessitate non-intrusive diagnostic approaches or are too large or small for conventional physical probing methods. The optical methods span a range of different techniques and are frequently employed both in industry and scientific research. Common optical measurements conducted in both industrial and scientific fields encompass temperature, molecular compositions in materials or gas flows, size, and length scales, as well as flow field velocities. The versatility of optical techniques allows for a variety of measurement types, including point measurements (0D), one-dimensional (1D), two-dimensional (2D), three-dimensional (3D), and time-resolved analyses, tailored to specific applications and scientific requirements. Recent advancements have allowed for a growing use of 3D optical techniques in entertainment industry for tasks such as optical landscape scanning to create 3D digital models and motion capture. Similarly, these techniques play an essential role in industrial manufacturing settings, enabling tasks like quality control assessments and rapid prototyping of components.

The same increased use of specifically 3D optical techniques can been seen in investigations of thermal energy conversion processes, such as combustion. Given the inherently 3D nature of most reactive flows, it becomes imperative to employ measurement techniques capable of capturing information, such as topology, position, and concentrations across all three dimensions. Obtaining more accurate measurements of reactive flow characteristics can allow for enhancement of energy systems designs through model validation. This validation process is highly important as it can result in improved process efficiency and reduction of harmful emission.

Combustion processes have historically contributed significantly to the global energy supply and still do. As of 2020, the International Energy Agency (IEA) reported that these processes accounted for approximately 90% of the global energy supply, with 80% of the fuel being derived from fossil sources [1]. Moreover, the IEA's 2022 projections demonstrate that despite anticipated reductions in usage of fossil fuel, these resources are believed to retain a substantial presence in the global energy supply, constituting around 75% in 2030 and 60% in 2050 [2]. These figures emphasize the ongoing significance of combustion within the global energy landscape, even in the context of achieving a net-zero emission scenario by 2050 [3]. This together with new

challenges in combination with implementation of novel renewable fuels underscores the pressing need for further advancements in combustion efficiency and emission reduction. Figure 1.1 illustrates the current and predicted future fossil fuel demand based on the Stated Policies Scenario (STEPS) [4].
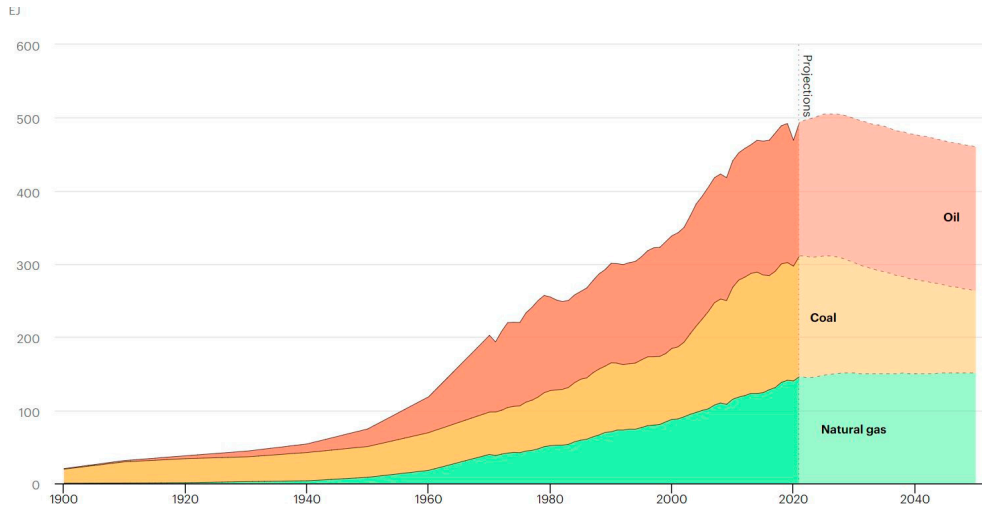
Figure 1.1: Current global and predicted fossil fuel demand following the IEA STEPS Scenario [2].

Volumetric measurements of reacting flows, such as combustion, can be accomplished through different methods. One approach involves the utilization of laser sheet scanning, wherein a probing laser sheet is systematically moved through the investigated volume. Subsequently, 2D images of each laser sheet are combined to generate comprehensive 3D information. The work in this thesis, with regards to volumetric reactive flow measurements, focus mainly on emission tomography which represent an alternative avenue for achieving 3D imaging. Emission tomography is a versatile and non-intrusive technique that utilizes the isotropic light emission inherent to various processes within a reacting flow to reconstruct back the original luminescence field from objects such as flames or plasma arcs.

This thesis work describes the fundamentals of 3D emission tomography, with a primary focus on the specific method developed and applied in the presented research. This includes details about the projection model, the reconstruction process, and its application, particularly emphasizing its efficacy in visualizing reactive flows. Subsequently, academic contributions regarding 3D measurements are presented, showcasing development and application of emission tomography in studying reactive flows. Application includes premixed CH_4/air Bunsen flames and ethanol (C_2H_5OH) diffusion pool flames, wherein the impact of diverse camera placements to facilitate optical access limitations was studied. Additionally, the versatility of emission tomography is demonstrated in the characterization of gliding

arc plasmas within varying flow fields, enabling measurements like 3D arc length and arc volume. This is then followed by stereoscopic 3D particle tracking velocimetry (PTV), as applied to burning iron particles in metal combustion, looking at particle microexplosions and velocities.

Subsequently, different 0D and 2D laser-based techniques, employed in this thesis are introduced. Accompanying each technique description is an experimental application, showcasing its practical implementation. Particle image velocimetry (PIV) which investigate flow fields, and laser-induced fluorescence (LIF), here targeted at hydroxyl (OH) analysis, were both employed in a lab-scale model gas turbine swirl combustor. This application aimed to investigate CO_2 dilution effects in syngas (comprising H_2, CO, and CH) combustion. Similarly, close to lean blow-off (LBO) conditions during hydrogen enrichment of CH_4 combustion were also investigated. Furthermore, fluorescence lifetime imaging (FLI) was applied in gliding arc plasma investigations of OH fluorescence lifetimes in combination with 3D emission tomography.

The potential release of nanoparticles during iron powder combustion was studied using shadowgraphy, enabling the visualization of release trails from individual iron particles. The creation of nanoparticles is important when it comes to energy carrier recyclability and health aspects.

Temperature measurements using phosphor thermometry was applied in a multi-fuel Stirling engine. This involved in-situ surface temperature measurements of heat exchanger pipes during diesel and O_2 combustion, as well as H_2 and O_2 combustion. Additionally, work investigating the impact of PMT non-linearity effects on measured phosphorescence lifetimes and in turn temperature was performed.

2 Tomography

Originally, tomography emerged as a technique primarily utilized in medical diagnostics, often coupled with X-ray observations, and underwent significant scientific advancements during the 1970s and 80s. Over time, technique refinement and improvement have led to its expansion into various scientific and engineering fields [5]. Presently, the application of tomography has extended beyond X-ray detection and now encompass a range of measurement techniques including ultrasound, laser radiation, chemiluminescence, and more. This versatility has facilitated a wide variety of applications.

Tomography allows the measurement of both external and internal geometries, making it an ideal technique for industrial quality control of intricate products featuring inaccessible internal features. This characteristic is particularly valuable for non-destructive testing. As a result, tomography finds widespread application in various fields, including manufacturing, inhomogeneous materials, the food industry, and the electronic device industry, serving quality control purposes effectively [6].

Similarly, tomography has found application in other domains where internal investigation are of importance such as seismology, where seismic travel time measurements are used to study the Earth's interior [7], or in magnetic resonance imaging (MRI), which employs non-ionizing radio frequency radiation to detect hydrogen molecules for medical imaging [6].

Central to the work in this thesis is the increased use of 3D emission tomographic techniques to investigate reacting and non-reacting flows [8]. The decreasing costs of computational resources and measurement apparatus have enabled a significant expansion of tomographic volumetric measurements, especially in combustion diagnostics. Here emission tomography leverages the emitted light from a reacting flow process to reconstruct back the complete luminescence field spatially, such as a flame or plasma arc, using path-integrated data from multiple acquired images of the same object. Its inherent flexibility and non-intrusive nature make it compatible with complementary measurement techniques like laser absorption spectroscopy [9, 10], particle image velocimetry [11], schlieren techniques [12, 13], and volumetric laser-induced fluorescence [14-16].

Thus, tomography can provide enhancements in 3D measurements, focusing on attributes such as position, topology, species distribution, acoustic oscillations, soot

formation, and soot volume fraction, for not just laminar but also unsteady and turbulent flows. These comprehensive measurements yield essential insights for refining models and validating numerical simulations [14, 17].

2.1   Inverse problem

Tomography revolves around the process of reconstructing and retrieving information from an object under investigation, utilizing a series of measurements conducted on the object. These measurements can come in multiple forms, encompassing aspects like light intensity, absorption, diffraction, and many others. Such methodology, involving the retrieval of information about a physical object or system through the analysis of observed measurements, is termed an inverse problem. At the heart of the tomographic technique lies precisely such an inverse problem, where a forward measurement model transforms a 2D field into 1D projection measurements and subsequently, this forward model can be inverted to recover the original 2D information. Figure 2.1 shows this concept in a 2D context, portraying two objects subject to a forward model that generates 1D projection views via line integrals. The recovered 2D information can then later be stacked allowing the acquisition of 3D information. However, this procedure can also be directly performed in 3D with a forward model that then converts 3D fields into 2D image projections. Inversion of such a forward model will allows recovery of 3D information from the image projections.
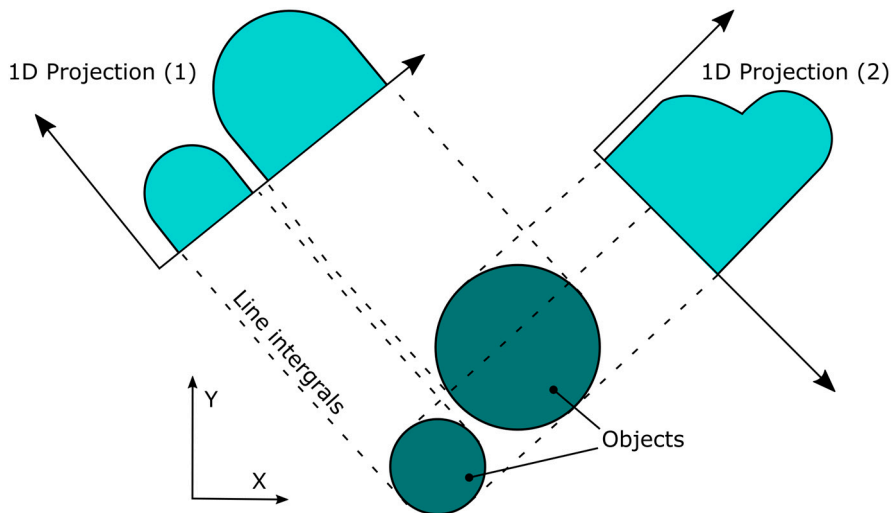

Figure 2.1: Illustration of how two-dimensional objects are measured using a forward model based on line integrals, creating 1D projection views.

The work within this thesis applied emission-based tomography that utilize 2D images of emitted light from a transparent object such as flames to reconstruct back the full 3D luminescence field. The three key steps of this process are illustrated in Figure 2.2.
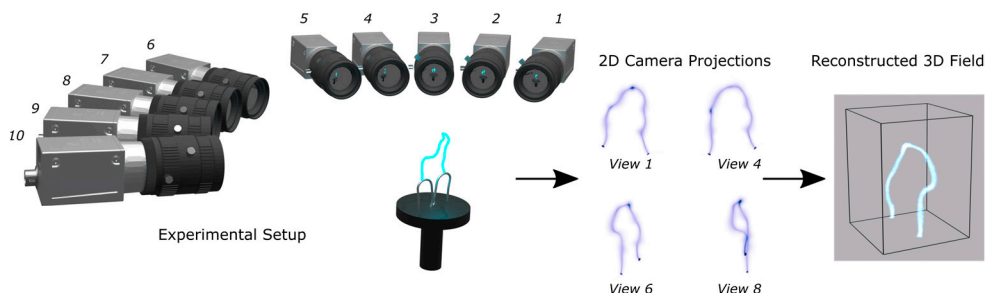

Figure 2.2: Depiction of the three key steps in emission based tomography. Experimental setup yeilding multiple 2D camera projections which thereafter are used to reconstruct the 3D luminecence field.

In reactive flows such as these, light is emitted from excited species partaking in the reactions giving rise to spontaneous emission trough chemiluminescence, incandescence emitted from hot soot particles or species responding to laser induced fluorescence. Emission of this type is generally isotropic, giving rise to light emission in all directions. The combination of such isotropic emission and object transparency allows images to be considered 2D line-of-sight projections where a measured pixel intensity results from an integral through the investigated volume. These inverse tomographic problems typically result in a linear system of the form

$$A\boldsymbol{x} = b \qquad (1)$$

where A is a projection matrix containing all linear voxel projections and $\boldsymbol{x}$ is the unknown field vector of the probed volume and b is the projection measurements. The availability of multiple projection views is an important feature when performing tomographic measurements of this type as each image is a line-of-sight integrated projection convolving features of the object. To allow extraction of such aspects and features, projection views from various perspectives are needed, often acquired using multiple cameras, fiber bundle or view splitters.

Numerous inverse problems, including the tomographic reconstruction of reactive flows, are notorious for being ill-posed. Depending on the ratio between the number of optical projection measurements (rows in the projection matrix A) and reconstructed measurement points (columns in A) the resulting linear system Equation (1) can be either underdetermined or overdetermined. In the case of a underdetermined system of equations, the number of variables is greater than the number of equations thus enabling an infinite set of solutions [18]. Conversely, in

overdetermined scenarios, the variables are fewer than the equations, possibly leading to a solution that does not precisely satisfy all equations. A simple illustration of optimal solutions is presented in Figure 2.3.

(a)   (b)
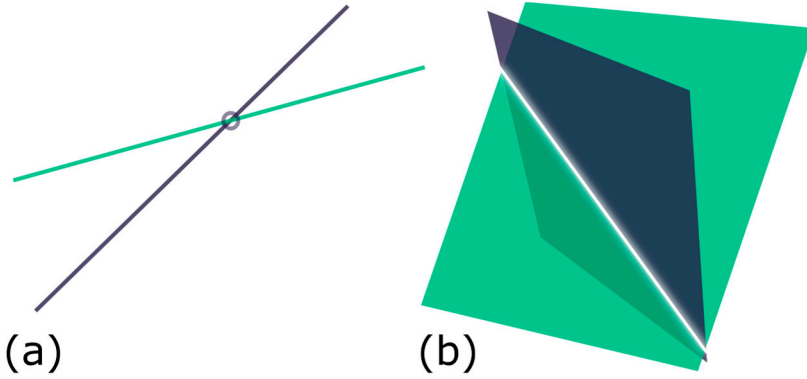
Figure 2.3: (a) Illustration of optimal solution in a two-dimensional space between two lines is the intersection point. (b) In three-dimensional space the intersection between two planes is a line, illustrating that finding the optimum on this line would require more information (such as a third plane).

Furthermore, practical tomography problems such as flame emission tomography also tends to be ill-conditioned due to volume discretization and effects from such errors will be amplified in the measurements b [12, 19]. Hence, introducing a priori information and boundary conditions into the reconstruction process, thereby rendering the problem more well-posed, restricts potential solutions to those yielding more accurate estimates of the reconstructed field. Smoothing, based on the assumption of a continuous field, can help in reactive flow reconstructions. However, one needs to be aware that reconstructions can in some cases suffer a trade of between resolving finer spatial features or having a more overall correct field estimate, especially in complex field, such as turbulent flows. Problems such as this could be solved by adding more projection views or applying more flexible smoothing models that allow for varying dependence strength between voxels [20], but might increase complexity of the reconstruction due to additional parameter estimation controlling the non-stationary smoothing.

2.2   Reconstruction model

The tomographic method applied to reconstruct 3D luminosity fields within the work of this thesis involved simultaneous acquisition of multiple 2D view projection measurements q from the probed 3D volume Ω, which contains a transparent object emitting light such as a flame or plasma discharge. Each view projection q

corresponds to a CMOS camera image captured from a distinct viewing angle and position surrounding the investigated volume Ω. These images consist of multiple $(m \times n)$ pixel projections p, as depicted in Figure 2.4. For computational efficiency, the continuous probed volume Ω is discretized into N_v voxels.

Probe volume Ω, discretized into N_v voxels

Pixel p

View q

Camera image with $m \times n$ pixels

Single voxel v
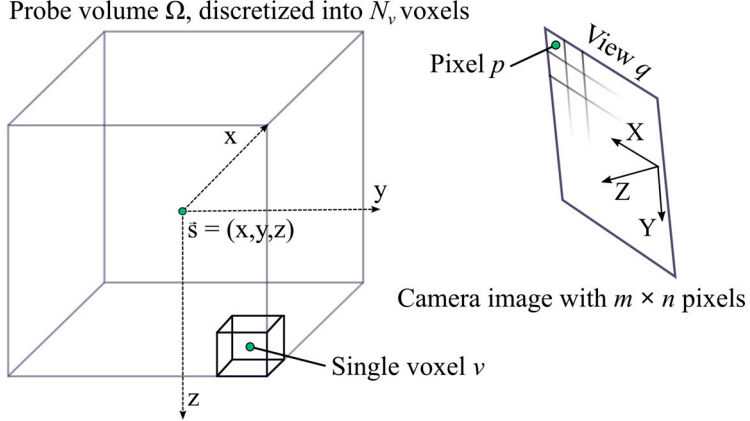
$\vec{s} = (x, y, z)$

Figure 2.4: Illustration of 2D view projection and probe volume Ω, discretized into N_v voxels.

Investigated luminosity intensity within the volume Ω at positions denoted as $\vec{s} = (x, y, z)$ can be characterized as a continuous field $f(\vec{s})$. This distribution of luminosity intensity can then be mapped to the projection measurements qp, acquired by the optical setup at a specific view and pixel, through a Fredholm integral equation of the first kind , which is defined by the radiative transfer equation (RTE) [19],

$$b_{qp} = \int_{qp} f(\vec{s}) \, dA \tag{2}$$

where $f(\vec{s})$ is the continuous flame field and b_{qp} is a projection measurement from view q and pixel p. Furthermore, a smoothness requirement, corresponding to a smoothing spline [21, 22] was applied in this work to the luminosity fields based on the assumption of the fields investigated being continuous. This was done by introducing a penalty term as

$$\iint \left(\Delta f(\vec{s}) \right)^2 \, d(\vec{s}) = \iint \left[\left(\frac{\partial^2}{\partial^2 x} + \frac{\partial^2}{\partial^2 y} + \frac{\partial^2}{\partial^2 z} \right) \right]^2 f(\vec{s}). \tag{3}$$

This term minimizes the second derivative throughout the flame field, resulting in more continuous solutions, which align with the typical physical expectations in the studied flows. Additionally, it helps alleviate any negative effects due to an ill-posed problem. Thereafter, the final reconstruction problem can be stated as

$$\arg\min_{f(\vec{s})} \sum_{qp} \left(b_{qp} - \int_{qp} f(\vec{s}) \, dA \right) + \lambda \iint \left(\Delta f(\vec{s}) \right)^2 d(\vec{s}) \tag{4}$$

where, λ is the weight of the penalty term and the minimization finds the reconstruction that best balances the observational measurements against the applied smoothness requirement. The parameter λ must be selected such that the smoothness requirement does not overshadow information contained in real measurement data while still improving on the spatial smoothness of the estimated solution. The parameter λ can either be estimated or found empirically by trial and error [23], throughout this thesis λ was selected empirically for each individual application.

The previously mentioned discretization of the investigated luminosity field into a voxel scalar field allows the RTE integral, depicted in Equation (2), to be approximated as a finite sum over the luminosity field. This yields a projection approximation of each intensity measurement b_{qp} as

$$b_{qp} = \sum_{v=1}^{N_v} w_{qpv} x_v \tag{5}$$

where x_v is a voxel, w_{qpv} that voxel's contribution to the projection qp and b_{qpv} defines a line-of-sight projection of said voxel v. Furthermore, the smoothness prior described in Equation (3) can be represented by a sparse discrete Laplacian matrix as follows:

$$Q = \begin{aligned} \left(d_{zz} \otimes I_{n_y} \right) \otimes I_{n_x} + \left(I_{n_z} \otimes d_{yy} \right) \otimes I_{n_x} + \\ + \left(I_{n_z} \otimes I_{n_y} \right) \otimes d_{xx} \end{aligned} \tag{6}$$

where d_{xx}, d_{yy} and d_{zz} are discrete one-dimensional (1D) Laplacians. I_{n_x}, I_{n_y} and I_{n_z} are identity matrices of applicable size to the volume size. Here each 1D discrete Laplacian applies a homogenous Dirichlet boundary condition which results in a final 3D discrete Laplacian with homogenous Dirichlet boundary condition for all boundaries specified by

$$f(x, y, z) = 0, \qquad (x, y, z) \in \vartheta\Omega \tag{7}$$

with $\vartheta\Omega$ depicting the boundary of the volume. The continuous problem can then be reformulated in a discretized structure [24] in the following way

$$\arg\min_{x} \|b - Ax\|_2^2 + \lambda x^T Q x. \tag{8}$$

Here A is the projection matrix containing all linear voxel projections and x is the unknown field vector i.e., the discretization of $f(\vec{s})$. The discretized reconstruction

of the probed volume Ω is then acquired from the solution to the minimization problem in Equation (8), which is a quadratic problem with known closed form solution[22]:

$$\boldsymbol{x}_{min} = (\lambda Q + A^T A)^{-1} A^T b \tag{9}$$

which optimally can be solved by using iterative methods [25] to avoid costly matrix operations.

It is possible to interpret the later part of the discretized system in Equation (8) in an alternative way such as a prior latent Gaussian field [26] with a precision matrix given by Q for the volume Ω and observations given by the discretized integral Equation (5). This results in the model

$$b = A\boldsymbol{x} + \varepsilon, \quad \varepsilon \in N(0, I\sigma_\varepsilon^2), \quad \boldsymbol{x} \in N(0, (\tau Q)^{-1}) \tag{10}$$

where ε are independent observational and discretization errors with variance σ_ε for each pixel and τ is a smoothness weight. The posterior for the discretized volume $\boldsymbol{x}$ conditional on observations and parameters is then given by

$$[\boldsymbol{x}|b, \sigma_\varepsilon^2, \tau] = N \begin{pmatrix} (\tau Q + A^T A\sigma_\varepsilon^{-2})^{-1} A^T b \, \sigma_\varepsilon^{-2} \\ , (\tau Q + A^T A\sigma_\varepsilon^{-2})^{-1} \end{pmatrix} \tag{11}$$

with the conditional expectation being

$$E(\boldsymbol{x}|b, \sigma_\varepsilon^2, \tau) = (\sigma_\varepsilon^2 \tau Q + A^T A)^{-1} A^T b. \tag{12}$$

By setting $\sigma_\varepsilon^2 \tau = \lambda$ this formulation becomes identical to the optimal reconstruction in Equation (9). Note that individual values of τ and σ_ε^2 are not needed for the reconstruction. One advantage of formulating the model in a statistical framework is the ability to quantify the uncertainty in the reconstruction as

$$V(\boldsymbol{x}|b, \sigma_\varepsilon^2, \tau) = (\tau Q + A^T A\sigma_\varepsilon^{-2})^{-1}. \tag{13}$$

This variance requires individual values for τ and σ_ε^2 and computation of the needed matrix inverse is likely to require iterative and/or approximate methods [27]. Investigation of the uncertainties of these types of uncertainties was outside of the scope of the work performed within this thesis but the theoretical results and possible numerical methods are provided here for completeness and understanding.

It's worth emphasizing that the projection model, as described in Equation (2) and employed throughout this thesis work, simplifies the RTE by neglecting aspects like scattering, self-absorption, and background intensity. In the context of the emission tomography applications in this thesis, experimental investigations in combustion focused on premixed CH_4/air flames. These types of premixed flames can be considered optically thin, given their minimal soot production, which otherwise could obstruct the emitted light through absorption. Small ethanol pool flames were

also examined and do exhibit low levels of soot production. However, by maintaining a small flame size during experiments and ensuring that the measurement cameras are positioned reasonably close to the probed region, conditions of minimal scattering can be achieved. This results in negligible impacts on the measurements and allows the exclusion of scattering from the model. These assumptions were deemed reasonable also in the plasma applications where the plasma arcs typically had small diameters, approximately 10 mm [28] and can be characterized as optically thin with relative low electron density in the order of 10^{13} cm^{-3} [29]. These conditions, coupled with short distances between cameras and the probed volume, result in minimal scattering effects.

In the flame applications, self-absorption was deemed negligible because the primary emission source was visible chemiluminescence from CH*, mainly from the $A^2\Delta - X^2\Pi$ transition, which is considered to suffer minimal self-absorption effects [30, 31]. Similarly, in the plasma applications, self-absorption could be neglected, as the reconstructed luminosity predominantly originated from excited N_2* emitting in the visible wavelength range, where an assumption of low self-absorption is reasonable.

In contrast, when investigating luminescence coming from excited species like OH, which emit light in the UV region and is known to suffer from self-absorption [30, 32], dismissing effects from self-absorption becomes more complex. Therefore, it is very important to assess each experimental scenario individually. Such evaluation is crucial for gaining insights into both the potential opportunities and, more importantly, recognizing the constraints and limitations of emission tomography within the particular application.

There exists work that has introduced absorption correction into the method of emission tomography based on the Beer-Lambers law [33]. In this approach, following the initial reconstruction of the luminescence field, each voxel x_v is assigned an absorption attenuation coefficient, assumed to be proportionally related to the luminescence distribution. Thereafter the process is iterated with a new luminescence field being calculated including the absorption attenuation until the whole iteration converges. However, this addition can result in heightened computational expense coming from the need for alternating iterations.

2.3   Camera model and Calibration

To obtain the projection matrix A, which contains all linear voxel projections as described in Equation (5), it is necessary to establish a mapping between each 2D camera image measurement b_{qp} and the corresponding voxels within the probed volume Ω. This mapping provides crucial information about camera orientation,

position, and, most importantly, identifies the voxels from which any detected luminosity intensity in a camera pixel originates.

The 3D tomographic and stereoscopic work in this thesis employed an optical model based upon the pinhole camera model initially introduced by Tsai [34] . In essence, a pinhole camera can be described as a screen or box containing a small aperture. Behind this aperture, a sensor is positioned, and any light from the field of view that is transmitted through the hole forms an image on the sensor, effectively generating a 2D image, this process is illustrated in Figure 2.5.
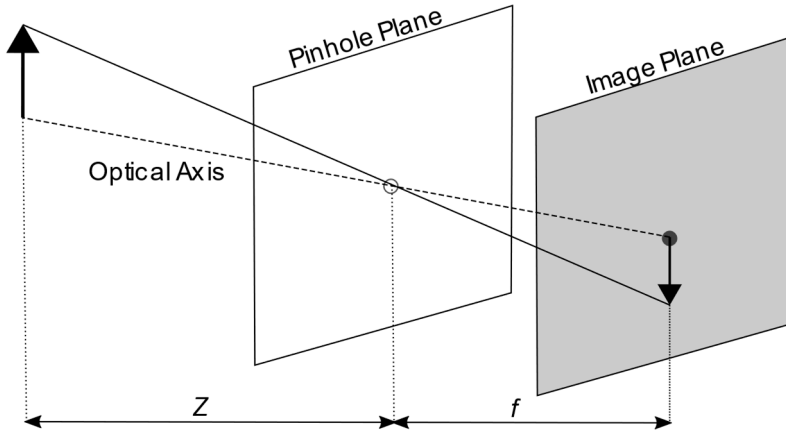

Figure 2.5: Illustration of the pinhole camera model. Light rays going through the aperture in the pinhole plane and thereafter projection onto an image plane forming the image.

This type of pinhole camera can be described using two distinct sets of parameters. First are the intrinsic parameters that describes the internal camera characteristics, like the focal length. Secondly, there are the extrinsic parameters, which encompass external information about the camera, including its position and orientation. With knowledge of all these parameters, it becomes possible to create a mapping that describes the paths taken by light rays as it travels between 3D points in the real world and 2D sensor points in the camera. This model is widely employed in the field of computer vision due to its versatility, as it enables the tracing of camera rays through straightforward matrix transformations [35].

The model involves the computation of two matrices, as outlined in Equation (14). The first matrix K is the intrinsic matrix containing information regarding the camera information. The cameras optical centre is described by the principal point c_x c_y, which determines where the optical axis intersects the 2D image plane and the camera focal length is represented by f_x f_y in pixel units. Finally, α represents the camera axis skew, namely that x- and y- axes are not perpendicular to each other. This skew parameter will be equal to zero for most cameras due to improved

manufacturing rendering this negligible. Nevertheless, in specific and less common applications, such as when capturing an image of another image or enlarging an image using a magnifying lens not perpendicular to the original image plane, the axis skew can be non-zero [35]. The second matrix, denoted as RT, is a rigid transformation matrix that contains the extrinsic parameters. These parameters include the camera rotation r in a 3×3 rotation matrix and translation t in a vector T.

$$K = \begin{pmatrix} f_x & \alpha & c_x \\ 0 & f_y & c_y \\ 0 & 0 & 1 \end{pmatrix}, RT = \begin{pmatrix} r_{1,1} & r_{1,2} & r_{1,3} & t_1 \\ r_{2,1} & r_{2,2} & r_{2,3} & t_2 \\ r_{3,1} & r_{3,2} & r_{3,3} & t_3 \end{pmatrix}. \tag{14}$$

These two matrices facilitate the relationship between a point $(X\ Y\ Z\ 1)$ in 3D space expressed in homogeneous coordinates located in the probed volume Ω and a projection point $(x\ y\ 1)$ in the detection cameras image domain as follows:

$$s(x\ y\ 1)^T = P(X\ Y\ Z\ 1)^T, \qquad P = K(RT), \tag{15}$$

where s is a scaling factor. The imaged points in 3D space are translated and rotated using the extrinsic matrix and are thereafter mapped to image positions in the camera sensor. This approach offers simplicity and great adaptability when it comes to camera placements, particularly useful in situations with restricted optical access.

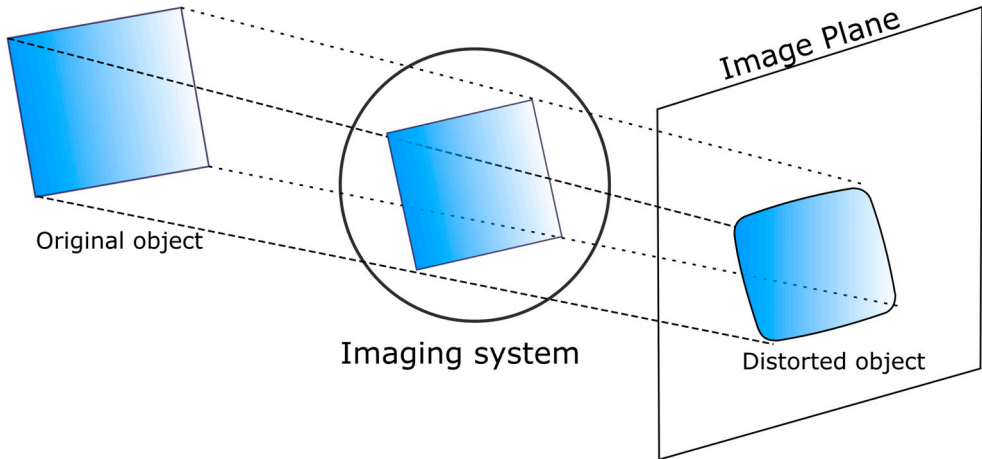**Figure 2.6:** Object distorted by distortion effects caused by the imaging system (such as a lens).

Camera lenses can sometimes introduce image effects such as radial or tangential distortions. The linear transform described cannot effectively take this into account. Therefore, distortions models are implemented to minimize such effects. A commonly employed model, developed by Brown [36] and often found in both

open-source and commercial calibration applications, has proven to be stable for volumetric imaging [8]. It is worth noting that if high quality optics are employed these types of distortions tend to be minimal, especially near the image centre. However, in specialized setups where distortions are intentionally introduced to achieve specific imaging characteristics, such as in Scheimpflug setups, it is important to recognize that modified camera transformations may be required to fully characterize the system.

As previously described, the pinhole camera model involves several unknown parameters within the camera matrices that require estimation. Practical estimation of these parameters is typically done through a camera calibration process. Various types of calibration methods exist, but the majority are based around imaging of a specific target, such as a checkerboard, point board, or a structured noise surface containing noise at different frequencies creating multiple detectable features in different length scales [37].
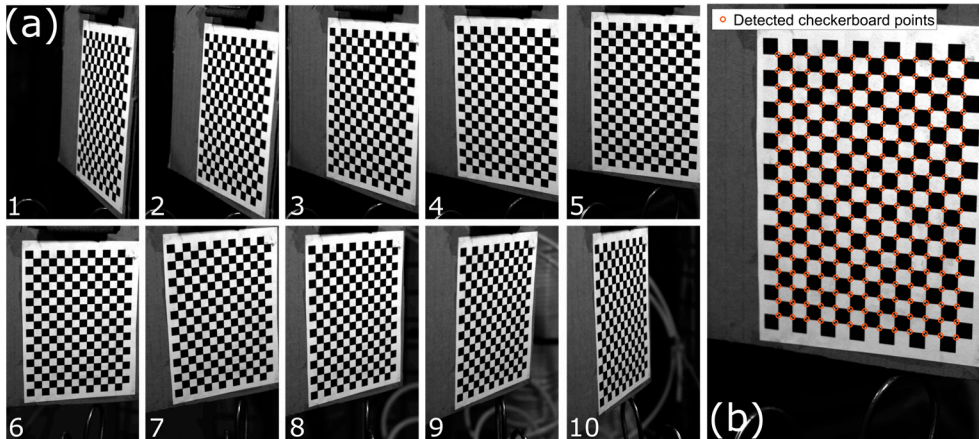
Figure 2.7: (a) Ten unique camera images of a checkerboard target with 14 x 19 squares. (b) Identified calibration points on the checkerboard target using a calibration routine.

For work described in this thesis, camera calibrations were conducted using a planar checkerboard target and Figure 2.7 (a) shows a sequence of images acquired of such a checkerboard target with a size of 14 x 19 squares. Different number of squares and square size were selected to accommodate each individual setup. The calibration process involves imaging of the target at various unique positions and orientations relative to the camera location. Subsequently, a feature detection algorithm, either based on edges or dots depending on the type of target, is employed to identify these features, as depicted in Figure 2.7 (b).

The calibration procedure was performed using Computer Vision System Toolbox in MATLAB 2022b. This toolbox, like others such as OpenCV [38] is advantageous

for calibrating multiple camera setups because it employs a method that assumes a planar calibration target. This allows the calibration of each individual camera followed by the establishment of a global coordinate system based on multiple images of the calibration target, visible to more than one camera simultaneously, used to map all cameras to the same coordinate system.

The calibration routine necessitates a minimum of three calibration images per camera, although superior results can be obtained by increasing the number to approximately 20 images. During this procedure, image distortions in terms of radial and tangential distortion were minimized. In cases where measurement volumes are confined, an increased number of images has proven advantageous as there is a high possibility that the full target will not be visible in the camera frame when being translated to different positions. Therefore, it is recommended to acquire more calibration images than strictly required, as post calibration might not always be possible. The versatility of this approach, that do not need a controlled target translation for camera calibration, has made it a widely adopted method in the field of volumetric imaging research [8]. Two sets of computed camera locations and orientations acquired from calibration are visualized in Figure 2.8, one from a more arbitrary camera arrangement (a) and another from an in-plane-half-circle arrangement (b).
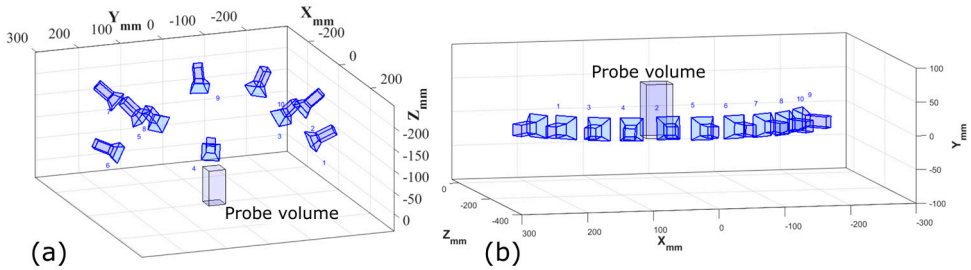
Figure 2.8: (a) Calibrated camera positions in an arbitrary arrangement. (b) Calibrated camera positions in a in-plane-half-circle arrangement.

The calibration of imaging systems containing multiple cameras is not always trivial. While planar calibration targets are commonly used as targets, alternative methods also exist where points in space generated by a laser pointer are imaged simultaneously by all cameras enabling the estimation of both extrinsic and intrinsic parameters as well as performing distortion corrections when calibrating systems consisting of at least three cameras [39]. Another approach is to increase the dimensions of the calibration target and instead image a 3D object. This approach offers several advantages, including the potential to reduce the number of required target translations during calibration when working with multiple cameras simultaneously. In cases where the 3D target is suitably complex, it may even permit single-shot calibration [40].

In some scenarios, one may encounter refractive media or objects, such as window surfaces, that enable optical access to the area of interest. Such refractive media can pose challenges in calibration, normal calibration routines can often handle such distortions but sometimes the use of different methods to mitigate any introduced errors are required. Hence, in the ideal application scenario, no such refractive element is present.

In experimental configurations that allow for controlled translation of calibration targets alternative calibration methods are available. An example of such a calibration scheme that can be very useful due to its simple numerical implementation is the method introduced by Machicoane [41] where a plane-by-plane transformation is used to establish a mapping between pixel coordinates and light rays. This approach establishes a connection between each pixel in the camera sensor and a 3D line traverses through the probed volume. Anything found along this line will be imaged at the location of the pixel. This is done by accurately translating a 2D calibration target, such as a checkerboard pattern, in steps along the target volume with each step representing a change in the Z dimension. This will map the whole probe volume using the X and Y coordinates from the target and the Z coordinate from the translation. Subsequently, a polynomial transform can be estimated to establish a mapping between image coordinates and world coordinates for each Z step. While this calibration procedure does demand precise target translation, it exhibits remarkable versatility in addressing imaging distortions, rendering it highly advantageous for calibrating camera systems dealing with refraction gradients [42].
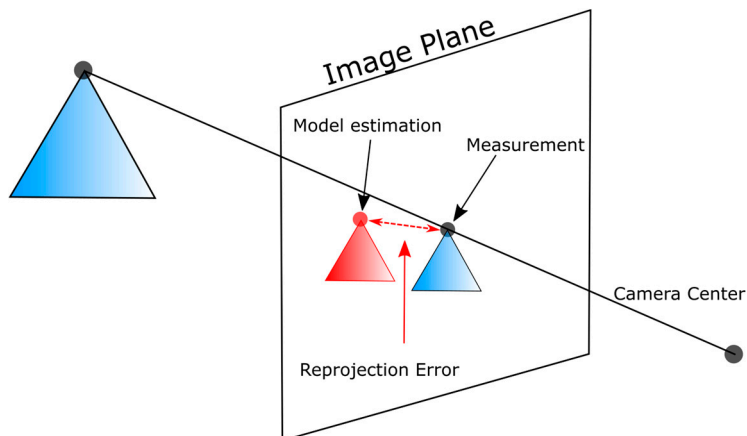

Figure 2.9: Illustration of reprojection error, the Euclidian image distances between a measured calibration point in the image plane and its corresponding point based on a estimated calibration model.

Appropriate camera calibration is essential for emission tomography measurements as it can heavily affect the techniques reconstruction accuracy. The quality of

calibration is generally assessed through the computation of the mean reprojection error RPE_{mean}, illustrated in Figure 2.9. This is the Euclidian image distances between measured calibration points in the image plane, obtained from the calibration target, and the positions where their corresponding 3D world points are projected onto the same image plane, based on the estimated calibration model acquired through the calibration process

$$RPE_{mean} = \frac{1}{N_{im}N_p} \sum_{i=1}^{N_{im}} \sum_{j=1}^{N_p} \|p_{ij} - \breve{p}_{ij}\|_2 . \tag{16}$$

Here N_{im} is the number of calibration images used in the calibration, N_p number of points on each calibration image, i is an image, j is a point, p_{ij} represent the detected point in the image plane and $\breve{p}_{ij}$ the corresponding 3D world estimated using the calibration model.

However, the effect of reprojection error RPE_{mean} on the reconstruction accuracy for emission tomography have not fully been assessed. More comprehensive investigations in this regard have been conducted within the field of tomographic PIV, where achieving subpixel accuracy concerning reprojection error is typically favoured [43, 44]. Therefore, one should aim for as low error as possible, especially in setups with a large number of cameras.

During the development of the emission-based tomographic approach outlined in this thesis, simulations were performed in regard to the calibration procedure to give further insight into the accuracy of the chosen calibration method. These simulations were carried out using the open-source 3D computer graphics software Blender [45]. Checkerboard calibration targets were imported into a vertical 3D space in Blender where they could be rotated and translated freely as depicted in Figure 2.10. Blender uses virtual cameras as viewports, as seen in Figure 2.10 (b), and true intrinsic and extrinsic parameters of the form presented in Equations (14, 15) can be extracted and compared to camera parameters calibrated from the virtual images of the imported checkerboard.
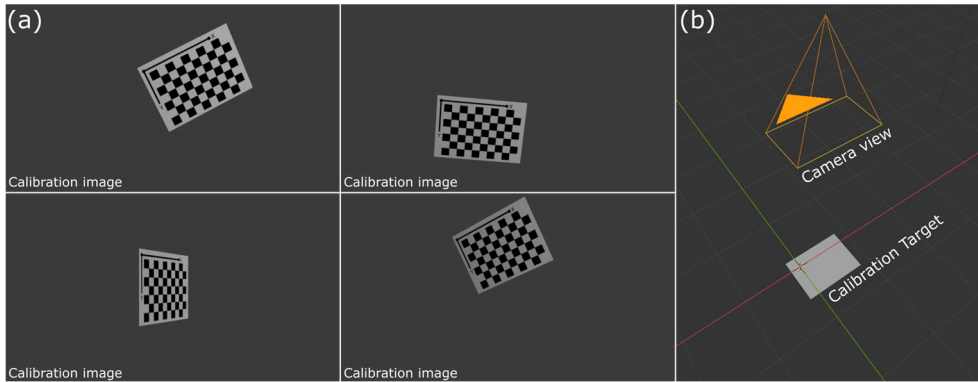
Figure 2.10: (a) Set of virtual images of a checkerboard target acquired using the virtual camera view. (b) Illustration of virtual camera view and imported calibration target within a virtual environment in Blender.

This approach provided a straightforward way of testing robustness and accuracy of the calibration routine. However, it is important to note that these calibration conditions are very ideal both in terms of light, distortions and other factors that will be present in a real configuration. Nevertheless, these types of simulations allow for test reconstructions using simulated calibrated parameters as well as preliminary camera arrangement test. This is most beneficial when testing a tomographic reconstruction approach as the setup calibration is highly important, even if the conditions are most ideal.

An additional calibration routine, which can be particularly important for certain emission tomography configurations, is the white-field or flat-field calibration. This process aims to mitigate varying pixel sensitivity and collection efficiency of the imaging optics such as vignetting, both within individual cameras and across cameras within the setup. White-field calibration can be accomplished by capturing images of a uniformly illuminated target, such as a uniformly illuminated screen or a digital computer display. The white field calibrations performed in this thesis used a white plastic screen positioned in front of the camera optics and back illuminated using a computer LED monitor set to emit white light.

The act of acquiring a good calibration in practice can prove complex, especially when calibrating a camera system comprising multiple cameras as in emission tomography experiments. It is beneficial to set up a repeatable calibration routine which can be performed both pre and post measurements to investigate any change or drift in the setup. Another piece of advice is that when calibrating a volumetric setup using a planar target such as a checkerboard, it is highly beneficial to have the whole volume in camera focus and acquire images throughout the whole measuring space. However, this can be especially hard to perform in setups with customized optical components such as view splitters in combination with objectives that have large fixed aperture and thus in turn a small depth of field.

18

2.4 Volume sampling

To complete the imaging model and construct the finalized projection matrix A which is used in the subsequent reconstruction, as outlined in Equation (8), it is necessary to sample the volume of interest that is being probed. This sampling is performed to acquire the projection approximation of each intensity measurement b_{qp} as seen in Equation (5). Consequently, one needs to acquire the luminosity contribution w_{qpv} of each specific voxel x_v to each camera pixel p across all the camera views q in the setup. There exist multiple different methods to perform this sampling, and they can typically be categorized into two groups namely ray-centric or voxel-centric models.

Ray-centric sampling models works by tracing light rays originating from the camera image and passing through the probed voxel volume. Various types of ray-centric methods exist, including line rays, cylindrical rays, and conical rays, each possessing distinct characteristics. Line rays assumes the recorded intensity integral trough the volume to be a line with the contribution w_{qpv} to each measurement pixel b_{qp} from a voxel x_v calculated based on the intersection between this line and the volume voxels. While this approach sacrifices some accuracy, it enhances computational speed. Cylindrical and conical rays represent improvements over line rays where instead the contribution w_{qpv} is determined based on the volumetric intersection between the rays and voxels [46]. Nevertheless, many ray-centred models are computationally expensive, and simplifications are often needed to decrease the computational costs [8].

The tomographic approach within this thesis adopts a voxel centric model where instead of tracing image rays going through the probed voxel volume, each voxel projection is traced back to the image plane. Hence, each column value in the projection matrix A will represents the contribution of a voxel (specific to that column) to every camera pixel in the optical setup (corresponding to the matrix rows). This gives that each column in A describes a voxel projection into each camera in the imaging system. Such a voxel projection is called a voxel spread function [47, 48], due to the basis used being a discretized voxel space. This concept bears similarity to that of a point spread function in imaging systems or an optical transfer function found in tomographic PIV [49, 50]. It should be noted that while this projection model commonly employs a voxel basis, it is not inherently restricted to it.

To obtain the voxel spread function, every individual voxel v in the discretized volume is sampled multiple times by projecting uniformly placed points from within each voxel onto the camera sensors. This is similar to methods such as the one employed by Liu H [51]who used Monte Carlo raytracing simulations for voxel sampling and or to the work of T. Yu [52] who considered each voxel being made

up of a large set of points. The projection of each sample point is carried out using the calibrated camera matrix of each camera, as defined in Equation (15). Point locations $\vec{s}$ within the volume are mapped to camera sensor points $\vec{x}$ using the camera matrix $\vec{x} = P(\vec{s})$. This will yield a distorted projection, the voxel spread function, of individual voxels in each camera as illustrated in Figure 2.11.
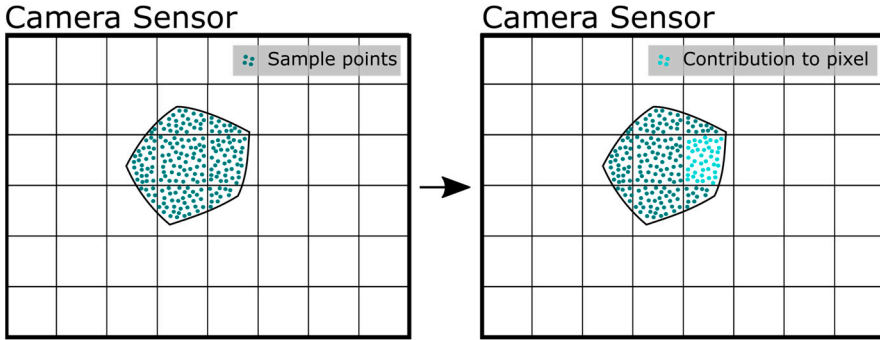

Figure 2.11: Illustration of voxel sampling. The voxel projection is made up of point projections from sampling, contributions to each pixel corresponds to fraction of points projecting to respective pixel.

Voxels in tomographic setups typically have a larger size compared to camera pixels, although this depends on the chosen voxel size, camera distance and camera resolution. Therefore, each voxel can generally project to more than one pixel and thus sections of each such voxel projection will fully or partially overlap with multiple different image pixels. When sampling the voxel with multiple projection points the intensity contribution weights, denoted as w_{qpv} in Equation (5), from each voxel v are determined by the number of sample points that project onto a specific pixel relative to the total number of sample points used. These contributions to each sensor measurement b_{qp} can then be reshaped into the projection matrix A which will be sparse. This type of approach tends to be computationally expensive but has the potential to generate an very accurate forward model for emission tomography [8].

Different types of sampling methods were tested before settling on the selected method described above. The initial method tested was a simple point projection model, where the centre of each voxel was projected into each camera and the pixel coordinate that projection landed on was given the full contribution of the voxel intensity, depicted in Figure 2.12 (a). This simplifies and reduces the computational cost of the projection matrix A substantially but also introduces errors, sometimes large ones, based on the voxel to pixel size ratio. While this simple point projection model proves advantageous when performing test reconstructions during the making of new tomographic measurement setups, its use is discouraged for actual reconstructions, especially when the voxel size substantially exceeds that of the camera pixels.
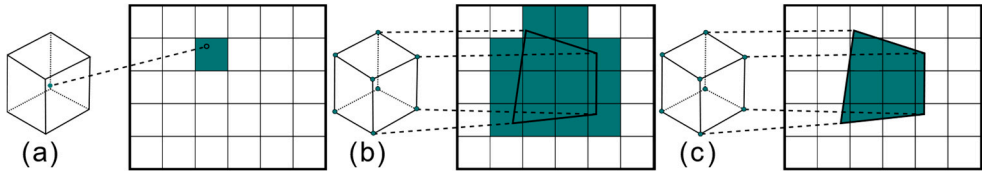
Figure 2.12: Illustrations of models for sensor pixel illumination by a single voxel. (a) simple centre point projection, (b) box-projection method, (c) convex hull method.

The second method tested was termed "box projection" and were based on the projection of all eight voxel corners onto the camera sensor as illustrated in Figure 2.12 (b). Thereafter, the voxel intensity was split evenly between every pixel intersecting this projected area. This approach offers the advantage of still having relatively low computational overhead while enhancing the accuracy of voxel-to-pixel mapping in comparison to the initially tested simple point method. The third method illustrated in Figure 2.12 (c) was based on a convex hull approach. Instead of assigning the same intensity contribution to each pixel intersecting the projected area, the amount of intensity contribution was based on the extent of overlap. This final method improved the voxel mapping, but the implementation turned out to be quite computationally expensive.

It is important to recognize that because a voxel is a three-dimensional entity, the overlap between the projection area and pixels, such as in the convex hull method, do not fully represent the voxels intensity contribution to each pixel. The chosen method, the voxel spread function, takes care of this aspect due to sample points being volumetrically distributed within each voxel. Additionally, it is important that all sample points are located within each camera's depth of field region, as each point are given a constant weight. If this criterion is not fulfilled differences caused by varying circle of confusions will induce errors within such a projection model.

In certain experimental setups, it is possible to take advantage of paraxial approximation which has been used in previous tomography applications [53, 54]. Paraxial approximation assuming that the angle between the optical axis and each projection ray is small, granting close to orthographic projections of each voxel due to the light rays being orthogonal to the projection image plane. This can yield an approximation where all voxels are considered to have a very similar voxel spread function. This significantly accelerates computation time and is deemed valid when the distance between the lens and the probed volume is reasonably large and the object of interest is in the centre of the field of view.

Undesirable aliasing effects can occasionally occur due to the systematic discretization of the volume, leading to unwanted frequency patterns in the projection mapping. This can be observed in Figure 2.13 (a), where a projection of a hollow Gaussian cone phantom displays such effects. These patterns often result in prominent streak artifacts within the reconstructed volume. Streak artefacts are a

common phenomenon in tomography, and they are made worse by these aliasing frequency patterns. To mitigate these patterns, a process was implemented that involved slight random displacements of each voxel's sampling coordinates before projection, reducing the impact of these discretization-related effects, as shown in Figure 2.13 (b). Slightly shifting voxels in this manner could have a minor effect on spatial projection resolution and can be seen as a minor trade-off between estimation accuracy and reconstruction resolution.
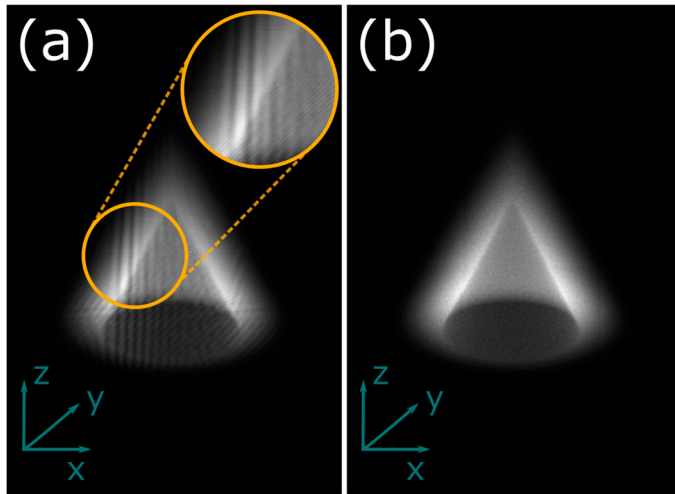

Figure 2.13: (a) Gaussian cone phantom visualized using projection method without randomized voxel sampling, aliasing effects are visible. (b) Gaussian cone phantom visualized with randomized voxel sampling.

To further constrain the system and decrease computational costs it is possible to introduce a hull-constraint. When applied in emission tomography within the work of this thesis such hull-constrains were implemented based on space-carving [55, 56]. They were applied to the probed volume before the reconstruction, following a similar approach to the work by Yucheng Fu [57]. The space-carving method involved projecting each voxel onto all cameras in the system and if any voxel projects to a total pixel area with zero intensity in any individual camera that voxel is removed from the volume. This removes voxels that are known to have zero intensity prior to the reconstruction which reduces the size of the projection matrix *A* and thus the overall computational time while retaining the studied objects overall shape. Voxels with zero intensity close to the investigated object, at the edge of the hull constraint, were kept providing flexibility in the system's solution process.
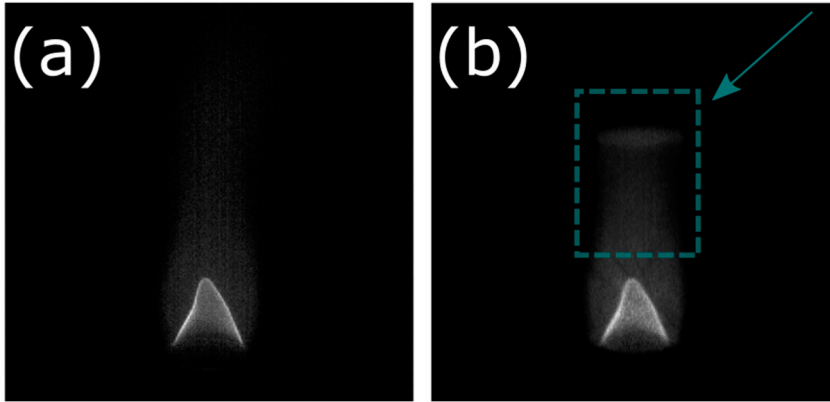
Figure 2.14: (a) Camera image of a CH4/air flame used in reconstruction. (b) Projection of the reconstructed flame made at the same view position as the displayed camera image, effects of an applied hull constraint are outlined.

Figure 2.14 shows a comparison between original camera images and reconstruction projections at the same view position of a CH$_4$/air flame measurement. Projection (b) is taken at the same view position as the original camera image (a). The effects of a hull constraint applied during reconstruction are visible in projection (b). In this projection, intensity originating from above the hull can be observed accumulating at the top of the reconstructed volume, as indicated by the arrow. While this outcome is expected and not ideal, it generally has minimal impact on the rest of the reconstruction due to the very low intensities outside the hull. However, every setup needs to be evaluated individually and there may be cases where a hull constraint is challenging to implement or unnecessary. Such a situation could arise in measurements characterized by a very low signal-to-noise ratio (SNR) in the acquired camera images, making it difficult to accurately distinguish the edges of the studied object.

2.5   Solvers

The final main piece in the tomographic reconstruction method is the inverse solver used to solve the resulting equation system. Volumetric imaging using emission tomography within the field of reactive flows deviates some from the typical use of tomography, which was originally developed for medical diagnostics [5]. To begin with, the objects investigated in this these contexts are often highly dynamic and unsteady, requiring instantaneous measurements or time resolved measurements using high speed sensors. This generally leads to a limitation in the number of projections of the target volume that is available because the measurement sensor cannot be moved around to acquire more projections. Instead, multiple sensors are

used to simultaneously capture the projections. This results in both economic limitations, due to sensors such as cameras or even high-speed cameras can be quite expensive. Additionally, achieving optical access can be challenging in contrast to many medical tomography setups where obtaining numerous projections can be comparatively straightforward.

One of the most used inverse solvers, in the field of 3D tomographic combustion diagnostics, is the algebraic reconstruction technique (ART). ART is an iterative and additive solver designed for linear equation system and was first introduced to the field of image reconstruction from projections in 1970 [58]. ART offers a notable advantage in that it allows easy implementation of priori information in between iterations [17, 59]. Various variations of ART have similarly been used involving truncation or Tikhonov regularization for smoothing [12, 60]. Other solvers have also found application due to their different individual strengths. Some examples include simultaneous ART where the iterative additions are done at the same time increasing parallelizability and thus reducing computational costs [61]. Multiplicative ART or its simultaneous counterpart SMART that maintains zero-intensity values as zero due to their multiplicative nature, which proves beneficial in some investigated topologies [14, 62, 63]. Moreover, stochastic methods have at times been employed for solving the 3D tomographic problem [64] and there have also been a growing trend in employing deep learning techniques to solve tomographic problems [65]. With the use of large training data sets these methods can be highly computationally efficient algorithms, although obtaining high-quality training data can pose a challenge.

The reconstruction of 3D fields in emission tomography typically demands substantial computational resources, with reconstruction times spanning from minutes to days. Naturally, these timescales depend upon several factors, including the dimensions of the reconstruction, the choice of solver, the solver implementation, and the quality of computational hardware. Therefore, computational cost plays major role in the selection process when choosing solver, even more so when performing time resolved measurements. The tomographic work presented in this thesis applied the preconditioned gradient method (PCG) to solve the resulting inverse problem mainly due to high computational performance and implementation ease. This allows for quick reconstructions for use in time resolved measurements or statistical studies requiring many field reconstructions. The method was implemented in MATLAB version 2022a.

Solution values in the reconstructed field that are negative are for emission tomography measurements generally regarded as non-physical. Therefore, a simple non-negativity constraint was implemented in the reconstruction routine. This constraint was achieved by iteration of the PCG algorithm with voxels containing negative intensity values in previous results being iteratively removed. Convergence is not guaranteed using this method but non convergence was never observed and simulations together with visual inspection of experimental reconstructions showed

good results and consistency. Similar constraints are often used together with reconstructions using ART, where the intensity value of negative voxels is set to zero in between reconstructions.

The stopping criteria for determining convergence was a tolerance on the relative residuals

$$\|b - A\boldsymbol{x}\|/\|b\| < 10^{-6}. \tag{17}$$

Here the relative tolerance was set to 10^{-6} , similar to other work within the field [17]. Maximum number of allowed iterations was kept to 10^3 but generally, the algorithm was terminated based on tolerance after around 20-120 iterations. However, this varies from system to system and larger systems may need additional iterations.

The computational cost of a 3D tomographic emission field reconstruction using this method can be separated into two distinct stages. First, the computation of projection matrix A where in the case of ten cameras, the number primarily used in the works shown in this thesis, the computational time was around 30 s up to more than an hour. This time depends on factors such as the chosen voxel sampling method, the number of voxels N_v, and camera measurements b. The computation time may increase further but only needs to be performed once for each camera setup. Secondly, the reconstruction itself involves solving Equation (9) using a PCG solver. A crucial step here is computing the forward matrix vector products of the form $(\lambda Q + A^T A)\boldsymbol{x}$ with $\boldsymbol{x}$ being the current best estimate of the solution. It is essential to avoid forming the entire matrix, since $A^T A$ will be almost completely dense thus requiring large amounts of memory. Instead, only the necessary matrix vector products $(\lambda Q + A^T A)\boldsymbol{x} = \lambda(Q\boldsymbol{x}) + A^T(A\boldsymbol{x})$ are computed. This approach significantly reduces both computational time and memory demands. The computational time for the PCG ranged from 10-30 s up to an hour for different sized reconstructions.

In terms of computer memory requirements, the sparse smoothing matrix Q is a large N_v-by-N_v matrix, but it is sparse because the number of non-zero elements is small. Having the smoothing operator only include the six direct voxel-neighbors every row of the Q matrix will only contain seven non-zero elements (representing the voxel itself and the six neighbors). Storing such a sparse matrix demands very little memory, approximately 250 Mb in many of the current applications, although this depends on the value of N_v. The final sparse projection matrix A will be b-by-N_v mapping the N_v voxels to the pixels in all image planes. Since each measurement can be seen as a camera ray going through the domain volume each row of A can be estimated to have roughly $\sqrt[3]{N_v}$ non-zero elements. In practical terms, for a case involving 10 cameras, the matrix A would initially have about 10^8 non-zero elements and requires around 1 Gb of storage. This storage requirement can be

reduced by applying a hull constraint, but the reduction will depend on the the size and nature of the object investigated. In cases involving a hull constraint within this thesis, reductions of 10-25% were commonly achievable.

In the field of emission tomography applied in reactive flows, there is currently a lack of comprehensive studies concerning reconstruction resolution [8]. This scarcity of research primarily comes from the complex nature of the issue. Reconstruction resolution is dependent on numerous factors, including the reconstruction solver, volume discretization, prior information like smoothing, camera quantity and placement, to just name a few. Some tries of estimation have been performed with Floyed [46] introducing an approximation for the reconstruction resolution length scale while employing ART as the iterative solver

$$L_{res} = \frac{2\sqrt{2}V_D}{N_{views}} \tag{18}$$

where L_{res} is the resolved length scale V_D the volume size and N_{views} number of projection views. Here one can observe the expected benefit of an increase in the amount of projection views in comparison to a lower count of views. Due to the complexity of defining a general resolution metric it is important to evaluate every individual application separately and empirical tests will generally prove a suitable path as it will relate more towards resolution of structures in the reconstructions [53, 62].

3 Applied 3D diagnostics

The capability to acquire 3D information for extracting characteristics and conducting measurements in all three dimensions is crucial, as many processes inherently are three-dimensional. This chapter discusses the implementation of the developed tomographic technique in both combustion diagnostics, focusing on flames, and in plasma diagnostics, investigating gliding arc plasmas, published in papers I and II. Additionally, the chapter covers 3D particle tracking in metal combustion using a stereoscopic high-speed camera configuration, published in paper III.

3.1 Arbitrary position 3D tomography in combustion diagnostics

This work looked at emission tomography of chemiluminescence from premixed CH_4/air flames and ethanol pool flames using the tomographic method developed within the work of this thesis, described in chapter 2. The aim was to evaluate the tomographic routine and experimentally examine the influence of camera positions. Previous research has numerically explored varied camera placements on 3D tomographic reconstructions to optimize positioning [66], and experimentally investigated using a single movable camera [47]. Here multiple arbitrarily placed CMOS cameras were used to perform experimental evaluation of tomographic flame field reconstruction.

The majority of previous 3D tomographic investigations of flame fields are conducted within tightly regulated laboratory settings, where constraints due to limited optical access are minimal. However, similar to application of other optical methodologies in real-world scenarios [67-69], the process of transitioning measurement setups from controlled laboratory environments to practical devices for in-situ diagnostics can present considerable challenges. Complicating factors can encompass limited optical access that will impede camera positioning, diminished field of view for individual cameras, sensitivity reduction resulting from window fouling, and the potential for image overexposure due to inadequate dynamic range of sensors. All these factors collectively contribute to the difficulty.

When achieving optical access in practical setups, the conventional in-plane-half-circle camera configurations and mirror arrangements using dual or quad scopes [14, 70], are seldom feasible due to apparatus constraints. Thus, arbitrary camera placements become necessary to adapt to available optical access. However, the positioning of acquired projections directly can impact measurement quality [71], posing challenges for equipment size, calibration procedures, and reconstruction methods. A practical scenario where in-situ 3D tomographic flame field studies could be done, but requiring flexible camera positioning, is exemplified by the marine engine cylinder head with 24 optical access ports displayed in Figure 3.1.
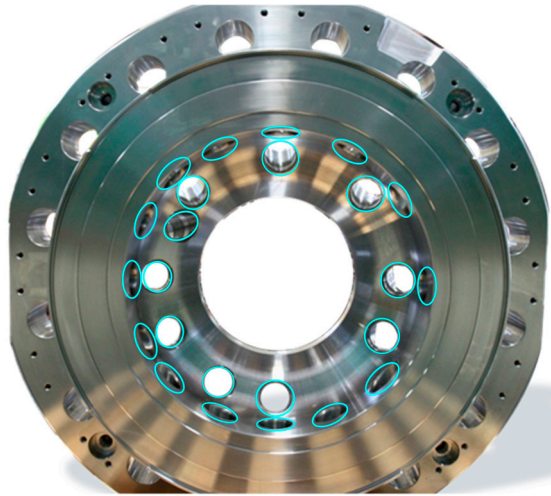

Figure 3.1: Image of an optical accessible cylinder head with 24 access ports (marked by cyan circles) for large bore marine engines. Courtesy of Johan Hult, MAN Energy Solutions.

Reconstructing 3D flame chemiluminescence fields, emitted from various excited species during combustion (e.g., C2*, CH*, and OH*), can offer valuable insights into flame characteristics such as propagation, geometry, wrinkling, curvature, surface density, and identification of recirculation regions. Notably, CH* and OH* are important for reaction and post-flame zone analysis [13, 14]. In this work, the primary emission source was chemiluminescence from CH*, particularly the $A^2\Delta - X^2\Pi$ transition, which emits within the visible spectrum.

Flame field reconstructions of the chemiluminescence field from unsteady CH$_4$/air Bunsen flames were performed using an arbitrary camera arrangement. Figure 3.2 presents reconstructed reaction zones at normalized intensity for two different such CH$_4$/air flames. The reconstructed volume was discretized into voxels, with dimensions of 100 x 121 x 81 in the x, y, and z directions, respectively. The section of the flame field facing the reader has been removed to illustrate the capability to capture the anticipated empty interiors in the reconstructed flames.

Minor line artifacts can be observed in the reconstructions, particularly in areas with higher intensity, like the top of the flames. However, these artifacts do not significantly affect the overall estimation of the flame topology. These results indicate that flexible camera arrangements, which often are more suitable for in-situ measurements, can adequately capture the expected field topology of unsteady Bunsen flames to a satisfactory level.
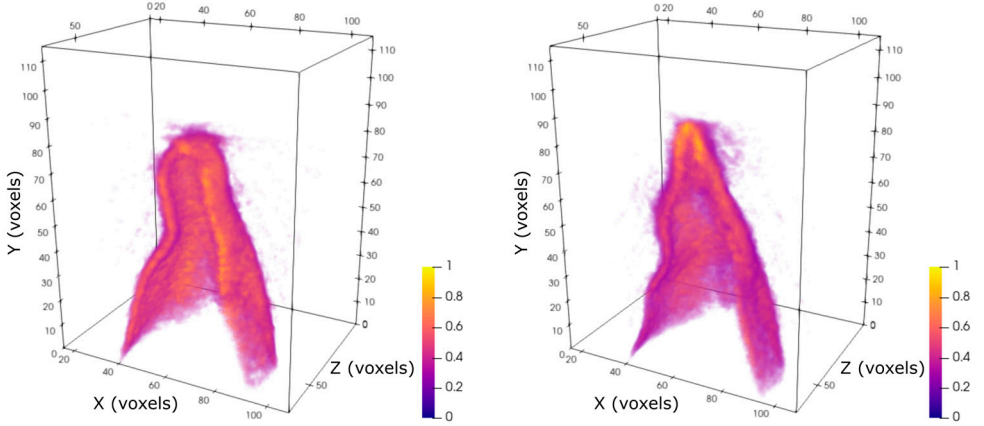

Figure 3.2: Reconstructed chemiluminescence fields of the reaction zone from two different experimental premixed CH4/air Bunsen flames. Section of the flame field facing the reader has been removed to show the hollow interior of the Bunsen flames. The luminosity is normalized between 0 and 1.

To investigate the effect of camera view numbers on field reconstruction quality for arbitrary camera arrangements, synthetic phantom field reconstructions at resolutions of 129^3 voxels were made from 50 different camera sets with randomized camera positions. Each camera position in every set where randomized between an azimuth angle of 0°- 360° and elevation angle of -45° - 45°. Note that these tests are made in perfect conditions with minimal errors and will most likely not represent real practical reconstruction quality.

Estimation of the phantom reconstruction quality was done using two different criteria. The first was structural similarity index (SSIM), a frequently used in the field of image analysis that look at dependencies between spatially close pixels or voxels [72]

$$SSIM = \frac{(2\mu_{True} \times \mu_{Rec} + C_1)(2\sigma_{True \cdot Rec} + C_2)}{(\mu_{True}^2 \times \mu_{Rec}^2 + C_1)(\sigma_{True}^2 \cdot \sigma_{Rec}^2 + C_2)} \tag{19}$$

where μ_{True} is the simulation phantom mean value, μ_{Rec} the reconstruction mean value, σ_{True}^2 and σ_{Rec}^2 the respective variances of simulation phantom and

reconstruction, $\sigma_{True \cdot Rec}$ the covariance between simulation phantom and reconstruction, C_1 and C_2 are stabilization parameters based on the dynamic range of voxel values. The second was root-mean-square-error (RMSE)

$$RMSE = \sqrt{\frac{\sum_{i=1}^{N_v}\left(x_i^{True} - x_i^{Rec}\right)^2}{N_v}} \tag{20}$$

where N_v is the total number of voxels in the reconstruction, x^{True} the simulated phantom and x^{Rec} the resulting reconstruction. Results are presented in Figure 3.3 with standard deviation based on all 50 different camera sets. Additionally, reconstruction results from a single in-plane-half-circle arrangement are included for comparative purposes.
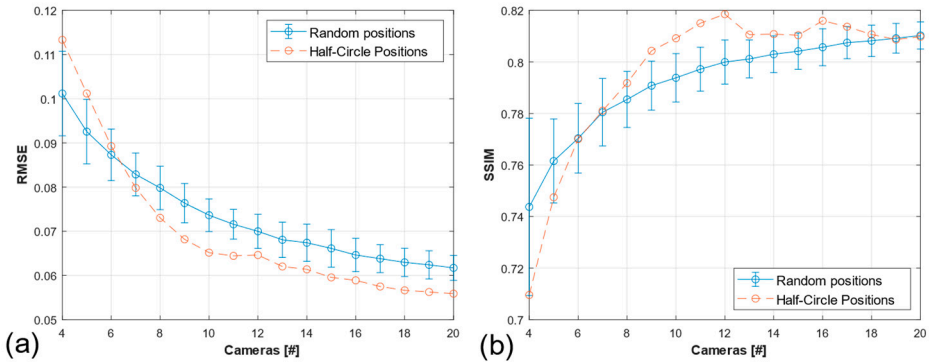

Figure 3.3: RMSE (a) and SSIM (b) respectively of synthetic phantom reconstructed using simulated randomized camera positions compared to an in-plane-half-circle camera arrangement. Error bars represent standard deviation.

The in-plane-half-circle arrangement generally show superior performance, likely because it leads to lower spatial variation between projections, in line with earlier research on in-plane camera placements [53]. This validates the preference to use such an arrangement in well-defined laboratory settings. However, the difference is relatively modest, approximately around 1%. At lower camera view counts ($N_q \leq 6$) arbitrary positions seem to perform equally well or slightly better, up to about 2% suggesting that having input data from diverse viewpoints outweigh the negative effects of increased spatial variation. In real experiments these differences are expected to be grater.

To experimentally test versatility and reconstruction convergence of an arbitrary camera setup, stable ethanol pool flames were reconstructed using subsets of 10 arbitrarily placed cameras. Here the probe volume was discretized into 60 by 60 by 200 voxels. Convergence assessment is crucial to ensure that reconstructions using

arbitrary camera arrangements provide accurate estimations of flame fields. In the following instances, the compared projection viewpoints did not align with any data view employed in the reconstruction process.

Figure 3.4 displays a comparison of intensity distributions in two projections generated from separate field reconstructions of the same ethanol flame. These two field reconstructions are generated using different subsets of six cameras each, with two views being common to both sets. This is similar to the approach employed by Meyer et al. [62]. Additionally, a reference intensity line obtained from a field reconstruction using all ten available cameras is included for comparison.
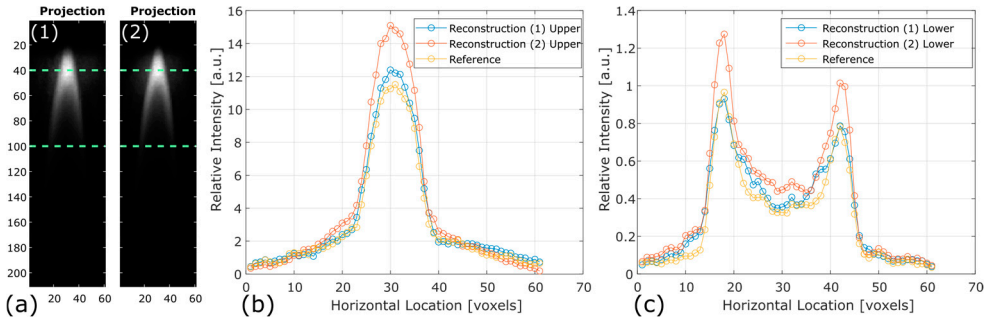

Figure 3.4: Comparison of intensity distributions in projections from two separate field reconstructions (a, 1) and (a, 2) of the same ethanol flame. Intensity is evaluated along an upper and a lower line (light green). (b) Intensity along the upper line for both projections. (c) Intensity along the lower line for both projections. Subsets of six cameras were used, with two cameras shared between sets. The intensity line labelled as 'Reference' in (b) and (c) corresponds to a field reconstruction using all 10 available cameras for comparison.

The projections in Figure 3.4 (a,1) and (a,2) show similar flame intensity structure and feature size across both lines. Nonetheless, while the relative intensity remains consistent between both projections, it is notable that the overall absolute intensity appears lower in reconstruction (1), which is evident in both (b) and (c).

Similar intensity difference is noted when comparing the vertical centre slices of the two reconstructions, displayed in Figure 3.5 (a,1) and (a,2), obtained from the same viewpoint as the previous projections in Figure 3.4. Furthermore, subtle structural differences are discernible, such as the slight intensity spike at approximately 51 voxels in Figure 3.5 (c), which is visible in reconstruction (1) but not apparent in (2). While the flame intensity structure aligns with the reference reconstruction in both (1) and (2), variations in absolute intensity are evident in both cases.
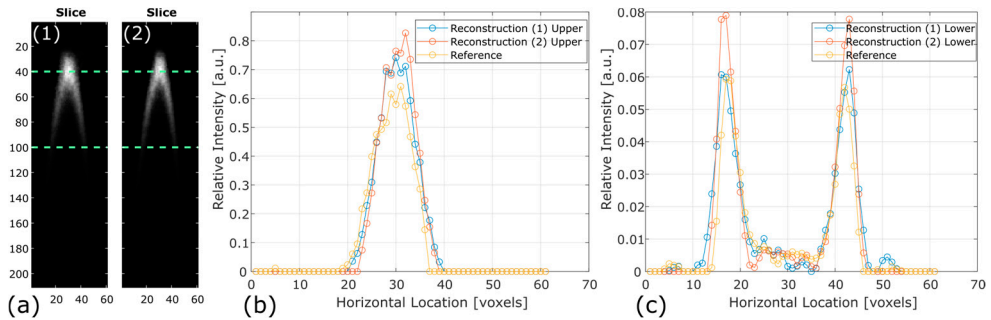
Figure 3.5: Comparison of intensity distributions in vertical center cross section slices from two separate field reconstructions (a, 1) and (a, 2) of the same ethanol flame. Intensity is evaluated along an upper and a lower line (light green). (b) Intensity along the upper line for both slices. (c) Intensity along the lower line for both slices. Subsets of six cameras were used, with two cameras shared between sets. The intensity line labelled as 'Reference' in (b) and (c) corresponds to a field reconstruction using all 10 available cameras for comparison.

To understand the limitations associated with arbitrary camera positions, the same flame field depicted in Figure 3.4 and Figure 3.5 was reconstructed once more. However, this time, subsets of four cameras were employed for the reconstruction, with no overlap in cameras between the sets. Increased reconstructions differences can be seen between vertical slices displayed in Figure 3.6. More pronounced effects on larger flame structures are observable, as indicated by variations in flame position between the slices (a) and the intensity distributions along the upper dashed lines (b). While a semblance of the flame structure persists between the lower dashed lines (c), variations in intensity are still observable, particularly in the right peak, along with some artificial broadening. These results indicate, similar to previous results, that flexible camera arrangements can capture suitable flame fields. Nevertheless, when the camera count is reduced the expected decline in reconstruction occurs and one needs to be observant.
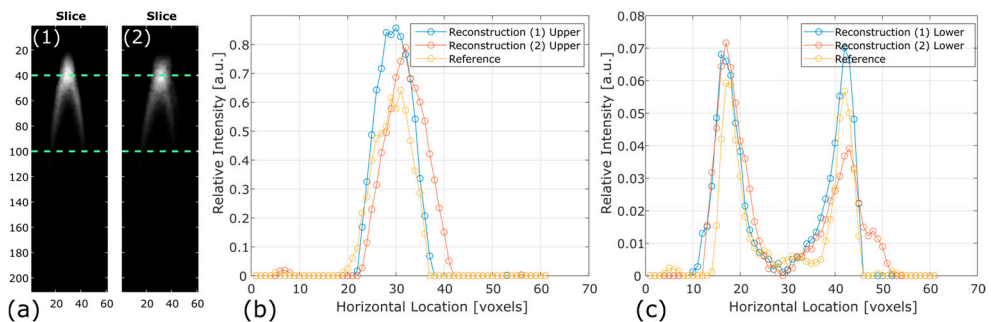

Figure 3.6: Comparison of intensity distributions in vertical center cross section slices from two separate field reconstructions (a, 1) and (a, 2) of the same ethanol flame. Intensity is evaluated along an upper and a lower line (light green). (b) Intensity along the upper line for both slices. (c) Intensity along the lower line for both slices. Subsets of 4 cameras were used, with no cameras shared between sets. The intensity line labelled as 'Reference' in (b) and (c) corresponds to a field reconstruction using all 10 available cameras for comparison.

This work focused on advancing the accessibility of 3D tomographic techniques for practical applications, particularly in situations where optical access is limited. Note however, that optimal reconstruction and experimental parameters will be between specific applications and must be assessed on an individual basis. Consequently, the methodology this work introduces for 3D tomographic investigations employing arbitrarily positioned cameras, aim to offer help when performing in-situ measurements in real-world setups, addressing aspects like priori information utilization, camera placement, and the evaluation of 3D flame field reconstruction.

3.2   3D emission tomography of gliding arc plasma

Once the functionality of the developed tomographic approach was established, it was employed in studying practical applications, here the investigated object was atmospheric gliding arc discharges.

Atmospheric pressure plasma has seen growing attention due to its diverse applications across multiple disciplines and industrial sectors including materials and surface treatment [73, 74], combustion science [75-78], and chemical control [79]. This heightened interest underscores the necessity for a more comprehensive understanding of these types of plasmas. Among the methods employed to produce plasma, gliding arc discharge [80] stands out as one such technique. Gliding arcs can generate atmospheric non-equilibrium plasma in sizable volumes [81] and offers access to pathways not typically available in equilibrium conditions. However, it presents challenges in terms of diagnostics and 3D geometrical dynamics due to the complex interactions between the plasma and the surrounding gas.

Here, non-intrusive 2D optical diagnostics has been a common approach to investigating gliding arc discharges [29, 81, 82]. However, the inherent 3D nature of plasma arc discharges benefits from measurement techniques capable of acquiring information in all three dimensions. Earlier 3D research on gliding arc plasma discharges includes investigations of hydroxyl radical distributions through the FRAME technique [28, 83] as well as 3D slip velocities together with plasma column lengths employing particle tracking velocimetry (PTV) [84].

More alternative non-invasive 3D diagnostic methods are therefore of great interest, and this work apply 3D emission tomography to investigate gliding arc discharges, capturing volumetric luminosity data across the entire probed volume. The reconstructed luminescence is in the visible wavelength range, particularly originating from N_2 chemiluminescence.

Focus was on quantifying and characterizing attributes that are typically challenging to acquire without access to volumetric data, including position, geometry, and

topology. The determination of arc length is one such attribute, crucial when calculating electric field strength [80, 85], and earlier measurements have primarily relied on 2D imaging techniques [29, 82, 86, 87].
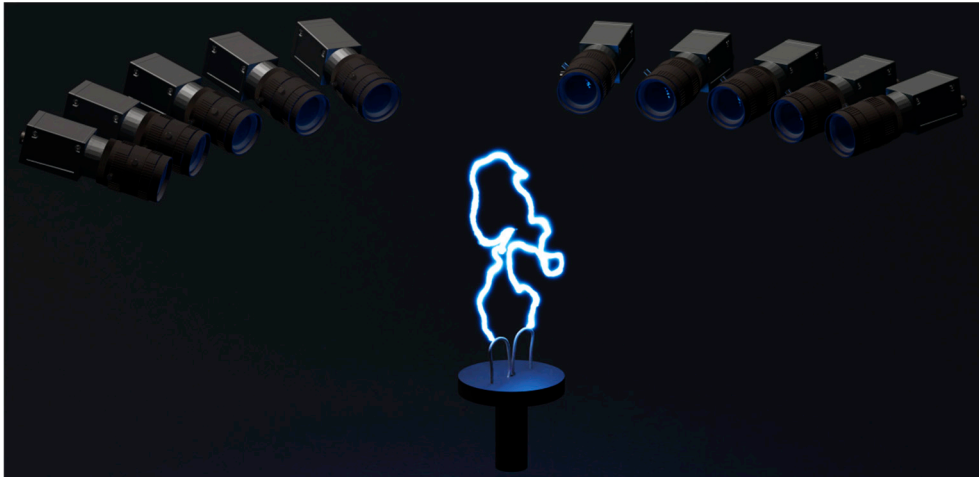

Figure 3.7: Schematic illustration of emission tomography setup and electrodes. The depicted gliding arc is a rendition of a reconstructed real discharge using emission tomography.

The gliding arc discharge system consisted of two water-cooled stainless-steel electrodes powered by an AC supply operating at a frequency of 35 kHz, similar discharge systems have been employed in previous studies [28, 81, 84, 88, 89]. A schematic of the experimental arrangement can be found in Figure 3.7. A vertical airflow at 10, 20, 30 and 40 L/min, responsible for vertically moving the plasma arc, was introduced between the two electrodes via a small orifice with a diameter of 3 mm.

The luminescence field measurements were conducted using 10 commercially available CMOS cameras. These cameras were positioned in an in-plane-half-circle around the electrodes, as illustrated in Figure 3.7. To enhance the signal while maintaining a sufficient depth of field, the f-number was set to f/4. Resolution was software binned to 900 by 600 pixels resulting in a signal to noise ratio (SNR) ranging from 200 to 500, depending on the airflow rate. The reconstructed volume was discretised into 221x221x221 voxels, with a spatial voxel resolution of 0.5 mm/voxel. This resolution was carefully chosen to strike a balance between capturing fine details while maintaining computational efficiency. In total, 500 measurements were carried out for each individual flow case.

Two tomographic 3D reconstructions at air flows of 10 L/min and 30 L/min respectively can be seen in Figure 3.8. The arc topology and arc thickness can be seen to change in between cases due to different turbulence levels.
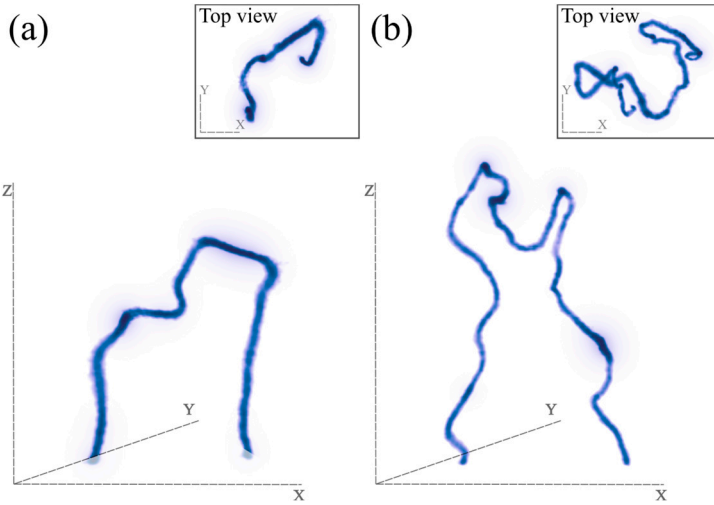
Figure 3.8: 3D tomographic luminosity reconstructions of typical plasma arcs at flow rates of (a) 10 L/min and (b) 30L/min.

The 3D arc length is acquired by estimating arc coordinates from the tomographic reconstructions. This is done by identifying the start and end points of the arc within the bottom slice of the reconstructed probe volume. Subsequently, the arc was found using Dijkstra's algorithm for the shortest path. The distance between two voxels was weighed by the inverse cube of their average value to find the shortest path given highest luminosity (centre of arc). Following this, a smoothing operation is applied to the discrete arc path, this process generates a set of ordered coordinates that define the arc path as seen in Figure 3.9. The arc length is then computed as the sum of all the Euclidean distances between these adjacent coordinates.
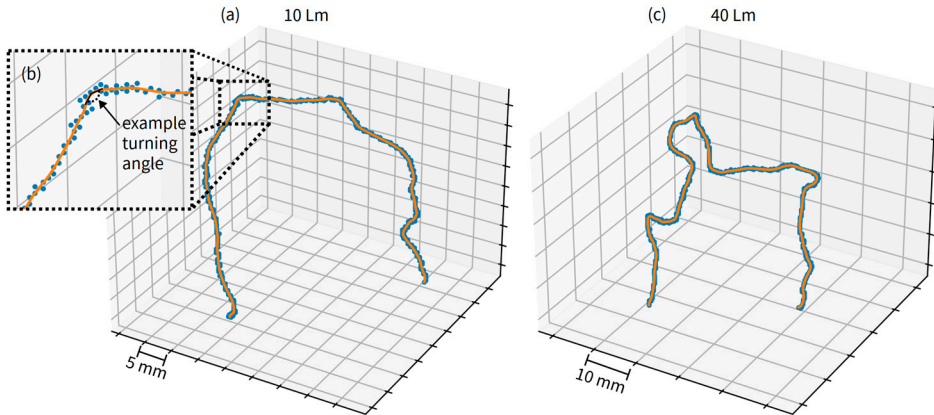
Figure 3.9: Two examples of extracted arcs, (a) from flow at 10 L/min and (c) from 40 L/min. The blue points indicate voxel coordinates of the arc while the orange curve is the interpolated arc coordinates of the arc path. The zoom in (b) illustrates how a turning angle can be extracted from the interpolated curve.

Figure 3.10 presents quantified 3D length distributions, showing that the mean length initially increases from approximately 175 mm at 10 L/min to about 190 mm at 20 L/min. Subsequently, the mean length begins to decrease around 30 L/min, reaching 160 mm at 40 L/min. The initial length increase can likely be attributed to the increase in airflow, which causes the plasma arc to expand. However, between 20 and 30 L/min, excessive turbulence generated by this expansion disrupts the arcs, making them unsustainable. Additionally, variations in the standard deviation σ of 3D length are evident between flow conditions, with 10 L/min having σ of 57 mm and 30 L/min as high as 76 mm. This variation is believed to be linked to the increasing number of viable arc pathways due to higher turbulence.
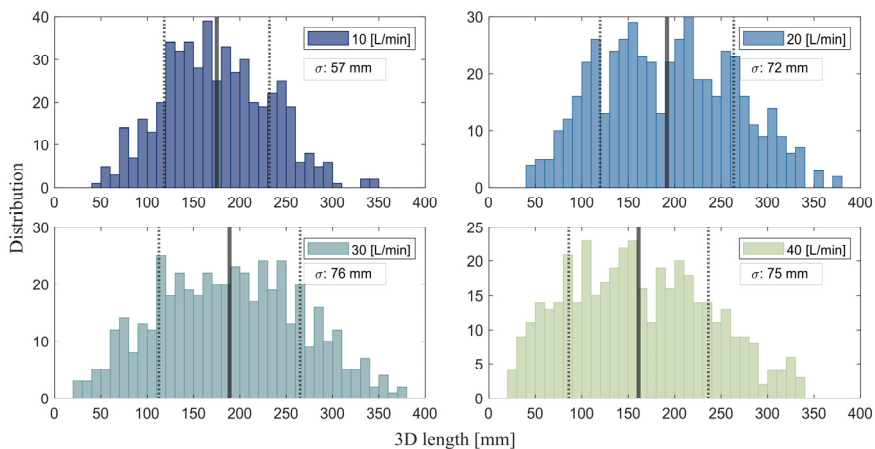

Figure 3.10: Distribution of measured 3D length at each flow rate. Solid line indicated standard deviation.

Comparisons between the quantified 3D length and the 2D length were conducted by projecting the reconstructed arc path along the axis perpendicular to the anode-cathode plane, creating an optimal image from which the 2D arc length could be extracted. Figure 3.11 (a) and (b) illustrates the anticipated trend of underestimating arc length when employing 2D projection [84].

Variation in difference between 3D and 2D length measurements was observed across different flow cases as presented in Figure 3.11. Discrepancies were observed of approximately 10% at 10 L/min, 14% at 20 L/min, 14% at 30 L/min, and up to 15% at the highest tested flow rate, 40 L/min. This discrepancy is linked to the loss of depth information in 2D projections, which, in turn, is influenced by how much the arc curves.
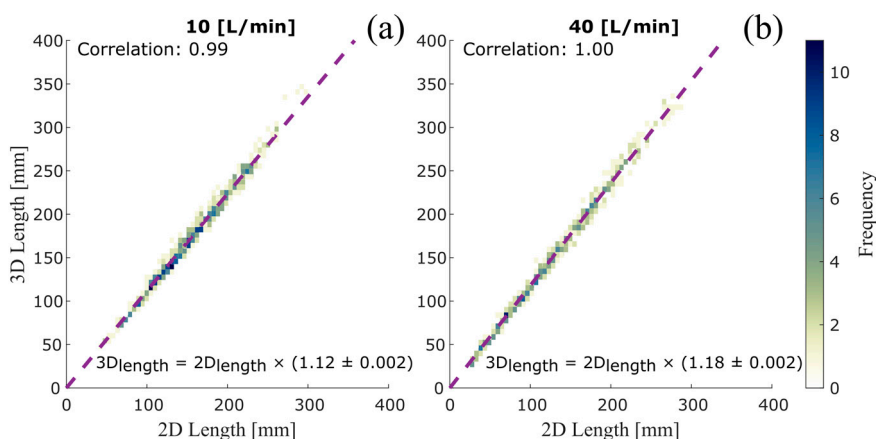
Figure 3.11: Correlation histograms between 3D length and 2D length at flow rates of 10 L/min and 40 L/min, equation shows proportionality.

A main feature of 3D emission tomography is the ability to quantify arc volume. Arc volume was extracted by using a global threshold of $3 \cdot 10^4$ counts, as illustrated in Figure 3.12, to eliminate reconstruction artefacts. All voxel values exceeding this threshold and connected to the previously identified arc coordinates determined by a connected components algorithm with 6-connectivity were considered part of the volume. Subsequently, the volume was determined by multiplying the count of identified arc voxels by the volume of each voxel, which was 0.5^3 mm^3, in order to obtain the complete arc volume.
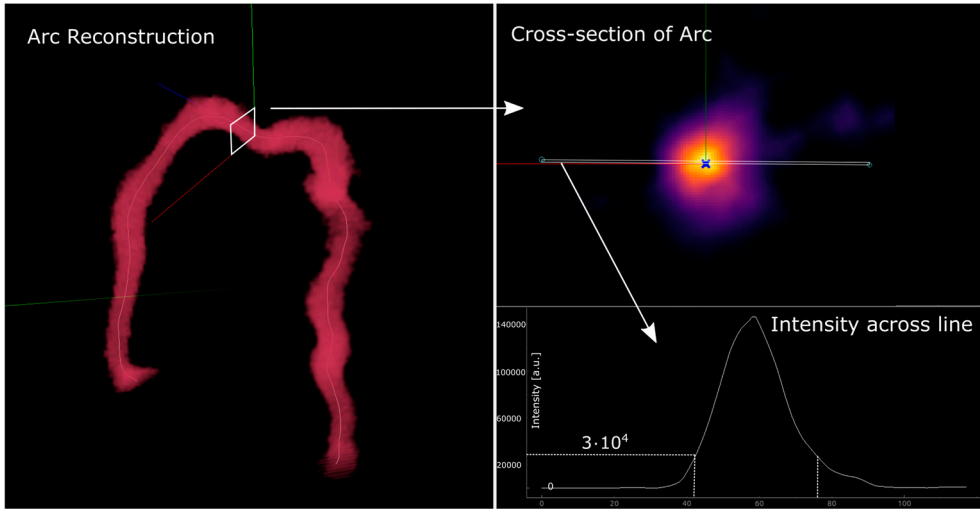
Figure 3.12: Illustration of selection of intensity treshhold for volumetric investigations.

A decreasing trend in the mean arc volume was observed as airflow rate increased, as shown in the panels of Figure 3.13 (a). This indicates a reduction of approximately 55% in volume when transitioning from 10 L/min to 40 L/min. Additionally, the standard deviation σ showed a decrease with increasing flows, dropping from 947 mm³ at 10 L/min to 515 mm³ for 40 L/min. As the flow rate increased, there was a decreasing proportionality constant between volume and 3D length, as evident in Figure 5 (b-e). This trend is believed to be primarily attributed to an increased in turbulence, which shortens arc residence times and subsequently reduces the number of locally excited species. Such a reduction in excited species weakens the luminescence around the arc centre, resulting in a reduced arc volume.

Plasma arcs displaying deviations from the norm were identified as outliers and are highlighted with both red and blue circles in Figure 3.13 (b-e). The outliers situated above the proportionality lines are marked with red circles and correspond to arcs containing shortcuts. An example of an outlier with a shortcut is illustrated in Figure 3.13 (b), indicated with an arrow. Shortcuts result in a shorter measured arc length as they follow the shortest path but the residual luminescence field just before the shortcut still contributes to the volume, leading to an increased volume to 3D length ratio. Shortcuts were observed slightly more frequent at flows of 40 L/min, which can be attributed to the increasing arc curvature that promotes pathways with lower resistance than the current one, thus increasing the likelihood of shortcuts.

Figure 3.13: (a) Distribution of measured volume at each of the four flow rates, solid lines show mean value and dashed lines show standard deviation σ. (b-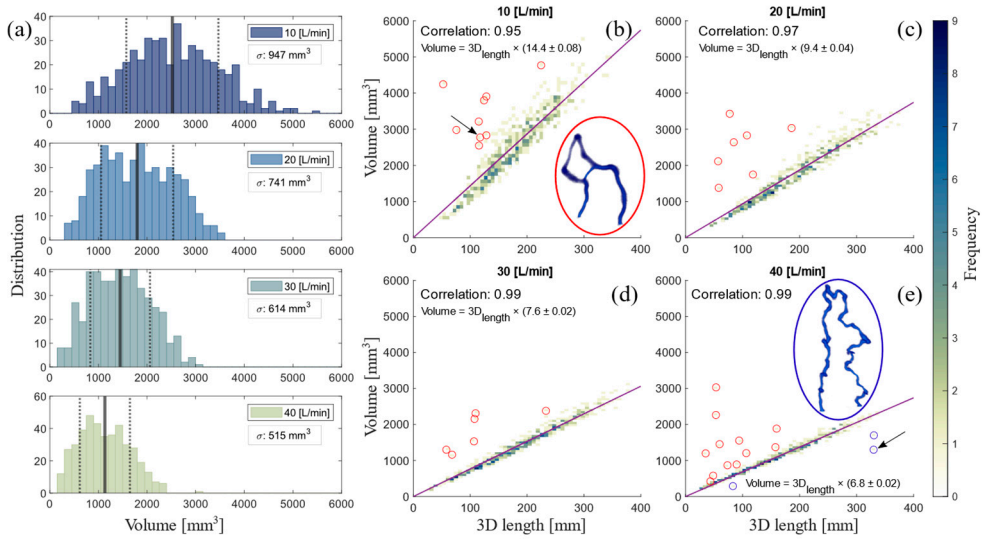e) Correlation histograms between volume and 3D length for each of the four flow cases, equation shows proportionality. Outliers are indicated by red (shortcut) and blue (volume overlap) circles. Example reconstructions of a red and blue outlier, indicated by arrow, and shown inside the large red and blue circles in (b) and (c).

Outliers situated below the proportionality lines are marked with blue circles, signifying arcs with extensive volume overlap owing to curvature. Figure 3.13 (e) showcases a reconstructed example of one such blue outlier, indicated with an arrow. These outliers were less common and exclusively appeared in the 40 L/min case. They are likely a combined result of turbulence and reduced arc residence time. Investigating such outliers and more could present valuable opportunities for future research, offering a more comprehensive understanding of various flow conditions.

The proposed methodology aims to enable flexible reconstruction of plasma luminosity fields in three dimensions. This technique can be implemented on its own or in combination with other techniques and is not limited to gliding arcs but can be extended to various other plasma systems with optical access. For additional information regarding this work please refer to paper I.

3.3 Stereoscopic high-speed imaging of iron microexplosions

Metallic fuels have gained considerable interest as a potential carbon-free energy carrier [90]. Their relevance is particularly pronounced within the realm of energy storage and transmission technologies [91, 92], where the utilization of recyclable fuels, powered by primary renewable sources like wind and solar energy, presents a promising avenue. Iron has emerged as a highly appealing candidate due to its characteristics, such as a high energy density and significant heat release during combustion [91, 93]. To achieve good recyclability of metal fuels, like iron, and to optimize efficiency, it is imperative to develop a profound understanding of their burning processes and properties.

In this work, the combustion characteristics of iron particles (d_{50} = 70 μm) introduced into a laminar diffusion CH_4/air flame produced with a customized Mckenna flat-flame burner were investigated. The focus was to explore the commonly observed micro-explosion phenomena during combustion of micron-sized iron powders [94, 95]. These microexplosion processes can impact both product formation and the overall stability of combustion, rendering them highly interesting for investigation.

To enable large field of view 3D particle imaging of burning iron particles velocity and microexplosion characteristics, a stereo configuration consisting of two high-speed cameras (Phantom VEO710L CMOS) was employed. A schematic of the setup is presented in Figure 3.14. These two cameras were positioned in the same horizontal plane, situated at a distance of 185 mm from the centre of the burner. Nikon objectives featuring a focal length of 50 mm and a f-number of 5.6 were utilized for each of the two cameras, along with a 12 mm extension ring. Exposure times in both camera setups were adjusted between 2 μs and 10 μs to enable either higher temporal resolution or increased signal intensity. Each camera possessed a native resolution of 1280x800 pixels, with individual pixels measuring 20 μm and a 12-bit depth. The resolution was later decreased to 1280x600 pixels to achieve a frame rate of 10 kHz.
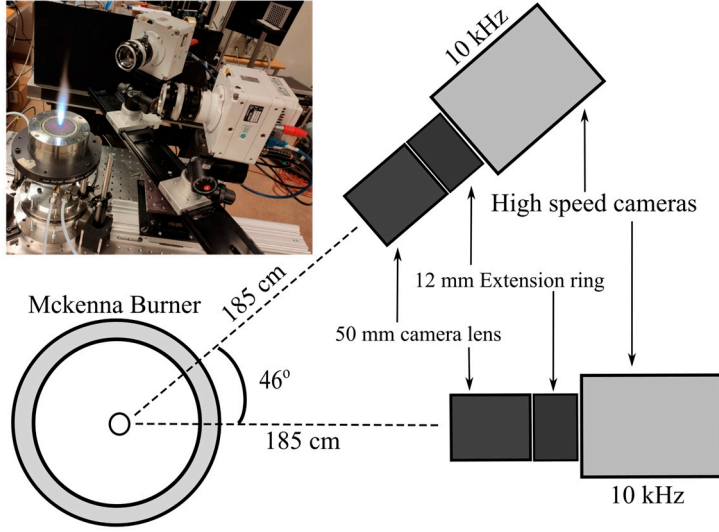
Figure 3.14: Schematic of experimental setup incorporating a stereoscopic camera arrangement.

To perform 3D tracking using a stereoscopic setup it is beneficial to have the cameras viewing angle at a large separation. However, the larger the separation angle is the harder it might become to match image points between the two cameras. Therefore, a separation angle of 46° was selected in this work to achieve a compromise between stereoscopic 3D information and ease of particle matching.

The 3D particle positions were acquired using a simple tracking method based on the pin-hole camera model, described in the camera model section 2.3. Following camera calibration, the estimated camera matrix parameters presented in Equation (15) were used to compute the 3D particle positions. This process is done by computing the intersections between projected camera pixel rays originating from particles detected in each camera, illustrated in Figure 3.15. Initially, particle locations in each of the two camera images were identified through threshold segmentation. This approach was suitable because the burning particles were significantly brighter than the overall background illumination. Thereafter, centroids of these segmented particle regions were computed, and used as origins for the projected pixel rays. By identifying the intersections or the closest points between the projected rays from the two cameras, the 3D positions of the particles were determined. The intersections of these rays can be determined by initially solving a linear system of the following form

$$\begin{pmatrix} \lambda_1 \\ \lambda_2 \end{pmatrix} = \begin{pmatrix} \|v_1\|^2 & -v_1^t v_2 \\ -v_2^t v_1 & \|v_2\|^2 \end{pmatrix}^{-1} \begin{pmatrix} -v_1^t(q_2 - q_2) \\ -v_2^t(q_1 - q_2) \end{pmatrix},$$

(21)

41

where v_1 and v_2 are the ray direction vectors, q_1 and q_2 their respective origin, λ_1 and λ_2 intersection scalar values. The sought intersection point P_i can then be found by calculating the point in between the two closes ray-points using the scalar values λ_1 and λ_2 from above

$$p_1 = q_1 + \lambda_1 v_1, \quad p_2 = q_{21} + \lambda_2 v_2 \qquad (22)$$

and then the point in between

$$P_i = p_1 + \frac{1}{2}(p_2 - p_1) = p_2 + \frac{1}{2}(p_1 - p_2). \qquad (23)$$

This routine was performed for every frame in high-speed sequences enabling 3D trajectory tracking and 3D velocity measurements of individual particles. Low seeding density of iron particles was maintained during this study. It is important to emphasize that in situations with a high seeding density, the quantity of projected rays significantly rises, making the task of matching these rays more challenging [96]. Additional efforts would be necessary to accurately estimate the correct 3D positions in such cases. The evaluation of particle position uncertainty was conducted by examining the re-projection error, as detailed in section 2.3. The maximum observed error ranged between 1-3 pixels (20 μm pixel size), with the larger errors typically occurring at the edges of the regions of interest.
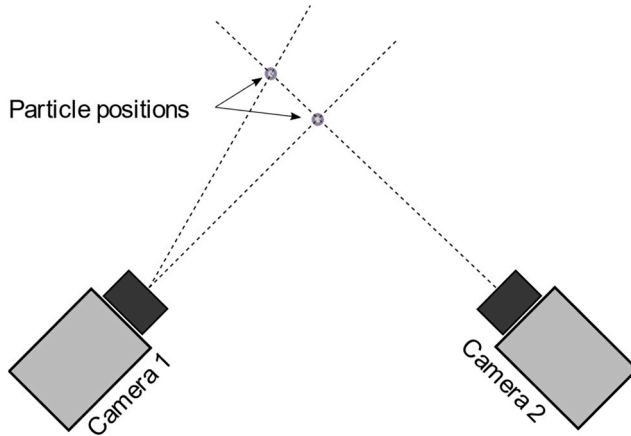
Figure 3.15: Illustration of particle positions from intersections between projected camera pixel rays, rays originate from particles detected in the cameras.

The observed microexplosions occurred prior to particle burning extinction, leading to change in trajectories, velocities, radiation intensities, and eventually fragmentation into multiple smaller particles. In Figure 3.16 (a) and (b), the reconstructed 3D path of a burning iron particle undergoing an explosion and the resulting fragments are displayed. These fragments were observed to have a

tendency to produce planar structures as presented in Figure 3.16 (b). It is important to note that only the brighter fragments were trackable, resulting in the loss of many smaller fragments that were initially observed during the explosion event but quickly became undetectable due to their rapid reduction in intensity.
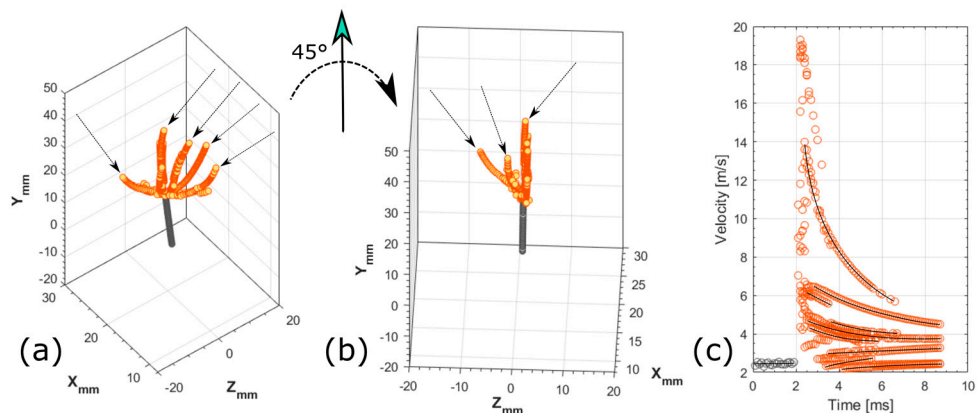

Figure 3.16: (a) Gray dots show 3D burning iron particle path pre-explosion and orange dots displays fragment paths post-explosion of one single explosion. (b) Another perspective of the explosion seen in (a), arrows indicates individual fragment paths. (c) 3D velocity at different consecutive time steps, solid lines are there to indicate individual fragments.

The initial particle velocity and explosion fragments velocities are shown in Figure 3.16 (c). Following, the microexplosion event seen at 2 ms, the 3D velocity of the majority of fragments showed a significant increase, typically reaching two to six times their previous velocities within 0.2 ms. Thereafter, the velocities of these fragments gradually converge towards the initial particle velocity as expected.

The post explosion fragments were observed to quickly burn out possibly due to higher specific surface area of the fragments yielding improved reactivity but a dominant increased heat loss post explosion. The microexplosion of burning particles could be attributed to internal gas expansion [97, 98] and influenced by the temperature of the hot gas products and the concentration of oxygen. The intensity and likelihood of a microexplosion are closely linked to the rate of gas generation and its expansion rate inside of the particle [99].

The formation of planar microexplosion structures was believed to be related to the vaporization of liquid iron. A tendency to generate tangential stress combined with any accumulated tension could increase the likelihood of a line-shaped opening that releases fragments into a two-dimensional plane. Microexplosions have the potential to influence fundamental combustion characteristics in iron combustion. Thus, a comprehensive understanding of this mechanism has the potential to enhance iron particle combustion in practical applications.
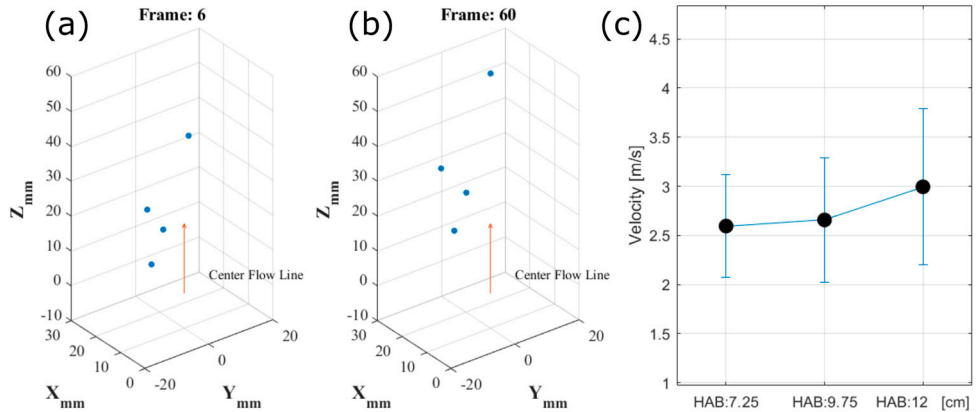
Figure 3.17: (a) 3D positions of burning iron particles. (b) 3D positions of the same burning iron particles at a later stage. (c) Mean particle 3D velocity at different HAB.

Figure 3.17 (a) and (b) displays detected 3D positions of burning iron particles as they traverse the combustion flow. The mean 3D particle velocity, presented in Figure 3.17 (c), demonstrates a velocity increase at higher HAB while simultaniusly showing significant standard variation. The velocity velocity is believed to be the result of multiple factors, including self-propulsion originating from the iron vaporization process, buoyancy effects, and particle mass reduction due to the significant release of iron oxides during combustion.

However, it is important to highlight that this study was not able to capture the entire velocity profile, from the initial seeding position to the maximum flame height, due to field of view limitations of the cameras. Nevertheless, an increase in particle velocity has been previously documented in a comparable type of burner [97]. Future improvements to this work would be to increase the field of view of the cameras and apply more advanced tracking algorithms to both increase the accuracy of the results and enabling higher seeding densities. Hopefully such improvements would yield an even better understanding of these types of processes.

4 Laser diagnostics

This chapter serves as an introduction to different 0D and 2D laser-based techniques employed in work within this thesis, presented in papers IV, V, VI, VII, and VIII. The techniques encompass a wide spectrum, including PIV for visualizing gaseous or liquid flow fields, LIF for molecular species investigation, shadowgraphy for particle visualization and thermographic phosphors for surface temperature measurements. Each technique description is subsequently accompanied by an experimental application, showcasing its practical implementation and efficacy.

4.1 Particle image velocimetry

The PIV technique operates based on the fundamental principle of identifying and tracking the movement of particles within a studied liquid or gaseous medium, whether reacting or non-reacting, to extract the velocity field of the medium. These tracer particles are either already part of the studied flow or intentionally seeded into the flow. As an optical method, PIV is regarded as non-intrusive, in contrast to the application of physical sensors.

In general, PIV is commonly employed as a planar technique to acquire 2D flow field information. This feature makes it compatible with other planar imaging methods, such as planar laser-induced fluorescence (PLIF), enabling simultaneous acquisition of velocity field and species information. The technique has been extended to 3D using both stereoscopic PIV [100] and tomographic PIV [43] thus allowing for 3D flow field acquisition. PIV has found extensive application in combustion diagnostics and other flow studies where tracer particles are illuminated using laser radiation, enabling the imaging and tracking of the particles through their Mie scattering of the laser light [101].

Sequential laser pulses are commonly utilized in PIV, these pulses are subsequently expanded into a thin sheet to pass through the investigated flow field. The ability of lasers to produce strong illumination at short pulse durations is advantageous as pulses with durations in the order of 10 ns provide short exposure times, preventing image blur of tracked particles at both low and high velocities. Synchronized with camera acquisitions, these laser pulses allow for the capture of sequential images, where the displacement of particles between consecutive images can be measured.

By tuning the time interval Δt between laser pulses, high-velocity flows can be accurately mapped, as particle displacement is averaged over this interval.

One commonly used approach to evaluate particle displacement between consecutive data images is through cross-correlation. This method involves segmenting each image into smaller regions called interrogation windows (IWs). The particles within these IWs are then matched and cross-correlated across sequential images, as depicted in Figure 4.1, resulting in both particle velocity direction and magnitude, enabling flow characterization [100]. To achieve optimal performance, it is essential to ensure uniform and relatively high particle density.
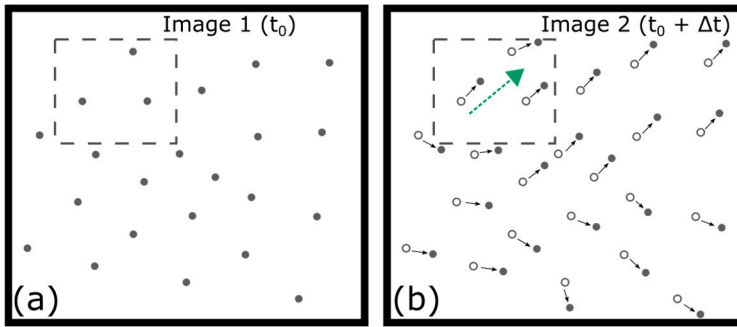

Figure 4.1: Illustration of PIV cross-correlation between two images in sequence. Dashed square depicts a IW and the green arrow in (b) illustrates the resulting velocity vector.

The size of the IW is a critical factor in determining the resolution of the resulting vector field, as each window corresponds to one vector. For instance, larger IWs, such as 32 by 32 pixels, will generate fewer vectors compared to smaller window sizes, like 8 by 8 pixels. However, it is essential to ensure a sufficient number of particles within the IW to achieve strong correlation. Additionally, for optimal performance and to minimize in-plane losses, the particles should not move more than a quarter of the full IW's distance [100, 102]. Consequently, selecting the appropriate size for the IW must consider factors such as flow speed and particle density to ensure reliable and precise results. In practical flows, such as combustion applications, achieving a homogeneous seeding density can be challenging due to thermal gas expansion, leading to IWs with varying degrees of particle numbers. One proposed approach to overcome this challenge is to adapt the IW size depending on the local particle density [103]. Multi-pass techniques utilizing adaptive cross corelation have been created working towards increased spatial resolution and higher dynamic velocity range [102].

An alternative evaluation method to cross-correlation is known as optical flow, which has proven to be successful in PIV measurements [104, 105]. One key advantage of optical flow is its ability to provide a velocity vector for each pixel in the measured sequence images, offering a higher spatial resolution. However, it is

important to note that this technique relies on a consistent signal intensity of the seeded particles, which can be challenging to achieve in practical scenarios [106, 107].

Special attention must be given when dealing with flows requiring seeding of tracking particles, such as combustion or gas flows. In such scenarios, particle selection becomes critical to ensure their size is sufficiently small for precise flow tracking while retaining enough signal strength for accurate tracking without being prematurely consumed, particularly in the context of combustion flows. In certain cases, particle seeding might not be viable, particularly in hypersonic flows where particles sometimes fail to follow the flow adequately. In such situations, alternative techniques like molecular tagging velocimetry can be employed. Such methods track the emitting light from excited gas molecules within the studied gas flow [108, 109], offering a viable alternative for extreme flow characterisation.

4.1.1 Particle image velocimetry in a lab-scale gas turbine model combustor

Syngas is a gas mixture predominantly comprised of H_2 and CO, that can be produced through the gasification of feedstocks like coal, biomass, and waste [110, 111]. The use of such high H_2-content fuel blends in gas turbine engines can possibly reduce CO_2 emissions. However, the utilization of any such H_2-rich fuels can be challenging due to distinct attributes of H_2 such as high diffusivity and high flame speed resulting in significant changes in the operating conditions in applications such as gas turbine engines [112]. To address this, syngas and other high H_2-content fuels are frequently diluted with additional species, including N_2, CO_2, or Argon. Such additives serve as countermeasures against high flame temperatures or flashbacks that in turn leads to reduced NO_x emissions. Another essential objective becomes to understand how fuel composition and dilution with additive species changes flame stability limits to ensure safe operation of the combustion device.

This study explored effects of CO_2 dilution in syngas combustion. The investigation was conducted in a laboratory-scale gas turbine model combustor, specifically designed to replicate the Siemens DLE (Dry Low Emission) burner. PIV together with LIF and flame luminescence imaging were employed. Focus was on studying the combustion flow field at atmospheric pressure conditions.

The experiments were performed at a constant Reynolds number (Re) of 10000 and the resulting flame and flow structures were studied at two different CO_2 dilution levels of 15% and 34% mole fraction respectively in the syngas/CO_2 mixture. The syngas mixture itself consisted of H_2, CO, and CH_4.

An illustration of the experimental setup can be seen in Figure 4.2. The light source in the high-speed PIV system was a diode-dumped, dual cavity Nd:YLF laser (Litron LDY304-PIV) operated at a wavelength of 527 nm. Titanium dioxide (TiO_2)

particles of a size around 1-10 μm were seeded into the flow and the scattered laser light was captured with a high-speed camera (Phantom v311) using a 70 mm Nikon objective with f-number 5.2 combined with a 12 mm extension. The camera resolution was 1280×1080 pixels with a frame rate of 1 kHz and individual pixel size of 20 μm at 12-bit depth.
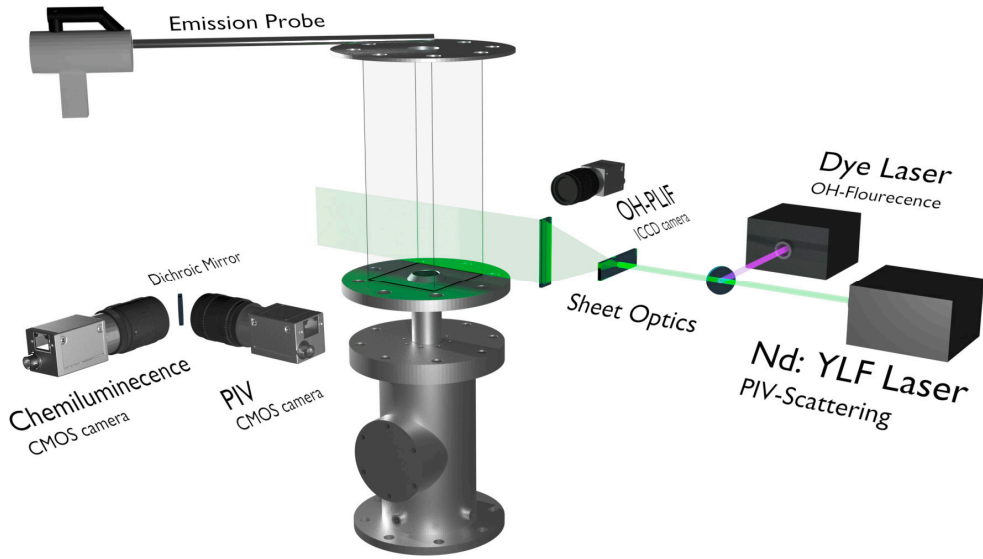

Figure 4.2: Schematic illustration of the experimental setup

In Figure 4.3 (a), pure syngas combustion is presented, without any CO_2 dilution, while Figure 4.3 (b) illustrates the maximum 34% CO_2 dilution case. The PIV images underwent processing using a multi-pass cross-correlation algorithm, initially employing an IW size of 64 by 64 pixels for the first pass, and subsequently reducing it to 32 by 32 pixels for the final pass. An IW overlap of 50% was applied, and vectors with velocity magnitudes exceeding 15 m/s were deemed erroneous and consequently excluded. Each vector field is superimposed onto a corresponding grayscale LIF image, showing the simultaneous distribution of OH. This showcases the versatility of PIV, allowing not only the visualization of the overall flame velocity field but also the identification of finer details such as vortices. Furthermore, the velocity field displays the inner recirculation zone surrounding the central axis of the burner and the outer recirculation zones located in the lower-left and lower-right corners. The fuel/air mixture then flows into the combustor region situated between these two recirculation zones.
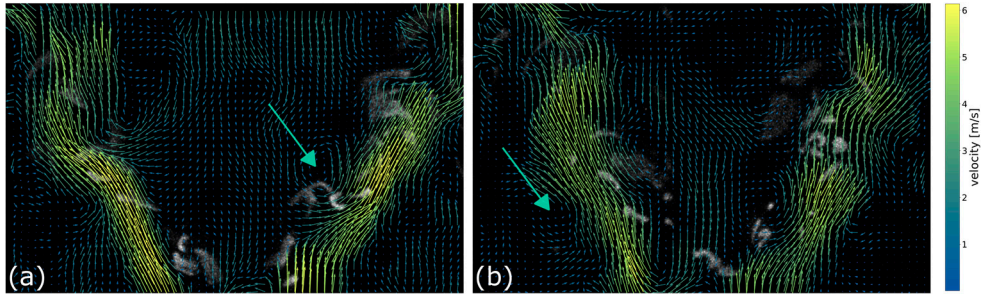
Figure 4.3: Instantaneous flow field images of syngas combustion without dilution (a) and syngas combustion with a 34% CO2 dilution (b). Vortices are highlighter with cyan arrows.

Moreover, Figure 4.4 illustrates how CO_2 dilution affects the average flow fields. The mean flow data was produced by averaging 3000 instant velocity field snapshots, equivalent to a duration of 3 ms, for each flame. Each individual PIV image was generated using a multi-pass cross-correlation method, starting with an initial IW size of 64 by 64 pixels, and subsequently reducing it to 16 by 16 pixels, with a 50% overlap.
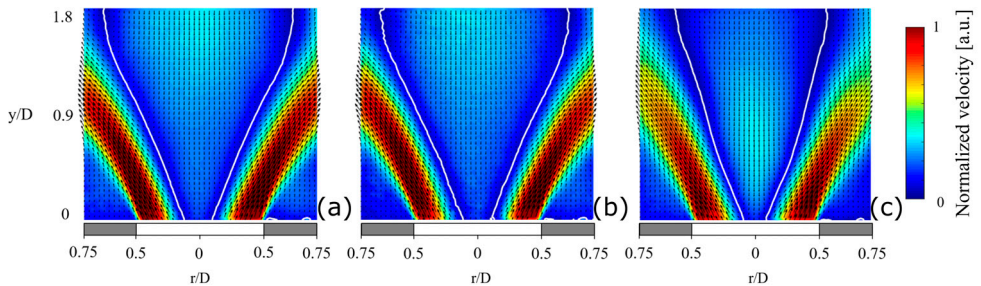
Figure 4.4: (a) Average flow field of syngas combustion with no CO2 dilution. (b) Average flow field with 15% dilution. (c) Average flow field with 34% dilution.

As illustrated in Figure 4.4, the influence of CO_2 dilution on the inner recirculation zone, characterized by zero axial velocity, is evident. These inner recirculation zones here shown using white lines, with Figure 4.4 (c) corresponding to 34% dilution displaying a smaller zone compared to the larger zone seen in Figure 4.4 (a), which corresponds to no dilution.

This aspect is further emphasized in Figure 4.5, where the widths of the inner recirculation zones for all three mixture cases, along with a reference case of cold flow is presented. Here the expected expansion of the inner recirculation zone can be observed, caused by thermal expansion of the reactive gases influencing various velocity components.

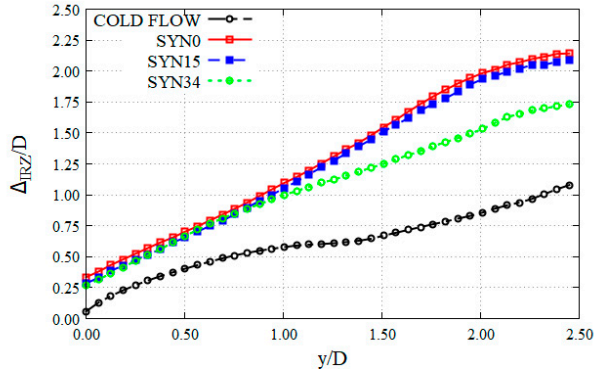**Figure 4.5:** Width of inner recirculation zone along the burner centerline for each of the tested syngas mixtures together with an cold flow reference case.

Given that the three resulting flames possess close to a linear relationship in terms of laminar flame speed and adiabatic flame temperature, it is reasonable to anticipate a similar relationship in the mean flow field.

However, the distinct difference in the mean flow structure observed during 34% CO_2 dilution can most likely be attributed to the flame-pocket structure, which results in a lower mean heat release rate. This decreased mean heat release rate aligns the flow field more closely with an isothermal (cold) flow, thereby resulting in a narrower inner recirculation zone in the radial direction and more unburnt fuel.

Achieving homogenous seeding density within this burner configuration posed a challenge due to varying density zones within the burner. The tendency of the flame to displace seeding particles outward, resulted in the interior flame structures being harder to resolve than exterior structures. While increasing the seeding density could partially address this issue, it would also render the technique more intrusive. Therefore, a trial-and-error approach is advised when determining the optimal seeding strategy for a specific application.

4.2   Laser-induced fluorescence

LIF stands out as a versatile and widely utilized laser diagnostic technique for investigating atoms and molecular species. At its core, LIF focuses on studying the phenomenon of spontaneous emission, commonly known as fluorescence. This emission occurs when molecules or atoms relax from an excited energy level down to their ground state after excitation by an energy source. The excitation process in LIF is performed by laser irradiation, tuned to match a specific energy transition of the species of interest. As a non-intrusive technique, thanks to its purely optical

(photon-in, photon-out) nature, LIF allows for investigations of characteristics such as species distributions or temperature fields [101].

The unique molecular absorption and fluorescence spectra of a species enables this technique to conduct species-specific investigations in complex environments with multiple species present. Fluorescence can not only occur at the excitation wavelength (known as resonant fluorescence) but also at other wavelengths, predominantly shifted towards longer wavelengths. This characteristic becomes advantageous when detecting fluorescence at non-resonant wavelengths, as it reduces disturbances from stray laser light or Mie scattering caused by particles. The technique can allow for both qualitative and quantitative measurements of species distributions and concentrations, leading to its widespread application in various fields, such as plasma diagnostics [113], combustion diagnostics [101], and medicine [114].

LIF in combustion research allows studying of pollutants, combustion radicals and intermediates species with high sensitivity enabling precise investigations, ranging from point measurements and planar imaging [115, 116] to volumetric laser-induced fluorescence [117-119]. As detector a photo multiplier tube (PMT) for point investigations or a camera for 2D measurements can be used. Generally, 3D measurements are achieved through multiple cameras adopting a tomographic approach with volumetric laser illumination or a single camera combined with a scanning laser sheet to effectively scan the probed volume.

In certain applications, such as flame visualization in combustion research or spatial molecular investigations in plasma research, qualitative information often proves sufficient. However, when aiming for quantitative measurements like absolute concentration, the consideration of LIF quenching becomes essential. The deexcitation of excited molecules or atoms through competing processes such as dissociation, chemical reactions, and collisional quenching can pose challenges in practical applications. Addressing these quenching effects becomes crucial for ensuring accurate and reliable quantitative results.

Collisional quenching is the primary source of non-radiative losses, disrupting the linear proportionality between the number density of the probed species and the emitted fluorescence signal. This disruption makes it challenging to accurately quantify the concentration based solely on the recorded signal, as the quenching effect depends on factors such as pressure, temperature, and the local species composition.

One approach to reduce the effect of quenching in LIF measurements is to utilize Fluorescence Lifetime Imaging (FLI) to capture the excited species-specific lifetimes within the probed volume. The extracted lifetime is proportional to the quenching rate, facilitating compensation during quantitative measurements. FLI employs dual time-gated camera detection of the emitted fluorescence, wherein two or more scientific cameras image the probe volume using different gate times, effectively capturing different parts of the LIF signal. This enables the generation of a two-dimensional lifetime image by analysing the differences between the two

measured images, employing techniques like Rapid Lifetime Determination (RLD) [120] algorithms or Dual Imaging and Modelling (DIME) [121, 122]. For further information regarding FLI, refer to paper VI.

4.2.1 Laser-induced fluorescence in a lab-scale gas turbine model combustor

Modern gas turbines are required to push towards reducing CO_2 emissions and other pollutants like NO_x and CO, all while adapting to a diverse range of fuels. Consequently, the development of fuel flexibility in gas turbine combustors is a vital objective. This flexibility must be attained while ensuring that emissions remain within acceptable thresholds and without compromising the overall efficiency of the device. A commonly embraced approach to simultaneously reduce NO_x and CO_2 emissions involves running the combustor under lean premixed or partially premixed conditions [123-125], employing low-carbon content fuels [125-127]. Additionally, the utilization of lean premixed combustion in combination with hydrogen presents an emerging solution for advancing clean energy production [128, 129]. Nonetheless, using pure H_2 in gas turbine engines can pose technical challenges, primarily due to the elevated flame speed of hydrogen and the high gas product temperatures, which can lead to increased NO_x emissions. Hence, a blend of methane and hydrogen emerges as a potential middle ground, offering a compromise between emission levels and operational safety for existing combustor technology.

This work investigates the impact of pilot flame and fuel composition on the structures and stabilization of swirling turbulent premixed methane/hydrogen/air flames within a laboratory scale gas turbine model combustor. Flames under stable and close to lean blow-off (LBO) conditions were studied for two hydrogen/ methane fuel mixtures characterized by a hydrogen mole ratio of 0 and 50 % respectively. The studied flames had a constant Reynolds number of 20000 with different equivalence ratios. Two pilot-to-global fuel ratios were investigated at 2 % and 6 % by volume, with the pilot-to-global air ratio consistently held at 2 %. Data for non-piloted flames were also acquired for comparison. The experimental setup, as detailed in section 4.1.1 regarding particle image velocimetry within a laboratory-scale gas turbine model combustor, was also employed in this work, as depicted in Figure 4.2.

Single shot LIF images of the OH radical during pure CH_4 combustion are showcased in Figure 4.6, revealing a pronounced contrast in the luminosity intensity of the OH layer between the LBO and stable combustion cases. Significant gradients in the OH-PLIF field can allows for estimation of the flame front position [130, 131].

As anticipated, cases close to LBO have reduced luminosity, primarily due to the leaner fuel-air mixture compared to the more stable cases. Furthermore, the OH layer presents a slightly discontinuous appearance, signifying localized extinction

of reaction zones. On the other hand, the stable cases display a more pronounced OH signal, indicative of a heightened combustion stability.

Pilot flame impact is also noticeable, for example in the LBO case with a 6 % pilot where shortly downstream of the pilot flame nozzles OH PLIF signals start to appear. These pilot flames are fuel-rich and, due to their high jet velocity compared to the laminar flame speed under fuel-rich conditions, lifts off the pilot nozzles. The OH radicals generated by the pilot flames are subsequently transported downstream, contributing to the stabilization of the main flame within the outer recirculation zone. The OH radicals seen in the piloted stable cases also suggests that pilot flames tend to anchor the main flame in the outer recirculation zone.
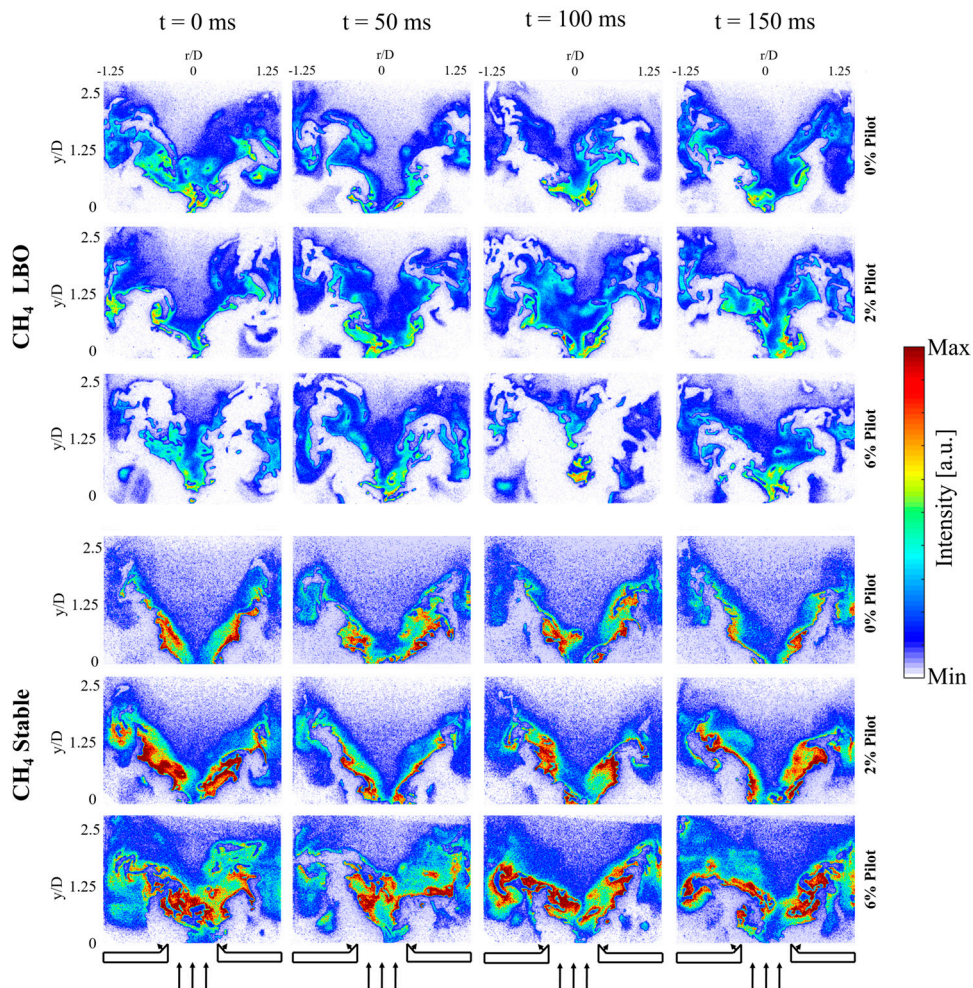

Figure 4.6: LIF image sequences of CH_4 combustion at different pilot flame fuel percentage, three LBO cases as well as three stable cases are shown.

For the hydrogen-enriched CH_4/H_2 mixtures, as depicted in Figure 4.7, more pronounced distinctions emerged between the stable and LBO cases. When operating under stable conditions, these hydrogen-enriched flames exhibited structures similar to their methane counterparts. However, during LBO conditions, the OH signal substantially diminished and became discretized, with signal appearing in small, isolated pockets.

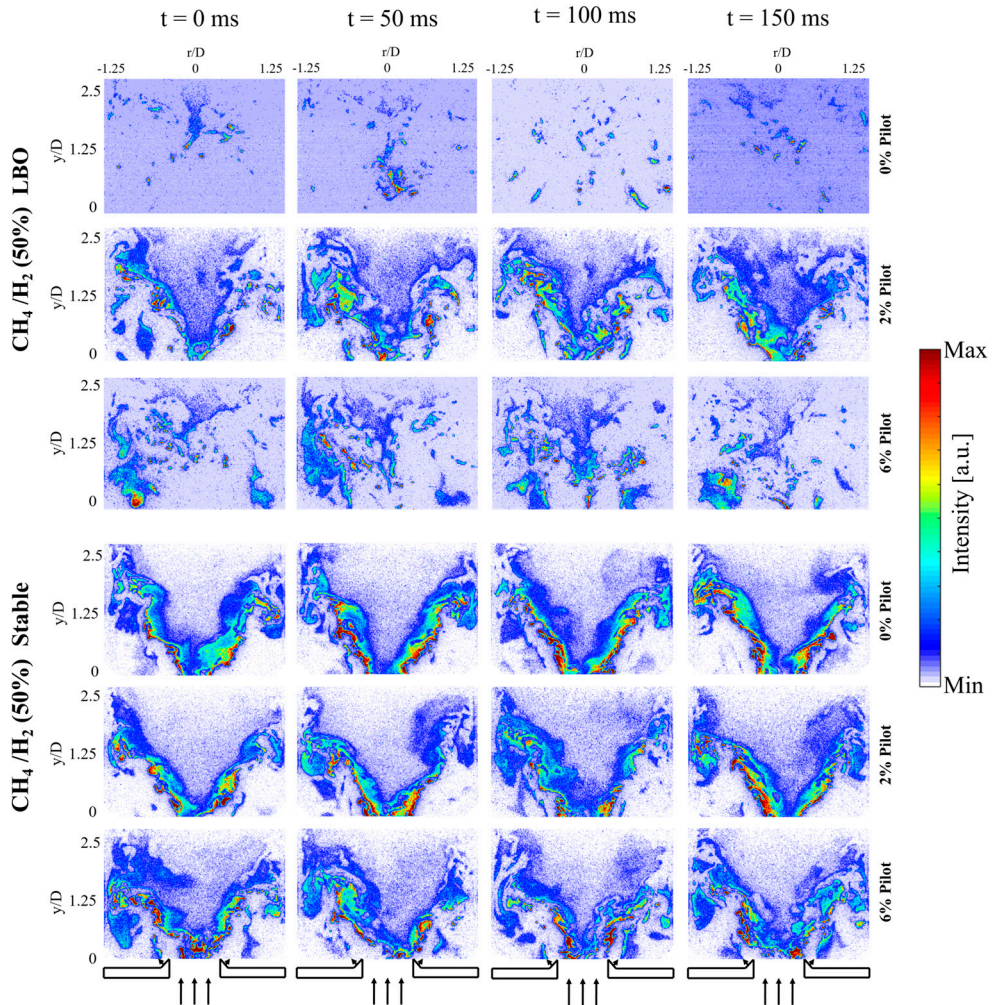**Figure 4.7:** LIF image sequences of CH_4/H_2 (50 %) combustion at different pilot flame fuel percentage, three LBO cases as well as three stable cases are shown.

Typically, hydrogen-enriched flames demonstrate OH layers that that are more fragmented and wrinkled when operating near LBO conditions, indicating disturbances within the reaction zone due to localized flame quenching [132]. This

phenomenon is likely a result of the high diffusivity of hydrogen, which causes it to diffuse and form relatively fuel-rich and fuel-lean regions respectively, causing different local reaction activity. The activation of pilot flames intensifies the OH signals, consequently giving flames such as the LBO 2 % case a flame structure resembling that of the stable 2 % pilot case. In general, pilot flames were observed to extend the overall operability range. The LBO equivalence ratio of the main flame decreased with an increase in the fuel mass flow rate in the pilot flames due to the increase of hot gas with a high OH radical concentration in the outer recirculation zone, which enhances the stabilization of the main flame. Hydrogen enrichment was also found to decrease the LBO equivalence ratio and improve resistance to LBO.

When performing optical measurements, such as these LIF investigations, these more practical apparatuses can present inherent challenges, often caused by restricted optical access. In this experimental setup, the combustion chamber featured a quartz liner, providing excellent optical access. Nevertheless, the task of aligning the laser sheet presented a challenge due to beam steering effects resulting from the positioning of the quartz liner in relation to the sheet-forming optics. Additionally, the potential for multiple reflections within the quartz liner posed a concern, especially when an effective filter combination capable of adequately blocking laser wavelengths was not in place. This challenge was further complicated by the necessity for overlapping LIF and PIV techniques to facilitate further simultaneous measurements.

4.2.2   Fluorescence lifetime imaging in gliding arc plasma

LIF is a widely embraced technique for its non-invasive characteristics and ability to selectively study molecules and atoms. This makes it highly valuable in plasma diagnostics [113, 133]. However, when striving for precise quantitative measurements, it becomes essential to consider the impact of quenching that will affect results.
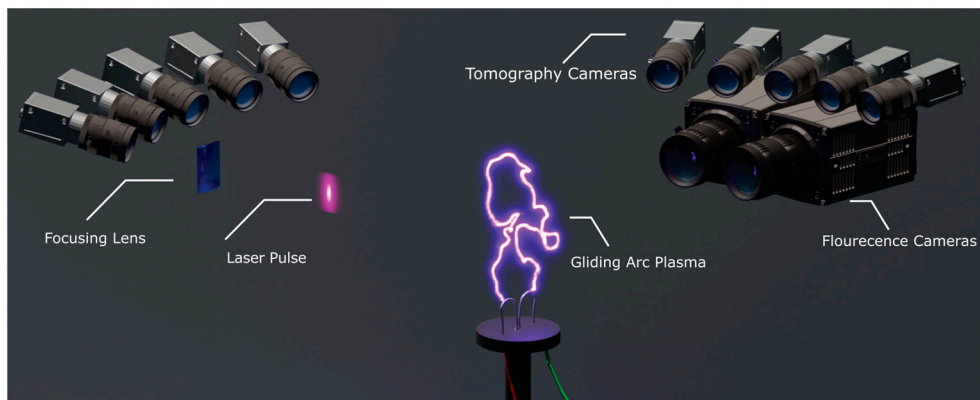
Figure 4.8: Illustration of the experimental setup. The depicted gliding arc is a rendition of a real discharge reconstructed using emission tomography.

To mitigate quenching effects, FLI can be employed to measure the lifetimes of the excited species of interest. However, due to the relatively short fluorescence lifetimes, picosecond laser pulses are sometimes required to accurately resolve these lifetimes [134, 135]. By combining such an excitation source with dual time-gated detection, techniques such as DIME can be applied to acquire lifetimes [121, 122, 136].

However, gliding discharges are very stochastic in both position and topology, therefore it can sometimes be hard to understand the observed fluorescence signal and in turn determine its origin. In this context, 3D emission tomography offers a promising solution by enabling the reconstruction of the entire luminescence field. This can provide valuable information about both the position and topology, facilitating the determination of measurement locations.

This work applied FLI and 3D emission tomography to achieve simultaneous instantaneous determination of OH fluorescence lifetimes in conjunction with 3D reconstructions of gliding arc discharges. By combining these techniques, it becomes possible to explore both the quenching of OH fluorescence and gain insights into the 3D spatial distribution of OH in the vicinity of the discharge.

The experimental setup was the same as the one described in section 3.2 regarding 3D emission tomography of gliding arc plasma with the addition of a 90 picosecond probe laser-sheet at 283 nm and two ICMOS cameras for 2D dual time-gated fluorescence detection, illustrated in Figure 4.8.
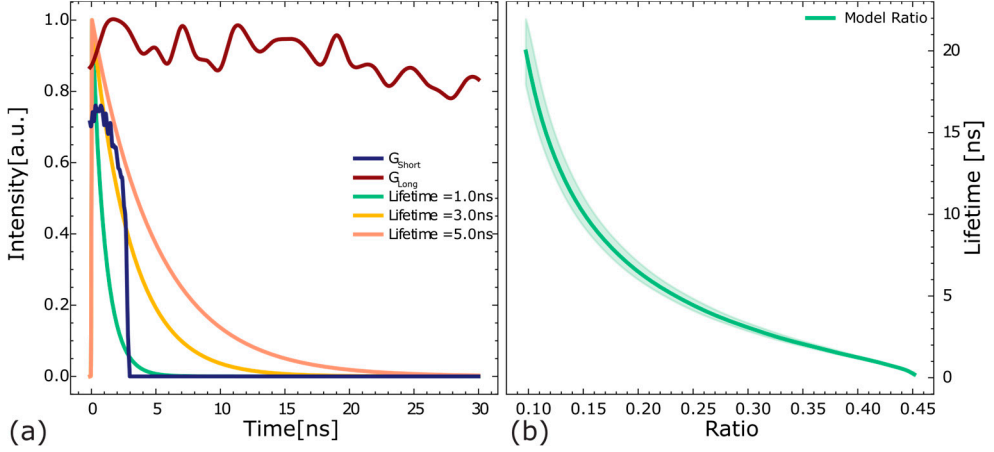
Figure 4.9: (a) Displays two gate functions together with decay time curves corresponding to different lifetimes. (b) Lifetime model containing relation between image ratio and lifetime.

Generally, rapid lifetime determination uses two LIF images where each pixel in the two images corresponds to the same location in the imaged volume. These two images are acquired using different camera gate settings to capture two different portions of the fluorescence decay curve. In Figure 4.9 (a) two gate functions G_{long} and G_{short}, used in this work are shown. G_{short} captures the initial portions of the decay curve while G_{long} can be seen to capture the whole curve. From the resulting images I_{long} and I_{short} an image ratio D which can be used to determine the fluorescence decay time can be calculated as follows

$$D = I_{short} \Big/ (I_{Short} + I_{long}) \tag{24}$$

The connection between the ratio image D and the fluorescence decay time is made through a model that takes into account both gate functions G_{long} and G_{short} as well as the decaying signal $S(t)$ yielding an estimate of the detected camera intensity.

$$I = \int G(t)S(t)dt \tag{25}$$

Here I is the detected camera intensity in one of the cameras and $S(t)$ is a mono-exponential function. Simulations of relative detected intensities for various fluorescence lifetimes allows a function to be estimated that takes an image ratio D and returns a unique lifetime τ, such a function is shown in Figure 4.9 (b). More details regarding the DIME evaluation algorithm and experimental considerations can be found in [121].
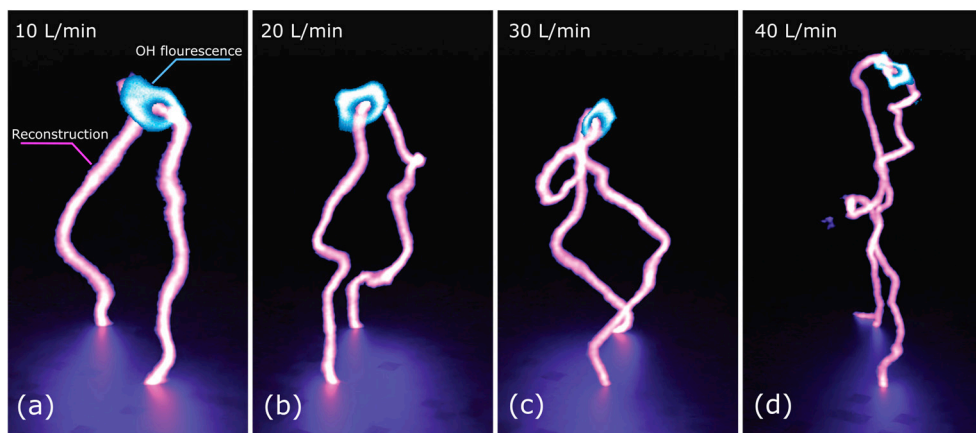
Figure 4.10: 3D emission tomography reconstruction of gliding arcs at airflows of 10, 20, 30, 40 L/min. Simultaneously captured OH fluorescence images, shown in blue, are combined with the tomographic reconstructions.

Simultaneous measurements of OH fluorescence images and 3D tomography of the gliding arc were conducted under ambient conditions, examining flow rates at 10, 20, 30, and 40 L/min. The combination of fluorescence imaging with 3D tomography offers valuable insights into the spatial distribution of OH around the gliding arc. Typical results are illustrated in Figure 4.10, showcasing the 3D tomographic reconstruction of the arc combined with LIF images. With increasing flow rates, the arc length expands, primarily due to vertical expansion caused by higher flows and additionally by a more complex arc structure arising from increased turbulence.

Furthermore, as the flow rates increase, a noticeable reduction in thickness of the arc is observed. This decrease is linked to diminished thermal effects, primarily coming from a shorter residence time. Therefore, both the N_2^* emission, which is the primary luminosity component generated by the gliding arc, and the OH region created by the arc see this reduction. The combination of these techniques emphasizes that the arc center is encompassed by OH, and that OH intensity increases towards the bulk and thereafter reduces towards the outer edges. This is further illustrated in Figure 4.11 showing a OH fluorescence image overlapped with a slice of the tomographic reconstruction along the same plane.
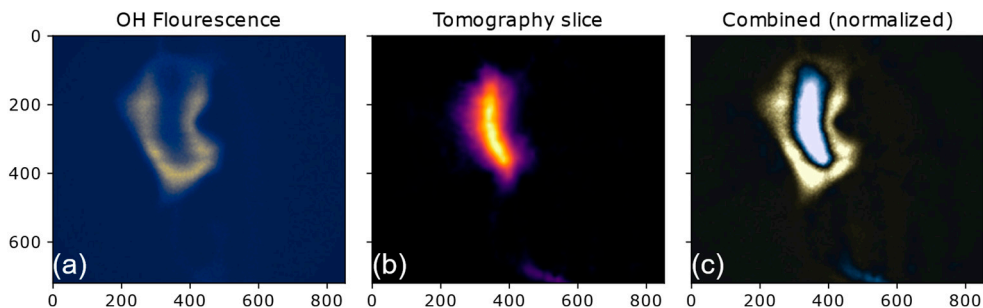
Figure 4.11: (a) OH fluorescence image. (b) Slice of the tomographic reconstruction at same at location as fluorescence in (a). (b) Overlapped OH fluorescence and tomography slice.

The collected fluorescence data primarily consisted of blank images where the laser failed to hit the arc or contained structures that were unidentifiable, rendering them unsuitable for analysis. Therefore, it is essential to highlight that without the additional information given from 3D emission tomography obtaining a comprehensive understanding of fluorescence signal origin would have been considerably more challenging.

Figure 4.12 presents lifetime analysis of the fluorescence data depicted in Figure 4.10 (a). The obtained lifetimes, as illustrated in Figure 4.12 (b), demonstrates slightly shorter lifetimes at the outer edge compared to the centre region, whereas the general structure maintains a relatively uniform lifetime. Along the outer edge of the fluorescence, a weakening of the signal strength can be observed that results in a lower SNR and is responsible for the spike observed in the lifetime data.

The image depicted in Figure 4.12 (a) can now be quenching corrected using the corresponding lifetimes. This correction involves dividing image (a) by image (b) enabling a direct comparison of image intensities. The resulting image is presented in Figure 4.12 (c), and its overall shape closely resembles that of the original uncorrected image in Figure 4.12 (a). Examination of intensity along the selected line reveals that the left peak now displays a slightly modified shape with reduced intensity. This is a result from a minor increase in lifetime, indicative of reduced quenching, specifically on the left side of the hole.
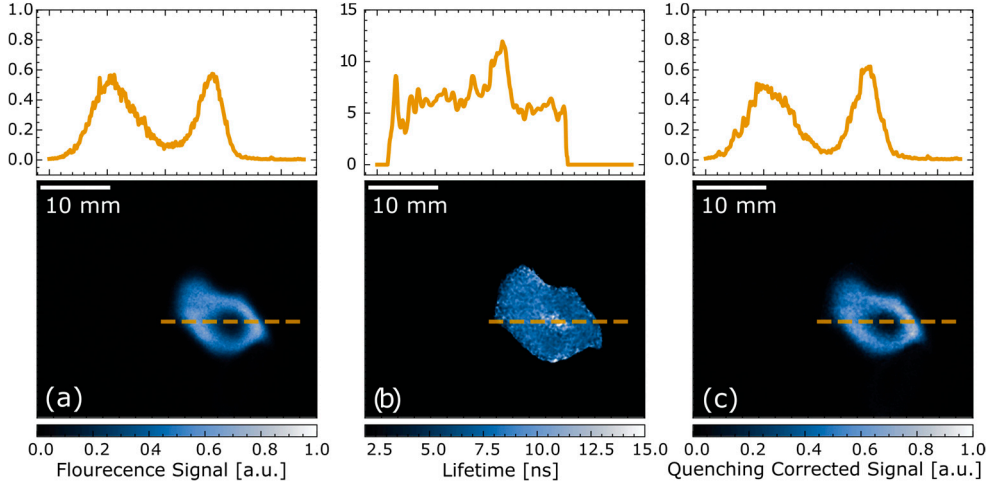
Figure 4.12: (a) Fluorescence image at 10 L/min, same as the one shown in Figure 4.10 (a). (b) Corresponding lifetime image obtained using DIME. (c) Resulting quenching corrected fluorescence image.

This work aims to enable quenching-corrected fluorescence imaging, thereby facilitating more quantitative measurements while through the integration of 3D emission tomography give a more comprehensive understanding of both the fluorescence structures and the intricate operational modes of gliding arcs and other plasma discharges.

4.3 Shadowgraphy

Shadowgraphy relies on detecting changes in the refractive index of a transparent medium, such as air or water. While sharing similarities with the schlieren technique, shadowgraphy offers a slightly simpler implementation, enhancing its practicality and applicability. These changes in refractive index can arise from various factors, including alterations in temperature, gas composition, or density. As light refracts through these index variations, distinct shadows are formed, enabling detailed investigations of diverse flow fields such as shockwaves and turbulent flows [137]. Figure 4.13 illustrates a shadowgraph setup used within work of this thesis, where a 450 nm diode laser is expanded onto a non-uniform white surface, causing the light to scatter through the probe volume. Subsequently, this scattered light serves as the primary light source for shadow creation.
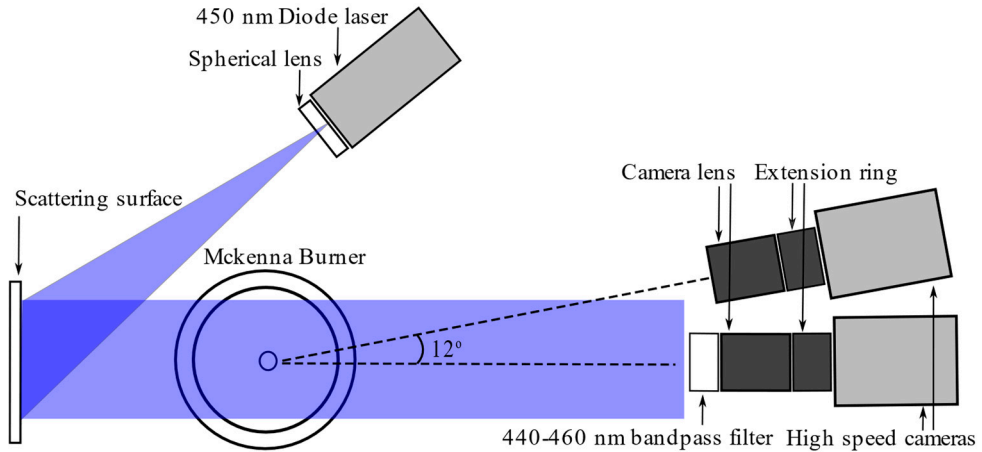
Figure 4.13: Schematic of experimental shadowgraphy setup studying a Mckenna Burner. Two high speed cameras are put in stereoscopic configuration, first camera looking at the shadows cast by the recracted diode laser, second camera looks at the natural luminosity image.

4.3.1   Nanoparticle-release in iron combustion

As previously discussed in section 3.3 describing Stereoscopic High-Speed Imaging of iron Microexplosions, metals have garnered significant attention as carbon-free energy carriers [90, 91]. A critical aspect to using iron or other metals as energy carriers is their potential for recyclability. This recycling process involves converting the resulting oxidized iron from combustion back into pure iron through electrolysis, powered by renewable sources like solar energy. However, the efficiency of this recycling process hinges on various factors, including the ability to capture the oxidized iron. The presence of nanoparticles in this context could complicate the capture process, potentially leading to diminished efficiency and raising health-related concerns.

In this study, high-speed shadowgraphy was employed to analyse the combustion dynamics of iron particles (d_{50} = 70 μm) introduced into a diffusive jet flame generated by a customized Mckenna flat-flame burner. The experimental arrangement for shadowgraphy is illustrated in Figure 4.13, featuring a stereoscopic configuration of two high-speed cameras. This setup enabled the simultaneous acquisition of both a shadow image and a thermal image from the same probed volume.

Results from this study included observations of release trails, possibly containing nanoparticles, emanating from burning iron particles, as seen in Figure 4.14 sequence (a), highlighted within the blue box. The emission from the particle is observed to progressively develop until it ultimately undergoes a microexplosion at 3 ms. The majority of these release trails were not observable in the simultaneously

acquired thermal images shown in sequence (b) of the same particle, which in turn showcasing the strength and usability of the shadowgraphy technique.
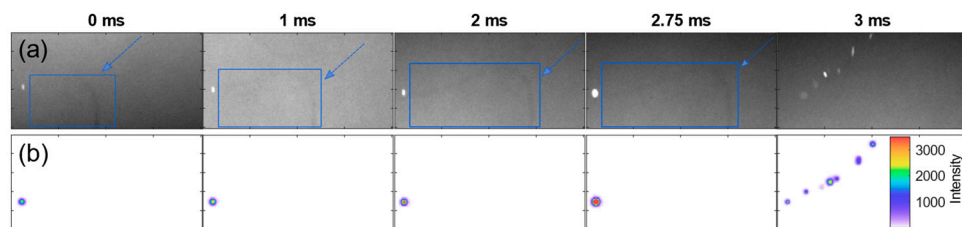

Figure 4.14: Sequence of shadowgraph images capturing particle release, followed by an explosion, over a duration of 3 milliseconds. The particle release is highlighted by the presence of blue boxes (a), while in parallel, a series of thermal radiation images of the same particle is shown (b).

The burning iron particle in Figure 4.14, can be seen to emit light in the sequence (a) which should be a shadow sequence. This occurs due to the particle being able to attain high temperatures, sometimes exceeding 2000K [94]. Consequently, the particle will emit light within the blue spectral range, aligning with the wavelength of the 450 nm diode laser. As a result, this emitted light, together with the laser light, will pass the 440-460 nm bandpass filter positioned in front of the camera, producing its visualization in the shadow image.
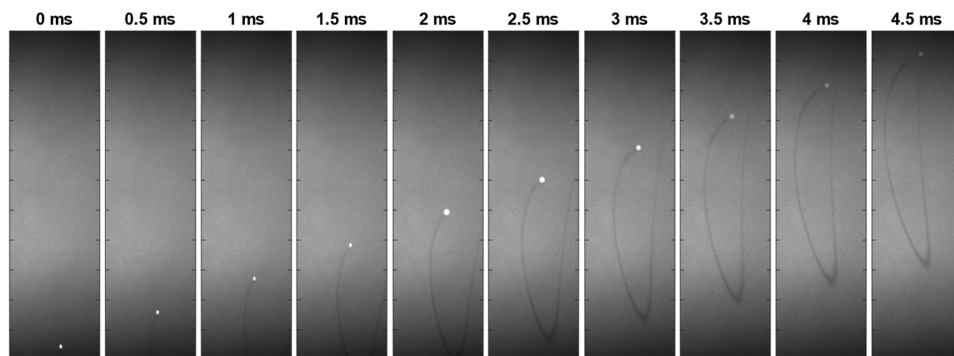
Figure 4.15: Sequential set of shadowgraph images depicting a burning iron particle and its accompanying release trail, spanning a duration of 4.5 milliseconds. The top and bottom of each image exhibit dark sections attributed to laser light limitations.

An additional sequence of shadowgraph images is presented in Figure 4.15, featuring a burning iron particle along with its release trail. Notably, these images reveal that the release trail exhibits considerable size in comparison to the originating particle and may result in large particle mass loss. The release process is seen to continue throughout the burning phase of the particle, and it is plausible

that this release trail is comprised of nanoparticles, the presence of which might pose significant challenges to the recyclability of the iron carrier and health precautions. For further insights into the potential nanoparticle-release and iron oxide products, refer to paper III.

4.4 Thermographic Phosphors

Thermographic phosphors are materials that exhibit temperature-dependent luminescence when excited by an external energy source, such as X-rays or UV light [138, 139]. Typically, a phosphor consists of a host crystal doped with either a lanthanide ion or a transition metal ion, which imparts its luminescence properties [139]. These phosphors can then be applied as a coating to surfaces, and their temperature-dependent characteristics can be utilized for surface thermometry [138].

Two frequently employed characteristics of phosphors are the spectral intensity change of their luminescence and the lifetime change of the luminescence decay. Nevertheless, the sensitivity of these characteristics also relies on the temperature range being measured, making certain phosphors more or less suitable for specific temperature ranges [140-142]. For instance, some phosphors exhibit heightened sensitivity at extremely high temperatures, such as 2000 K, while others may only be sensitive at cryogenic temperatures [143, 144] making appropriate phosphor selection vital for the specific application. Various detectors are commonly employed for capturing the generated phosphorescence luminosity, including PMT detectors, CMOS sensors, and CCD cameras.

Upon excitation of phosphors to a higher energy state through energy absorption from sources such as laser irradiation, two primary pathways of deexcitation emerge, namely radiative and non-radiative deexcitation. In radiative deexcitation, photons are emitted and can subsequently be measured, whereas in non-radiative deexcitation, no photons are generated, and the energy is dissipated through other processes like collisions. Consequently, the emission from an excited phosphor gradually decays over time, leading to a reduction in the measured phosphor luminescence. This reduction in luminescence behaviour is often approximated using a mono-exponential decay

$$I(t) = I_o \cdot e^{-\frac{t}{\tau}} \tag{26}$$

where I_o represents the initial intensity, $I(t)$ the emission intensity at time t, with a decay time of τ [139]. The decay time τ of phosphors is temperature-dependent, typically decreasing as the temperature rises, thereby enabling the extraction of temperature information from measured decay times [145]. Figure 4.16 illustrates the relationship between the measured decay time and increasing temperature,

highlighting the reduction in decay time as temperatures rise. Notably, the two displayed phosphors exhibit different sensitivity ranges: YVO$_4$:Tm demonstrates sensitivity below 650 K, while Mg$_4$FGeO$_6$:Mn shows sensitivity above 650 K.
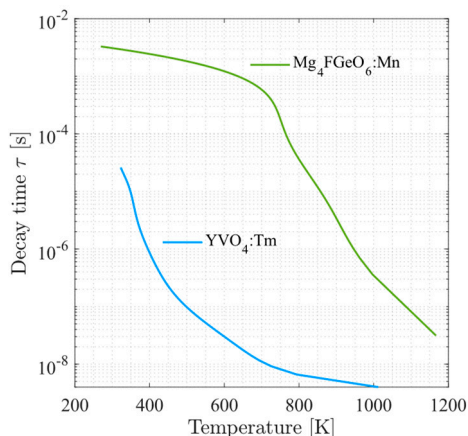
Figure 4.16: Measured decay time of the two phosphors YVO$_4$:Tm and Mg$_4$FGeO$_6$:Mn.

The flexibility and versatility of the technique stem from that it only requires optical access and a coating application of phosphor to the surface that is to be measured. However, the technique becomes semi-invasive due to the phosphor coating application. Nonetheless, the induced effect can be reduced with the use of thinner coatings and despite this semi-invasive aspect, the technique still exhibits the potential for achieving both high measurement precision and accuracy.

The phosphor thermometry work within this thesis focused on utilizing the luminescence lifetime dependence to determine surface temperatures. Pulsed laser irradiation served as the employed excitation source, and the collected phosphorescence signal was detected using PMT detectors.

4.4.1 PMT nonlinearities in phosphor thermometry

Photomultiplier tube-based acquisition systems are known for their high sensitivity and rapid rise and fall times. These characteristics make them commonly used as point detectors in conjunction with phosphor thermometry, particularly for examining decay times [142].

Earlier investigations have demonstrated that nonlinear photomultiplier tube effects can result in significant errors in measured decay time when there are variations in phosphorescence intensity. This becomes of particular concern for single-shot measurements, as the need for high SNR demands a strong phosphor luminescence signal, which can potentially lead to PMT nonlinearity effects changing the shape

of the decay curve. In the end, the goal is to avoid this and ensure that variations in the signal do not affect the measured decay time.

However, prior studies primarily focused on detection system effects under conditions of fixed or small changes in decay times. Additionally, these studies did not consistently disentangle the influences arising from changes in phosphorescence intensity, PMT gain, and laser fluence [146-150]. If change in phosphorescence intensity is caused by variations in excitation laser fluence, it will be unclear if the change of decay time is caused by detector effects or phosphorescence variations. Therefore, nonlinearity effects in detectors are ideally studied by phosphorescence signal attenuation with for example neutral density filters. Similar disentanglement needs to be done when investigating the relationship between laser fluence and the measured decay time.

In this investigation, the phosphorescence peak signal was varied using neutral density (ND) filters, and a range of phosphor decay times, from 3 ms down to 20 ns, was explored to evaluate nonlinearity effects in PMTs. The phosphors chosen for this study were YVO4:Tm and Mg_4FGeO_6:Mn, primarily due to their widespread usage in the field of phosphor thermometry. Additionally, these phosphors were selected for their decay times, which span multiple orders of magnitude, while still providing sufficient phosphorescence signal for this investigation.

Two primary PMT effects can introduce nonlinear detector response, namely photocathode bleaching and space charge accumulation at the end of the dynode chain. Photocathode bleaching arises when an excess of photons reaches the photocathode within a sufficiently short time interval and depletes the valence band resulting in a nonlinear intensity response in the PMT. Space charge accumulation is more likely to occur in the presence of high light fluence, high overall gain, and a lower voltage configuration across the last dynodes in the PMT [146]. Under such conditions, substantial local electric fields (space charges) can arise at the end of the dynode chain and the anode, leading to disturbances in incoming electrons creating nonlinear response [146, 151].

Figure 4.17 show the fractional decay time error, calculated by dividing all decay times within a series, such as 3×10^{-3} s, by the decay time of the data point with the lowest peak signal in the same series. The peak signal level for a decay curve refers to the maximum voltage measured during the signal. The data point with the lowest peak signal is selected as the reference point, as it can be assumed that it experiences the least detector nonlinearities due to its lowest phosphorescence intensity.
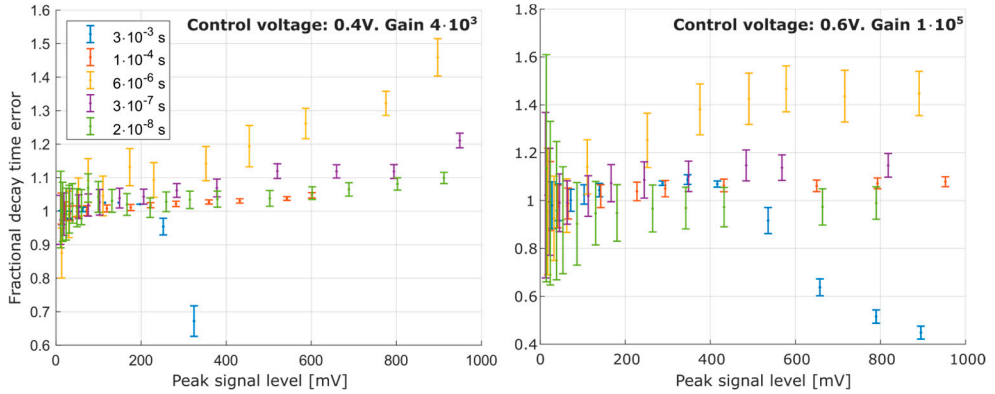
Figure 4.17: Relationship between decay time error and peak signals, employing a H11526-20-NF PMT and constant laser fluence. Peak signals was systematically varied using neutral density filters.

The investigation results are shown in Figure 4.17, illustrating decay times at different peak signal levels. The measured decay time decreases as the peak signal increases for decay times within the range of 3×10^{-3} s. This decay time decrease was probably due to the high average phosphor luminosity intensity caused by the long decay times that in turn caused photocathode bleaching [151] or dynode chain charge depletion [152] in the PMT. After such bleaching, it will take some time for the photocathode to recover and return to a linear response again.

Decay times of 10^{-4} s do not exhibit saturation effects. However, for faster decay times of approximately 6×10^{-6} s, an increase in the measured decay time becomes evident. This phenomenon is likely attributable to space charge accumulation at the anode and the last few dynodes, which disrupts the electron propagation, reduces the anode current, and extends the signal, resulting in a longer perceived decay time [151]. Shorter decay time in the range of than 6×10^{-6} s showed diminished effects due to nonlinearity. Higher noise at higher control voltages results from allowing only small fractions of the phosphorescence to reach the detector, preventing excessive anode currents that could potentially damage the PMT.

Superior precision at lower gains, resulting from a higher photon flux at corresponding peak signal levels, is appealing for single-shot temperature measurements. However, caution must be exercised concerning potential decay time accuracy issues due to nonlinearities. This investigation showed that generally the PMT exhibited improved linearity with an increase in gain for a given peak signal level and decay time. Increased gain resulted in decreased precision and therefore the selection of gain should be made based on needed precision and accuracy for the given application. To mitigate temperature errors caused by detector non-linearities, employing higher sensitivity phosphors proves effective, as they lead to a reduction in such inaccuracies.

4.4.2　Temperature measurements in a multi-fuel Stirling engine

In situ remote sensing of surface temperature measurements were conducted in combination with high-speed imaging of different combustion and ignition processes in a multi-fuel Stirling V4 underwater engine at Saab Kockums, showcased in Figure 4.18. The phosphor used was Mg_4FGeO_6:Mn selected due to its widespread usage in the phosphor thermometry field and its sensitivity within a large temperature range.
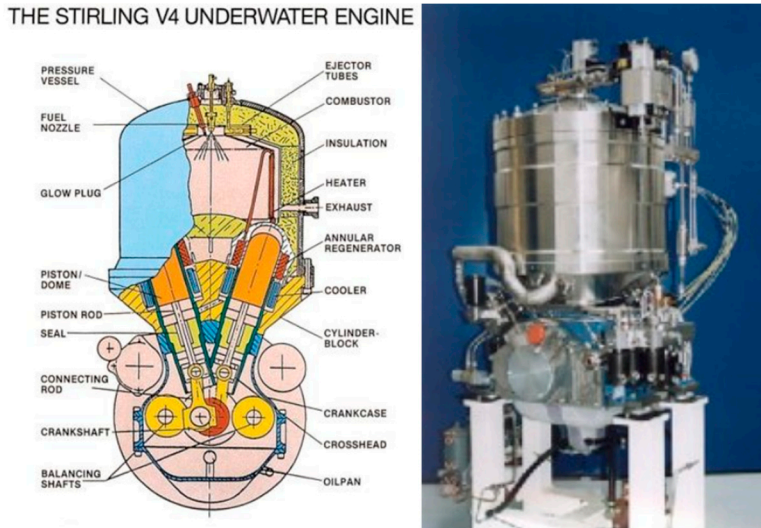
Figure 4.18: Illustration of the multi-fuel Stirling V4 underwater engine, curtesy of Saab Kockums.

Modifications were applied to the engine to facilitate optical access, and imaging inside the combustion chamber became possible with the use of a specially designed borescope adapter, as depicted in Figure 4.19. This adapter was both air- and water-cooled, enabling it to withstand the elevated temperatures within the chamber and in turn allowing for high-quality flame imaging using a high-speed camera. Moreover, this adapter played a crucial role in simplifying laser alignment within the pressure vessel during the phosphor thermometry measurements, which proved to be challenging due to restricted physical and optical access.

Figure 4.19: Custom-made air- and water-cooled borescope for optical access shown in left panels. Right panel shows the borescope coupled to a high-speed camera. Curtesy of Erik Pierrou, Saab Kockums.

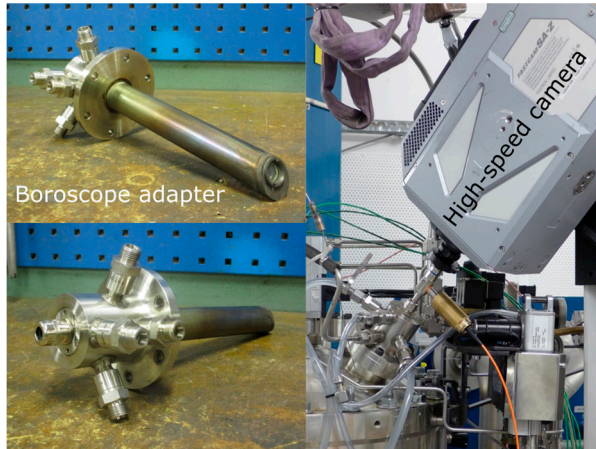In-situ high-speed measurements of combustion luminosity enabled investigations into flame topology, positioning, and ignition during different pressures and engine loads. Figure 4.20 displays an image sequence from a high-speed measurement capturing diesel and O2 combustion at 20 kHz, all images were acquired using 30 μs exposure time. The sequence showcases combustion at four different pressure levels (a-d), revealing significant variations in flame structure, which can be valuable for comparisons with Computational Fluid Dynamics (CFD) simulations.
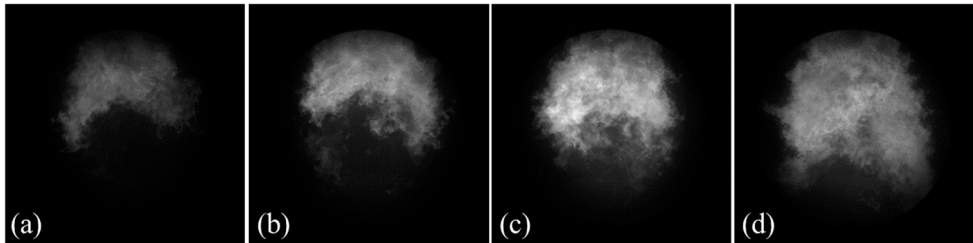
Figure 4.20: In-situ images of diesel and pure O_2 combustion at increasing pressures (a-d).

For the in-situ surface temperature measurements, a thin layer of phosphor was applied to adjacent heat-exchanger pipes, as illustrated in Figure 4.21 (c). This phosphor coating was later excited using 266 nm laser light from the fourth harmonic of a Nd:YAG laser, and temperature data were derived from the temperature-dependent phosphorescence lifetime, which was measured with a PMT. The study aimed to investigate surface temperatures at these specific heat exchanger pipes during diesel and O_2 combustion at various pressures and loads.

Optical access for the laser and detector system was facilitated by a side window integrated into the pressure vessel, as shown in Figure 4.21 (b). This window design allowed for laser illumination of the phosphor-coated heat exchanger within the vessel while simultaneously enabling the collection of the phosphorescence signal along the same optical path.
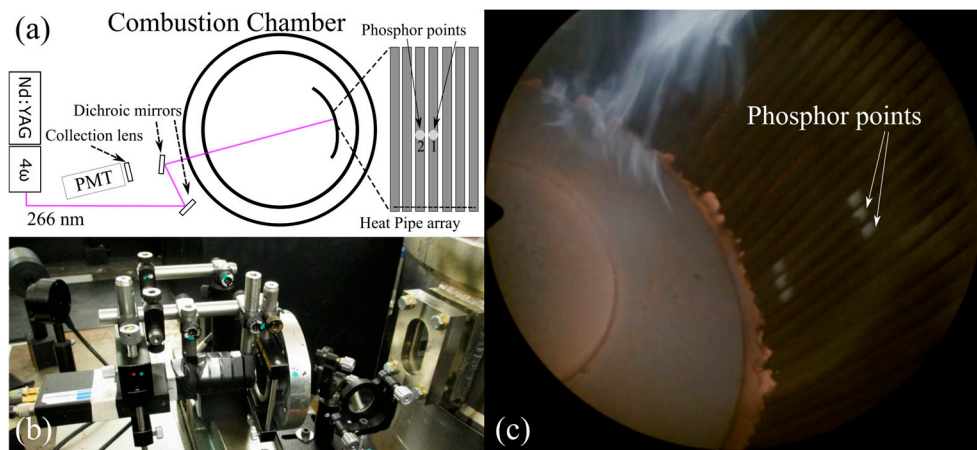
Figure 4.21: (a) Illustration of experimental setup. (b) Photo of experimental setup and optical window. (c) Image from inside combustion chamber during combustion, phosphor location is indicated by arrows. Images curtesy of Saab Kockums.

Additionally, similar temperature measurements were carried out during tests of H_2 and O_2 combustion scenarios. Summarized findings of relative temperature, where temperature measurements were averaged over all runs, are presented in Figure 4.22 for both diesel and hydrogen combustion cases.

These temperature measurements show a slight temperature difference between the two heat-exchanger pipes. This minor temperature difference is anticipated because one pipe (point 1) receives heat transfer air that has already passed through and cooled previous pipe (point 2). Consequently, the heat transfer from the pipe surface to the air is reduced, leading to a higher surface temperature in point 1. The capability to detect such variations in an in-situ environment, where both the excitation laser and the resulting signal traverse the combustion chamber and pass trough the flame within it, speaks to the precision of the phosphor thermometry technique.
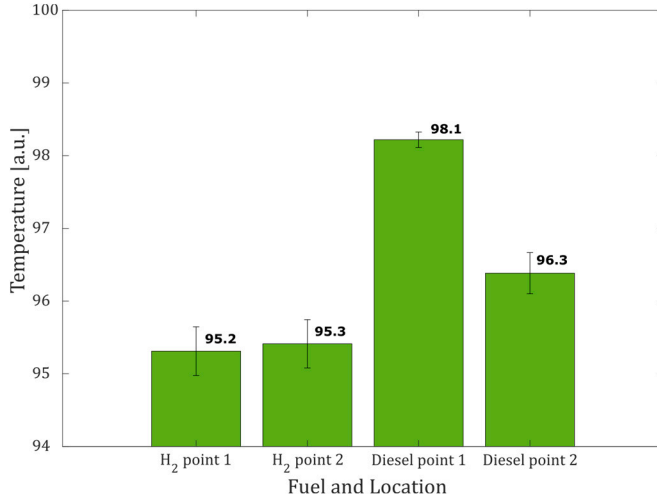
Figure 4.22: Normalized averaged surface temperatures on the heat-exchanger pipes 1 and 2 for both diesel and hydrogen combustion.

However, in the scenario of H_2 and O_2 combustion, no such significant difference could be observed. Figure 4.23 displays the relative surface temperatures across the tested runs for both hydrogen and diesel. Several factors could contribute to this observation, including the engine and many of its components not being fully optimized for H_2 combustion, as this was an initial test scenario. Additionally, the high diffusivity and rapid flame speed of hydrogen may lead to suboptimal heat distribution over the currently used heat exchanger and thus further investigations are needed to comprehensively evaluate these results.
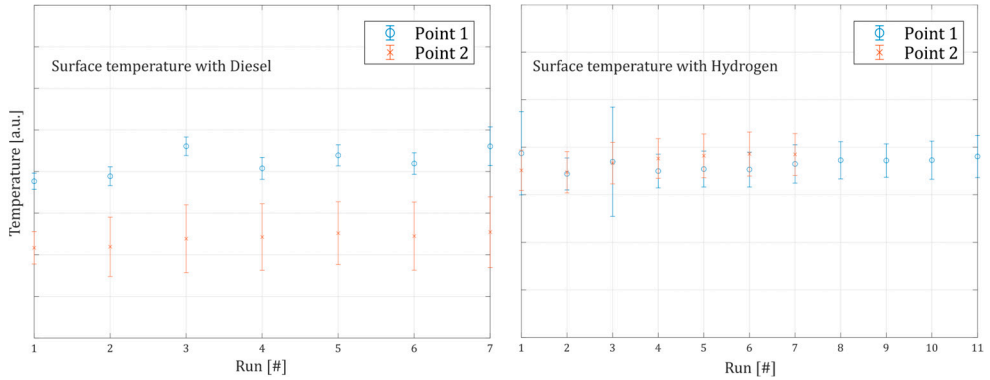
Figure 4.23: Relative surface temperatures for both heat pipes at different runs for both hydrogen and diesel.

5 Outlook

This thesis concerns development and application aspects of emission-based tomography and the application of laser-based techniques in reactive environments. The field of optical diagnostics offer numerous avenues for future research, although the suggestions outlined below are limited to the scope of this thesis.

Within emission tomography future research could focus on improving computational speed. While not the most vital characteristic of the technique, computational cost is still crucial, particularly when working with large volumes or conducting statistical and high-speed studies that involve extensive datasets. Furthermore, deeper investigation into the resolution and accuracy of the technique is warranted. While some previous work has touched on these aspects, the complexity of resolution in emission tomography necessitates a more comprehensive understanding.

On the practical application side, applying tomography to more complex reactive flows, such as plasma-assisted combustion, is intriguing. The ability of emission tomography to extract topology information could have substantial benefits in such processes. Similarly, exploring further integration of emission tomography with other optical diagnostics methods, such as volumetric LIF, in specialised flows holds promise. Improvement on such combined approaches could offer greater insights into complex systems.

For metal combustion studies, future research might employ more advanced techniques, such as improved particle tracking algorithms for better velocity measurements in higher density flows and micro-explosion studies. This field holds great promise, especially considering the potential for clean energy carriers.

The LIF and PIV studies conducted on the laboratory-scale swirl burner showed great promise. Given the importance of energy production, further research aimed at improving fuel efficiency and reducing emissions is vital. Future improvements on the experimental side could be studies using 3D PIV, possibly in combination with emission tomography.

More extensive evaluations are needed for the in-situ phosphor thermometry measurements performed in the multifuel sterling engine, particularly concerning the H_2 combustion. Given the increasing interest in H_2 as a clean fuel, this area

presents numerous research opportunities and the ability of phosphor thermometry to measure surface temperature in harsh environments can prove vital.

In conclusion, this thesis tries to lay a foundation and push for continued advancement in emission-based tomography and show applications of different non-intrusive laser-based techniques for studies in reactive environments to improve energy processes. The complex nature of these fields provides ample room for innovative research to address pressing challenges and contribute to various applications, including clean energy, combustion studies and plasma science. Furthermore, many of the techniques presented within this thesis such as emission tomography and LIF can be applied in fields outside of energy related research broadening the scope of research even further.

6 Acknowledgments

And so, we arrive at the place where most people stop and have a look around. So please "stay awhile and listen" as I try to thank all the people who helped me reach here. There are so many that I would like to acknowledge and give thanks to, but alas you may be too many… nevertheless I shall do my best…

I would like to start by thanking my main supervisor Mattias Richter for not only introducing me to this field but also for hiring me and being a great and supporting supervisor throughout my studies. I greatly appreciate the freedom you have given me to perform the work in my own way while still always being there for discussions and providing great suggestions and help.

I would also like to thank my co-supervisor Marcus Aldén for your honest feedback during my work, it was always greatly appreciated.

Then I want to thank all the people in my research group, both current and former. Henrik, thanks for great scientific collaborations and many fun discussions as well as that Warzone win, I still have goosebumps. Panagiota, I would like to thank you for always lifting the spirits in the group with your great mentality and supportive nature, it really helped. Ruike, thanks for our many discussions regarding optics and for introducing me to the world of motorsports, I never could imagine watching formula 1 could be so much fun. Alexios, I very much appreciated our scientific discussions, and I am still in awe of your deep car knowledge, you have taught me a lot. Saeed, thanks for all the interesting tech-talks and fun Swedish sessions, and we should not forget the skydiving excursion, that was crazy. Sebastian, thanks for many great collaborations and for just being such a great guy to be around, also thanks for introducing me to downhill mountain biking in Whistler, it was insane, and I loved it. Aravind, thanks for many discussions and for joining the ski trips, it was a blast. Kailun, thanks for many fun interactions on the lab floor, your tidiness as well as your snowboard skills always impresses me. Megha, thanks for the great collaboration and for always having such a positive mental attitude, also thanks for joining the epic ski trip.

I would also like to thank all the people working at the division, you have all together created a wonderful work environment that has been a pleasure to reside in during this time.

I would like to thank my officemate Vladimir for many scientific and non-scientific discussions, I consider you one of the smartest people I have ever met, and thanks for being the initiator for the skydiving trip, that was pure awesomeness. Adrian, thanks for all the great collaborations and fun activities we did together both in projects, within trivselgruppen, and outside of work, especially for introducing me to disc golf, a sport I most likely never will fully stop playing. Saga, thanks for all the interesting discussions and great climbing sessions, also thank you for initiating the via ferrata trip in Canada, that was one of the coolest things I have ever done. Yupan, Alsu and Lisa, thanks for some epic ski trips up north, I am however not sure I will ever take a snow bath again.

I would like to extend special thanks to Christian, Emelie, Minna, Cecilia, and Igor, for having helped me numerous times with various things over the years. I would also like to thank Arman, Vassily, Meena, David A, Sabrina, David F, Jonas, Zhiyong, Simon, Yue, Francesco, Shen, Meng, Armand, Anna-Lena, Jundie, Ali, Hampus, Martin, Per-Erik, Edouard, Andreas, Elias, Zhongshan, Joakim, Johan, Elna, Sven-Inge and many more, because you are all awesome.

Finally, I would like to thank my family for all the encouragement, love, and support you have given me. Mother and Father, thanks for always being there no matter what and for being such great role models. Ellinor, thanks for being the most awesome sister ever, our semi-yearly cycling and vacation trips are always insanely fun.

I have met so many great people along this road and so I will for sure have missed to mention someone as the hour is running late and this thesis needs to be printed, but for you who I might have missed I just want to say thank you!

7 References

[1] IEA, "Key World Energy Statistics 2021," IEA, https://www.iea.org/reports/key-world-energy-statistics-2021, 2021. [Online]. Available: https://www.iea.org/reports/key-world-energy-statistics-2021

[2] IEA, "World Energy Outlook 2022," IEA, https://www.iea.org/reports/world-energy-outlook-2022, 2022. [Online]. Available: https://www.iea.org/reports/world-energy-outlook-2022

[3] IEA, "Net Zero by 2050," IEA, https://www.iea.org/reports/net-zero-by-2050, 2021. [Online]. Available: https://www.iea.org/reports/net-zero-by-2050

[4] IEA, "Global Energy and Climate Model," IEA, https://www.iea.org/reports/global-energy-and-climate-model, 2022. [Online]. Available: https://www.iea.org/reports/global-energy-and-climate-model

[5] C. Liguori *et al.*, "Emerging clinical applications of computed tomography," *Medical Devices: Evidence and Research,* vol. 8, no. null, pp. 265-278, 2015/06/05 2015, doi: 10.2147/MDER.S70630.

[6] L. De Chiffre, S. Carmignato, J. P. Kruth, R. Schmitt, and A. Weckenmann, "Industrial applications of computed tomography," *CIRP Annals,* vol. 63, no. 2, pp. 655-677, 2014/01/01/ 2014, doi: https://doi.org/10.1016/j.cirp.2014.05.011.

[7] L.-Y. Chiao and B.-Y. Kuo, "Multiscale seismic tomography," *Geophysical Journal International,* vol. 145, no. 2, pp. 517-527, 2001, doi: 10.1046/j.0956-540x.2001.01403.x.

[8] S. J. Grauer, K. Mohri, T. Yu, H. Liu, and W. Cai, "Volumetric emission tomography for combustion processes," *Progress in Energy and Combustion Science,* vol. 94, p. 101024, 2023/01/01/ 2023, doi: https://doi.org/10.1016/j.pecs.2022.101024.

[9] Z. Wang, Y. Deguchi, T. Kamimoto, K. Tainaka, and K. Tanno, "Pulverized coal combustion application of laser-based temperature sensing system using computed tomography – Tunable diode laser absorption spectroscopy (CT-TDLAS)," *Fuel,* vol. 268, 2020, doi: 10.1016/j.fuel.2020.117370.

[10] C. Wei, D. I. Pineda, C. S. Goldenstein, and R. M. Spearrin, "Tomographic laser absorption imaging of combustion species and temperature in the mid-wave infrared," *Opt. Express,* vol. 26, no. 16, pp. 20944-20951, 2018/08/06 2018, doi: 10.1364/OE.26.020944.

[11] A. Schröder, R. Geisler, G. E. Elsinga, F. Scarano, and U. Dierksheide, "Investigation of a turbulent spot and a tripped turbulent boundary layer flow using time-resolved tomographic PIV," *Experiments in Fluids,* vol. 44, no. 2, pp. 305-316, 2007, doi: 10.1007/s00348-007-0403-2.

[12] S. J. Grauer, A. Unterberger, A. Rittler, K. J. Daun, A. M. Kempf, and K. Mohri, "Instantaneous 3D flame imaging by background-oriented schlieren tomography," *Combustion and Flame,* vol. 196, pp. 284-299, 2018/10/01/ 2018, doi: https://doi.org/10.1016/j.combustflame.2018.06.022.

[13] A. K. Agrawal, N. K. Butuk, S. R. Gollahalli, and D. Griffin, "Three-dimensional rainbow schlieren tomography of a temperature field in gas flows," *Appl. Opt.,* vol. 37, no. 3, pp. 479-485, 1998/01/20 1998, doi: 10.1364/AO.37.000479.

[14] B. R. Halls *et al.*, "kHz-rate four-dimensional fluorescence tomography using an ultraviolet-tunable narrowband burst-mode optical parametric oscillator," *Optica,* vol. 4, no. 8, pp. 897-902, 2017/08/20 2017, doi: 10.1364/OPTICA.4.000897.

[15] B. R. Halls, P. S. Hsu, S. Roy, T. R. Meyer, and J. R. Gord, "Two-color volumetric laser-induced fluorescence for 3D OH and temperature fields in turbulent reacting flows," *Opt Lett,* vol. 43, no. 12, pp. 2961-2964, Jun 15 2018, doi: 10.1364/OL.43.002961.

[16] L. Ma, Q. Lei, T. Capil, S. D. Hammack, and C. D. Carter, "Direct comparison of two-dimensional and three-dimensional laser-induced fluorescence measurements on highly turbulent flames," *Opt Lett,* vol. 42, no. 2, pp. 267-270, Jan 15 2017, doi: 10.1364/OL.42.000267.

[17] J. Floyd, P. Geipel, and A. M. Kempf, "Computed Tomography of Chemiluminescence (CTC): Instantaneous 3D measurements and Phantom studies of a turbulent opposed jet flame," *Combustion and Flame,* vol. 158, no. 2, pp. 376-391, 2011/02/01/ 2011, doi: https://doi.org/10.1016/j.combustflame.2010.09.006.

[18] D. A. Forsyth and J. Ponce, *Computer vision: a modern approach.* prentice hall professional technical reference, 2002.

[19] K. J. Daun, S. J. Grauer, and P. J. Hadwin, "Chemical species tomography of turbulent flows: Discrete ill-posed and rank deficient problems and the use of prior information," *Journal of Quantitative Spectroscopy and Radiative Transfer,* vol. 172, pp. 58-74, 2016/03/01/ 2016, doi: https://doi.org/10.1016/j.jqsrt.2015.09.011.

[20] Y. Yue and P. L. Speckman, "Nonstationary Spatial Gaussian Markov Random Fields," *Journal of Computational and Graphical Statistics,* vol. 19, no. 1, pp. 96-116, 2010/01/01 2010, doi: 10.1198/jcgs.2009.08124.

[21] G. Wahba, "Spline Interpolation and Smoothing on the Sphere," *SIAM Journal on Scientific and Statistical Computing,* vol. 2, no. 1, pp. 5-16, 1981/03/01 1981, doi: 10.1137/0902002.

[22] G. Wahba, *Spline Models for Observational Data* (CBMS-NSF Regional Conference Series in Applied Mathematics). Society for Industrial and Applied Mathematics, 1990, p. xvi + 161.

[23] G. Wahba, "A Comparison of GCV and GML for Choosing the Smoothing Parameter in the Generalized Spline Smoothing Problem," *The Annals of Statistics,* vol. 13, no. 4, pp. 1378-1402, 1985. [Online]. Available: http://www.jstor.org/stable/2241360.

[24] P. H. C. Eilers, I. D. Currie, and M. Durbán, "Fast and compact smoothing on large multidimensional grids," *Computational Statistics & Data Analysis,* vol. 50, no. 1, pp. 61-76, 2006/01/10/ 2006, doi: https://doi.org/10.1016/j.csda.2004.07.008.

[25] R. Barrett *et al.*, *Templates for the solution of linear systems: building blocks for iterative methods*. SIAM, 1994.

[26] D. W. Nychka, "Spatial-process estimates as smoothers," in *Smoothing and regression: approaches, computation, and application*: John Wiley & Sons, Inc., 2000, pp. 393-424.

[27] J. M. Tang and Y. Saad, "A probing method for computing the diagonal of a matrix inverse," *Numerical Linear Algebra with Applications,* https://doi.org/10.1002/nla.779 vol. 19, no. 3, pp. 485-501, 2012/05/01 2012, doi: https://doi.org/10.1002/nla.779.

[28] Y. Bao *et al.*, "Single-shot 3D imaging of hydroxyl radicals in the vicinity of a gliding arc discharge," *Plasma Sources Science and Technology,* vol. 30, no. 4, p. 04LT04, 2021/04/27 2021, doi: 10.1088/1361-6595/abda9c.

[29] C. Kong, J. Gao, J. Zhu, A. Ehn, M. Aldén, and Z. Li, "Characterization of an AC glow-type gliding arc discharge in atmospheric air with a current-voltage lumped model," *Physics of Plasmas,* vol. 24, no. 9, p. 093515, 2017, doi: 10.1063/1.4986296.

[30] H. M. Hertz and G. W. Faris, "Emission tomography of flame radicals," *Opt. Lett.,* vol. 13, no. 5, pp. 351-353, 1988/05/01 1988, doi: 10.1364/OL.13.000351.

[31] R. Bleekrode and W. C. Nieuwpoort, "Absorption and Emission Measurements of C2 and CH Electronic Bands in Low-Pressure Oxyacetylene Flames," *The Journal of Chemical Physics,* vol. 43, no. 10, pp. 3680-3687, 1965/11/15 1965, doi: 10.1063/1.1696536.

[32] J. Floyd and A. M. Kempf, "Computed Tomography of Chemiluminescence (CTC): High resolution and instantaneous 3-D measurements of a Matrix burner," *Proceedings of the Combustion Institute,* vol. 33, no. 1, pp. 751-758, 2011, doi: 10.1016/j.proci.2010.06.015.

[33] T. Yu, Z. Li, C. Ruan, F. Chen, X. Lu, and W. Cai, "Development of an absorption-corrected method for 3D computed tomography of chemiluminescence," *Measurement Science and Technology,* vol. 30, no. 4, p. 045403, 2019/03/18 2019, doi: 10.1088/1361-6501/ab01c1.

[34] R. Tsai, "A versatile camera calibration technique for high-accuracy 3D machine vision metrology using off-the-shelf TV cameras and lenses," *IEEE Journal on Robotics and Automation,* vol. 3, no. 4, pp. 323-344, 1987, doi: 10.1109/JRA.1987.1087109.

[35] R. Hartley and A. Zisserman, *Multiple View Geometry in Computer Vision*. Cambridge University Press, 2003.

[36] D. C. Brown, "Close-Range Camera Calibration," *PHOTOGRAMMETRIC ENGINEERING,* vol. 37, pp. 855–866, 1971.

[37] B. Li, L. Heng, K. Koser, and M. Pollefeys, "A multiple-camera system calibration toolbox using a feature descriptor-based calibration pattern," in *2013 IEEE/RSJ International Conference on Intelligent Robots and Systems*, 3-7 Nov. 2013 2013, pp. 1301-1307, doi: 10.1109/IROS.2013.6696517.

[38] G. Bradski and A. Kaehler, *Learning OpenCV: Computer vision with the OpenCV library*. " O'Reilly Media, Inc.", 2008.

[39] T. Svoboda, D. Martinec, and T. Pajdla, "A Convenient Multi-Camera Self-Calibration for Virtual Environments," *Presence,* vol. 14, pp. 407-422, 08/01 2005, doi: 10.1162/105474605774785325.

[40] A. Unterberger, J. Menser, A. Kempf, and K. Mohri, "Evolutionary Camera Pose Estimation of a Multi-Camera Setup for Computed Tomography," in *2019 IEEE International Conference on Image Processing (ICIP)*, 22-25 Sept. 2019 2019, pp. 464-468, doi: 10.1109/ICIP.2019.8804398.

[41] N. Machicoane, A. Aliseda, R. Volk, and M. Bourgoin, "A simplified and versatile calibration method for multi-camera optical systems in 3D particle imaging," *Review of Scientific Instruments,* vol. 90, no. 3, p. 035112, 2019, doi: 10.1063/1.5080743.

[42] A. Roth, S. Mehdi, D. Frantz, and E. Berrocal, "Stereoscopic high-speed imaging for 3D tracking of coughed saliva droplets in the context of COVID-19 spreading," in *Proceedings of the 20th International Symposium on Application of Laser and Imaging Techniques to Fluid Mechanics 2022*, 2022.

[43] G. E. Elsinga, F. Scarano, B. Wieneke, and B. W. van Oudheusden, "Tomographic particle image velocimetry," *Experiments in Fluids,* vol. 41, no. 6, pp. 933-947, 2006/12/01 2006, doi: 10.1007/s00348-006-0212-z.

[44] B. Wieneke, "Improvements for volume self-calibration," *Measurement Science and Technology,* vol. 29, no. 8, p. 084002, 2018/07/12 2018, doi: 10.1088/1361-6501/aacd45.

[45] B. O. Community. Blender - a 3D modelling and rendering package [Online] Available: http://www.blender.org

[46] J. Floyd, "Computed tomography of chemiluminescence: a 3D time resolved sensor for turbulent combustion," 2009.

[47] W. Cai, X. Li, F. Li, and L. Ma, "Numerical and experimental validation of a three-dimensional combustion diagnostic based on tomographic chemiluminescence," *Opt. Express,* vol. 21, no. 6, pp. 7050-7064, 2013/03/25 2013, doi: 10.1364/OE.21.007050.

[48] W. Cai, X. Li, and L. Ma, "Practical aspects of implementing three-dimensional tomography inversion for volumetric flame imaging," *Appl. Opt.,* vol. 52, no. 33, pp. 8106-8116, 2013/11/20 2013, doi: 10.1364/AO.52.008106.

[49] D. Schanz, S. Gesemann, A. Schröder, B. Wieneke, and M. Novara, "Non-uniform optical transfer functions in particle imaging: calibration and application to tomographic reconstruction," *Measurement Science and Technology,* vol. 24, no. 2, p. 024009, 2012/12/20 2013, doi: 10.1088/0957-0233/24/2/024009.

[50] F. Champagnat, P. Cornic, A. Cheminet, B. Leclaire, G. L. Besnerais, and A. Plyer, "Tomographic PIV: particles versus blobs," *Measurement Science and Technology,* vol. 25, no. 8, p. 084002, 2014/07/14 2014, doi: 10.1088/0957-0233/25/8/084002.

[51] H. Liu, T. Yu, M. Zhang, and W. Cai, "Demonstration of 3D computed tomography of chemiluminescence with a restricted field of view," *Appl Opt,* vol. 56, no. 25, pp. 7107-7115, Sep 1 2017, doi: 10.1364/AO.56.007107.

[52] T. Yu, H. Liu, and W. Cai, "On the quantification of spatial resolution for three-dimensional computed tomography of chemiluminescence," *Opt Express,* vol. 25, no. 20, pp. 24093-24108, Oct 2 2017, doi: 10.1364/OE.25.024093.

[53] K. Mohri *et al.*, "Instantaneous 3D imaging of highly turbulent flames using computed tomography of chemiluminescence," *Appl Opt,* vol. 56, no. 26, pp. 7385-7395, Sep 10 2017, doi: 10.1364/AO.56.007385.

[54] K. T. Walsh, J. Fielding, and M. B. Long, "Effect of light-collection geometry on reconstruction errors in Abel inversions," *Opt. Lett.,* vol. 25, no. 7, pp. 457-459, 2000/04/01 2000, doi: 10.1364/OL.25.000457.

[55] K. N. Kutulakos and S. M. Seitz, "A Theory of Shape by Space Carving," *International Journal of Computer Vision,* vol. 38, no. 3, pp. 199-218, 2000/07/01 2000, doi: 10.1023/A:1008191222954.

[56] A. W. Fitzgibbon, G. Cross, and A. Zisserman, "Automatic 3D Model Construction for Turn-Table Sequences," in *3D Structure from Multiple Images of Large-Scale Environments*, Berlin, Heidelberg, R. Koch and L. Van Gool, Eds., 1998// 1998: Springer Berlin Heidelberg, pp. 155-170.

[57] Y. Fu and Y. Liu, "3D bubble reconstruction using multiple cameras and space carving method," *Measurement Science and Technology,* vol. 29, no. 7, p. 075206, 2018/06/08 2018, doi: 10.1088/1361-6501/aac4aa.

[58] R. Gordon, R. Bender, and G. T. Herman, "Algebraic Reconstruction Techniques (ART) for three-dimensional electron microscopy and X-ray photography," *Journal of Theoretical Biology,* vol. 29, no. 3, pp. 471-481, 1970/12/01/ 1970, doi: https://doi.org/10.1016/0022-5193(70)90109-8.

[59] H. H. B. Sørensen and P. C. Hansen, "Multicore Performance of Block Algebraic Iterative Reconstruction Methods," *SIAM Journal on Scientific Computing,* vol. 36, no. 5, pp. C524-C546, 2014/01/01 2014, doi: 10.1137/130920642.

[60] E. O. Åkesson and K. J. Daun, "Parameter selection methods for axisymmetric flame tomography through Tikhonov regularization," *Appl. Opt.,* vol. 47, no. 3, pp. 407-416, 2008/01/20 2008, doi: 10.1364/AO.47.000407.

[61] M. M. Hossain, G. Lu, D. Sun, and Y. Yan, "Three-dimensional reconstruction of flame temperature and emissivity distribution using optical tomographic and two-colour pyrometric techniques," *Measurement Science and Technology,* vol. 24, no. 7, p. 074010, 2013/06/12 2013, doi: 10.1088/0957-0233/24/7/074010.

[62] T. R. Meyer, B. R. Halls, N. Jiang, M. N. Slipchenko, S. Roy, and J. R. Gord, "High-speed, three-dimensional tomographic laser-induced incandescence imaging of soot volume fraction in turbulent flames," *Opt Express,* vol. 24, no. 26, pp. 29547-29555, Dec 26 2016, doi: 10.1364/OE.24.029547.

[63] S. M. Wiseman, M. J. Brear, R. L. Gordon, and I. Marusic, "Measurements from flame chemiluminescence tomography of forced laminar premixed propane flames," *Combustion and Flame,* vol. 183, pp. 1-14, 2017/09/01/ 2017, doi: https://doi.org/10.1016/j.combustflame.2017.05.003.

[64] J. Gregson, M. Krimerman, M. B. Hullin, and W. Heidrich, "Stochastic tomography and its applications in 3D imaging of mixing fluids," *ACM Trans. Graph.,* vol. 31, no. 4, p. Article 52, 2012, doi: 10.1145/2185520.2185548.

[65] J. Huang, H. Liu, Q. Wang, and W. Cai, "Limited-projection volumetric tomography for time-resolved turbulent combustion diagnostics via deep learning," *Aerospace Science and Technology,* vol. 106, p. 106123, 2020/11/01/ 2020, doi: https://doi.org/10.1016/j.ast.2020.106123.

[66] Q. Wang, T. Yu, H. Liu, J. Huang, and W. Cai, "Optimization of camera arrangement for volumetric tomography with constrained optical access," *J. Opt. Soc. Am. B,* vol. 37, no. 4, pp. 1231-1239, 2020/04/01 2020, doi: 10.1364/JOSAB.385291.

[67] T. D. Fansler and S. E. Parrish, "Spray measurement technology: a review," *Measurement Science and Technology,* vol. 26, no. 1, p. 012002, 2014/12/01 2014, doi: 10.1088/0957-0233/26/1/012002.

[68] C. Schulz and V. Sick, "Tracer-LIF diagnostics: quantitative measurement of fuel concentration, temperature and fuel/air ratio in practical combustion systems," *Progress in Energy and Combustion Science,* vol. 31, no. 1, pp. 75-121, 2005/01/01/ 2005, doi: https://doi.org/10.1016/j.pecs.2004.08.002.

[69] C. D. Slabaugh, A. C. Pratt, and R. P. Lucht, "Simultaneous 5 kHz OH-PLIF/PIV for the study of turbulent combustion at engine conditions," *Applied Physics B,* vol. 118, no. 1, pp. 109-130, 2015/01/01 2015, doi: 10.1007/s00340-014-5960-5.

[70] B. R. Halls, D. J. Thul, D. Michaelis, S. Roy, T. R. Meyer, and J. R. Gord, "Single-shot, volumetrically illuminated, three-dimensional, tomographic laser-induced-fluorescence imaging in a gaseous free jet," *Opt. Express,* vol. 24, no. 9, pp. 10040-10049, 2016/05/02 2016, doi: 10.1364/OE.24.010040.

[71] S. J. Grauer, P. J. Hadwin, and K. J. Daun, "Bayesian approach to the design of chemical species tomography experiments," *Appl. Opt.,* vol. 55, no. 21, pp. 5772-5782, 2016/07/20 2016, doi: 10.1364/AO.55.005772.

[72] W. Zhou, A. C. Bovik, H. R. Sheikh, and E. P. Simoncelli, "Image quality assessment: from error visibility to structural similarity," *IEEE Transactions on Image Processing,* vol. 13, no. 4, pp. 600-612, 2004, doi: 10.1109/TIP.2003.819861.

[73] Y. Kusano, "Atmospheric Pressure Plasma Processing for Polymer Adhesion: A Review," *The Journal of Adhesion,* vol. 90, no. 9, pp. 755-777, 2014/09/02 2014, doi: 10.1080/00218464.2013.804407.

[74] Y. Kusano *et al.*, "Gliding arc surface treatment of glass-fiber-reinforced polyester enhanced by ultrasonic irradiation," *Surface and Coatings Technology,* vol. 205, pp. S490-S494, 2011/07/25/ 2011, doi: https://doi.org/10.1016/j.surfcoat.2011.01.061.

[75] T. Ombrello, Y. Ju, and A. Fridman, "Kinetic Ignition Enhancement of Diffusion Flames by Nonequilibrium Magnetic Gliding Arc Plasma," *AIAA Journal,* vol. 46, no. 10, pp. 2424-2433, 2008/10/01 2008, doi: 10.2514/1.33005.

[76] B. Lin, Y. Wu, Z. Zhang, D. Bian, and D. Jin, "Ignition enhancement of lean propane/air mixture by multi-channel discharge plasma under low pressure," *Applied Thermal Engineering,* vol. 148, pp. 1171-1182, 2019/02/05/ 2019, doi: https://doi.org/10.1016/j.applthermaleng.2018.12.011.

[77] D. H. Lee, K. T. Kim, M. S. Cha, and Y. H. Song, "Optimization scheme of a rotating gliding arc reactor for partial oxidation of methane," *Proceedings of the Combustion Institute,* vol. 31, no. 2, pp. 3343-3351, 2007/01/01/ 2007, doi: https://doi.org/10.1016/j.proci.2006.07.230.

[78] S. Starikovskaia, D. A. Lacoste, and G. Colonna, "Non-equilibrium plasma for ignition and combustion enhancement," *The European Physical Journal D,* vol. 75, no. 8, p. 231, 2021/08/24 2021, doi: 10.1140/epjd/s10053-021-00240-2.

[79] J. Gao, J. Zhu, A. Ehn, M. Aldén, and Z. Li, "In-Situ Non-intrusive Diagnostics of Toluene Removal by a Gliding Arc Discharge Using Planar Laser-Induced Fluorescence," *Plasma Chemistry and Plasma Processing,* vol. 37, no. 2, pp. 433-450, 2017/03/01 2017, doi: 10.1007/s11090-016-9771-9.

[80] A. Fridman, S. Nester, L. A. Kennedy, A. Saveliev, and O. Mutaf-Yardimci, "Gliding arc gas discharge," *Progress in Energy and Combustion Science,* vol. 25, no. 2, pp. 211-231, 1999/04/01/ 1999, doi: https://doi.org/10.1016/S0360-1285(98)00021-5.

[81] Z. W. Sun *et al.*, "Optical diagnostics of a gliding arc," *Opt. Express,* vol. 21, no. 5, pp. 6028-6044, 2013/03/11 2013, doi: 10.1364/OE.21.006028.

[82] C. Kong, J. Gao, J. Zhu, A. Ehn, M. Aldén, and Z. Li, "Effect of turbulent flow on an atmospheric-pressure AC powered gliding arc discharge," *Journal of Applied Physics,* vol. 123, no. 22, p. 223302, 2018, doi: 10.1063/1.5026703.

[83] A. Ehn, J. Bood, Z. Li, E. Berrocal, M. Aldén, and E. Kristensson, "FRAME: femtosecond videography for atomic and molecular dynamics," *Light: Science & Applications,* vol. 6, no. 9, pp. e17045-e17045, 2017/09/01 2017, doi: 10.1038/lsa.2017.45.

[84] J. Zhu *et al.*, "Measurements of 3D slip velocities and plasma column lengths of a gliding arc discharge," *Applied Physics Letters,* vol. 106, no. 4, p. 044101, 2015, doi: 10.1063/1.4906928.

[85] S. Pellerin, J. M. Cormier, F. Richard, K. Musiol, and J. Chapelle, "Determination of the electrical parameters of a bi-dimensional d.c. Glidarc," *Journal of Physics D: Applied Physics,* vol. 32, no. 8, p. 891, 1999/04/21 1999, doi: 10.1088/0022-3727/32/8/009.

[86] J. Ananthanarasimhan, P. Leelesh, M. S. Anand, and R. Lakshminarayana, "Validation of projected length of the rotating gliding arc plasma using 'regionprops' function," *Plasma Research Express,* vol. 2, no. 3, p. 035008, 2020/08/18 2020, doi: 10.1088/2516-1067/abae49.

[87] M. McNall and S. Coulombe, "Characterization of a rotating gliding arc in argon at atmospheric pressure," *Journal of Physics D: Applied Physics,* vol. 51, no. 44, p. 445203, 2018/09/28 2018, doi: 10.1088/1361-6463/aade44.

[88] J. Zhu *et al.*, "Dynamics, OH distributions and UV emission of a gliding arc at various flow-rates investigated by optical measurements," *Journal of Physics D: Applied Physics,* vol. 47, no. 29, p. 295203, 2014/06/26 2014, doi: 10.1088/0022-3727/47/29/295203.

[89] J. Zhu *et al.*, "Translational, rotational, vibrational and electron temperatures of a gliding arc discharge," *Opt. Express,* vol. 25, no. 17, pp. 20243-20257, 2017/08/21 2017, doi: 10.1364/OE.25.020243.

[90] A. Davis, "Solid propellants: The combustion of particles of metal ingredients," *Combustion and Flame,* vol. 7, pp. 359-367, 1963/01/01/ 1963, doi: https://doi.org/10.1016/0010-2180(63)90212-8.
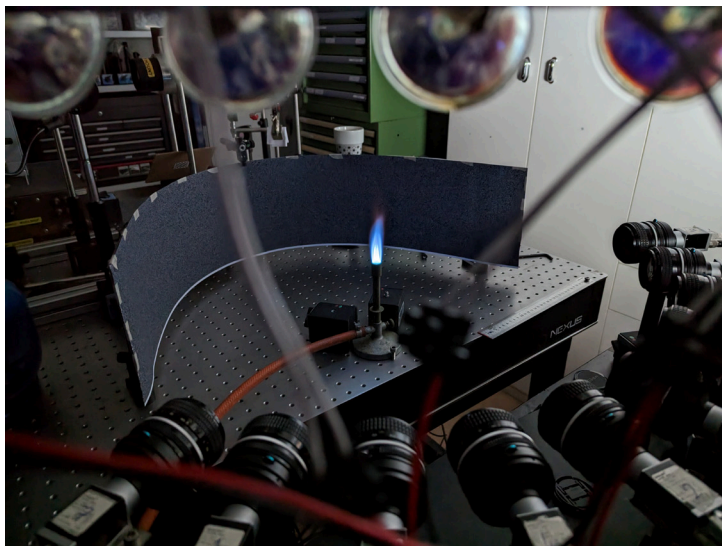
[91] J. M. Bergthorson, "Recyclable metal fuels for clean and compact zero-carbon power," *Progress in Energy and Combustion Science,* vol. 68, pp. 169-196, 2018/09/01/ 2018, doi: https://doi.org/10.1016/j.pecs.2018.05.001.

[92] J. M. Bergthorson *et al.*, "Metal-water combustion for clean propulsion and power generation," *Applied Energy,* vol. 186, pp. 13-27, 2017/01/15/ 2017, doi: https://doi.org/10.1016/j.apenergy.2016.10.033.

[93] R. A. Yetter, G. A. Risha, and S. F. Son, "Metal particle combustion and nanotechnology," *Proceedings of the Combustion Institute,* vol. 32, no. 2, pp. 1819-1838, 2009/01/01/ 2009, doi: https://doi.org/10.1016/j.proci.2008.08.013.

[94] N. I. Poletaev and M. Y. Khlebnikova, "Combustion of Iron Particles Suspension in Laminar Premixed and Diffusion Flames," *Combustion Science and Technology,* vol. 194, no. 7, pp. 1356-1377, 2022/05/19 2022, doi: 10.1080/00102202.2020.1812588.

[95] A. Wright, S. Goroshin, and A. Higgins, "Combustion time and ignition temperature of iron particles in different oxidizing environments," 2015.

[96] M. Bourgoin and S. G. Huisman, "Using ray-traversal for 3D particle matching in the context of particle tracking velocimetry in fluid mechanics," *Review of Scientific Instruments,* vol. 91, no. 8, p. 085105, 2020, doi: 10.1063/5.0009357.

[97] P. Tóth, Y. Ögren, A. Sepman, P. Gren, and H. Wiinikka, "Combustion behavior of pulverized sponge iron as a recyclable electrofuel," *Powder Technology,* vol. 373, pp. 210-219, 2020/08/01/ 2020, doi: https://doi.org/10.1016/j.powtec.2020.05.078.

[98] B. Schwarzchild, "Drops of liquid exhibit surprising self-propulsion on ratcheted surfaces," *Physics Today,* vol. 59, no. 6, pp. 17-19, 2006, doi: 10.1063/1.2218536.

[99] Y. Feng, L. Ma, Z. Xia, L. Huang, and D. Yang, "Ignition and combustion characteristics of single gas-atomized Al–Mg alloy particles in oxidizing gas flow," *Energy,* vol. 196, p. 117036, 2020/04/01/ 2020, doi: https://doi.org/10.1016/j.energy.2020.117036.

[100] M. Raffel, C. E. Willert, F. Scarano, C. J. Kähler, S. T. Wereley, and J. Kompenhans, *Particle image velocimetry: a practical guide*. Springer, 2018.

[101] A. C. Eckbreth, *Laser diagnostics for combustion temperature and species*. CRC press, 2022.

[102] R. J. Adrian and J. Westerweel, *Particle image velocimetry* (no. 30). Cambridge university press, 2011.

[103] R. Theunissen, F. Scarano, and M. L. Riethmuller, "An adaptive sampling and windowing interrogation method in PIV," *Measurement Science and Technology,* vol. 18, no. 1, p. 275, 2006/12/14 2007, doi: 10.1088/0957-0233/18/1/034.

[104] J. H. Seong, M. S. Song, D. Nunez, A. Manera, and E. S. Kim, "Velocity refinement of PIV using global optical flow," *Experiments in Fluids,* vol. 60, no. 11, p. 174, 2019/10/29 2019, doi: 10.1007/s00348-019-2820-4.

[105] B. E. Schmidt, A. W. Skiba, S. D. Hammack, C. D. Carter, and J. A. Sutton, "High-resolution velocity measurements in turbulent premixed flames using wavelet-based optical flow velocimetry (wOFV)," *Proceedings of the Combustion Institute,* vol. 38, no. 1, pp. 1607-1615, 2021/01/01/ 2021, doi: https://doi.org/10.1016/j.proci.2020.07.028.

[106] T. Liu, A. Merat, M. H. M. Makhmalbaf, C. Fajardo, and P. Merati, "Comparison between optical flow and cross-correlation methods for extraction of velocity fields from particle images," *Experiments in Fluids,* vol. 56, no. 8, p. 166, 2015/08/06 2015, doi: 10.1007/s00348-015-2036-1.

[107] B. Atcheson, W. Heidrich, and I. Ihrke, "An evaluation of optical flow algorithms for background oriented schlieren imaging," *Experiments in Fluids,* vol. 46, no. 3, pp. 467-476, 2009/03/01 2009, doi: 10.1007/s00348-008-0572-7.

[108] R. Miles, "Femtosecond Laser Electronic Excitation Tagging (FLEET) for Imaging Flow Structure in Unseeded Hot or Cold Air or Nitrogen," in *51st AIAA Aerospace Sciences Meeting including the New Horizons Forum and Aerospace Exposition*, (Aerospace Sciences Meetings: American Institute of Aeronautics and Astronautics, 2013.

[109] N. J. DeLuca, R. B. Miles, W. D. Kulatilaka, N. Jiang, and J. R. Gord, "Femtosecond Laser Electronic Excitation Tagging (FLEET) Fundamental Pulse Energy and Spectral Response," in *30th AIAA Aerodynamic Measurement Technology and Ground Testing Conference*, (AIAA AVIATION Forum: American Institute of Aeronautics and Astronautics, 2014.

[110] N. A. Samiran, J.-H. Ng, M. N. Mohd Jaafar, A. Valera-Medina, and C. T. Chong, "H2-rich syngas strategy to reduce NOx and CO emissions and improve stability limits under premixed swirl combustion mode," *International Journal of Hydrogen Energy,* vol. 41, no. 42, pp. 19243-19255, 2016/11/09/ 2016, doi: https://doi.org/10.1016/j.ijhydene.2016.08.095.

[111] N. A. Samiran, M. N. M. Jaafar, J.-H. Ng, S. S. Lam, and C. T. Chong, "Progress in biomass gasification technique – With focus on Malaysian palm biomass for syngas production," *Renewable and Sustainable Energy Reviews,* vol. 62, pp. 1047-1062, 2016/09/01/ 2016, doi: https://doi.org/10.1016/j.rser.2016.04.049.

[112] A. N. Lipatnikov and J. Chomiak, "Molecular transport effects on turbulent flame propagation and structure," *Progress in Energy and Combustion Science,* vol. 31, no. 1, pp. 1-73, 2005/01/01/ 2005, doi: https://doi.org/10.1016/j.pecs.2004.07.001.

[113] R. Engeln, B. Klarenaar, and O. Guaitella, "Foundations of optical diagnostics in low-temperature plasmas," *Plasma Sources Science and Technology,* vol. 29, no. 6, p. 063001, 2020/06/15 2020, doi: 10.1088/1361-6595/ab6880.

[114] M. Kwaśny and A. Bombalska, "Applications of Laser-Induced Fluorescence in Medicine," *Sensors*, vol. 22, no. 8, doi: 10.3390/s22082956.

[115] A. Johchi, J. Pareja, B. Böhm, and A. Dreizler, "Quantitative mixture fraction imaging of a synthetic biogas turbulent jet propagating into a NO-vitiated air co-flow using planar laser-induced fluorescence (PLIF)," *Experiments in Fluids,* vol. 60, no. 5, p. 82, 2019/04/17 2019, doi: 10.1007/s00348-019-2723-4.

[116] V. B. Mbayachi, Z.-Y. Tian, X. Zhang, M. Khalil, and D. A. Ayejoto, "Laser-Induced Fluorescence in Combustion Research," in *Advanced Diagnostics in Combustion Science*, Z.-Y. Tian Ed. Singapore: Springer Nature Singapore, 2023, pp. 223-243.

[117] R. Wellander, M. Richter, and M. Aldén, "Time-resolved (kHz) 3D imaging of OH PLIF in a flame," *Experiments in Fluids,* vol. 55, no. 6, p. 1764, 2014/06/14 2014, doi: 10.1007/s00348-014-1764-y.

[118] B. R. Halls, N. Jiang, T. R. Meyer, S. Roy, M. N. Slipchenko, and J. R. Gord, "4D spatiotemporal evolution of combustion intermediates in turbulent flames using burst-mode volumetric laser-induced fluorescence," *Opt. Lett.,* vol. 42, no. 14, pp. 2830-2833, 2017/07/15 2017, doi: 10.1364/OL.42.002830.

[119] L. Ma, Q. Lei, J. Ikeda, W. Xu, Y. Wu, and C. D. Carter, "Single-shot 3D flame diagnostic based on volumetric laser induced fluorescence (VLIF)," *Proceedings of the Combustion Institute,* vol. 36, no. 3, pp. 4575-4583, 2017/01/01/ 2017, doi: https://doi.org/10.1016/j.proci.2016.07.050.

[120] Y. Li *et al.*, "Single-shot time-gated fluorescence lifetime imaging using three-frame images," *Opt. Express,* vol. 26, no. 14, pp. 17936-17947, 2018/07/09 2018, doi: 10.1364/OE.26.017936.

[121] A. Ehn, O. Johansson, A. Arvidsson, M. Aldén, and J. Bood, "Single-laser shot fluorescence lifetime imaging on the nanosecond timescale using a Dual Image and Modeling Evaluation algorithm," *Opt. Express,* vol. 20, no. 3, pp. 3043-3056, 2012/01/30 2012, doi: 10.1364/OE.20.003043.

[122] S. Nilsson, E. Kristensson, M. Aldén, J. Bood, and A. Ehn, "Fluorescence lifetime imaging through scattering media," *Scientific Reports,* vol. 13, no. 1, p. 3066, 2023/02/21 2023, doi: 10.1038/s41598-023-30055-7.

[123] S. Taamallah, K. Vogiatzaki, F. M. Alzahrani, E. M. A. Mokheimer, M. A. Habib, and A. F. Ghoniem, "Fuel flexibility, stability and emissions in premixed hydrogen-rich gas turbine combustion: Technology, fundamentals, and numerical simulations," *Applied Energy,* vol. 154, pp. 1020-1047, 2015/09/15/ 2015, doi: https://doi.org/10.1016/j.apenergy.2015.04.044.

[124] W. Zhang *et al.*, "Effect of differential diffusion on turbulent lean premixed hydrogen enriched flames through structure analysis," *International Journal of Hydrogen Energy,* vol. 45, no. 18, pp. 10920-10931, 2020/04/01/ 2020, doi: https://doi.org/10.1016/j.ijhydene.2020.02.032.

[125] F. Pignatelli *et al.*, "Pilot impact on turbulent premixed methane/air and hydrogen-enriched methane/air flames in a laboratory-scale gas turbine model combustor," *International Journal of Hydrogen Energy,* vol. 47, no. 60, pp. 25404-25417, 2022/07/15/ 2022, doi: https://doi.org/10.1016/j.ijhydene.2022.05.282.

[126] R. W. Schefer, D. M. Wicksall, and A. K. Agrawal, "Combustion of hydrogen-enriched methane in a lean premixed swirl-stabilized burner," *Proceedings of the Combustion Institute,* vol. 29, no. 1, pp. 843-851, 2002/01/01/ 2002, doi: https://doi.org/10.1016/S1540-7489(02)80108-0.

[127] D. M. Wicksall, A. K. Agrawal, R. W. Schefer, and J. O. Keller, "Fuel Composition Effects on the Velocity Field in a Lean Premixed Swirl-Stabilized Combustor," 2003. [Online]. Available: https://doi.org/10.1115/GT2003-38712.

[128] IEA, "Energy Technology Perspectives 2023," IEA, https://www.iea.org/reports/energy-technology-perspectives-2023, 2023. [Online]. Available: https://www.iea.org/reports/energy-technology-perspectives-2023

[129] Y. Koç, H. Yağlı, A. Görgülü, and A. Koç, "Analysing the performance, fuel cost and emission parameters of the 50 MW simple and recuperative gas turbine cycles using natural gas and hydrogen as fuel," *International Journal of Hydrogen Energy,* vol. 45, no. 41, pp. 22138-22147, 2020/08/21/ 2020, doi: https://doi.org/10.1016/j.ijhydene.2020.05.267.

[130] J. M. Donbar, J. F. Driscoll, and C. D. Carter, "Reaction zone structure in turbulent nonpremixed jet flames—from CH-OH PLIF images," *Combustion and Flame,* vol. 122, no. 1, pp. 1-19, 2000/07/01/ 2000, doi: https://doi.org/10.1016/S0010-2180(00)00098-5.

[131] R. Sadanandan, M. Stöhr, and W. Meier, "Simultaneous OH-PLIF and PIV measurements in a gas turbine model combustor," *Applied Physics B,* vol. 90, no. 3, pp. 609-618, 2008/03/01 2008, doi: 10.1007/s00340-007-2928-8.

[132] L. Berger, A. Attili, and H. Pitsch, "Synergistic interactions of thermodiffusive instabilities and turbulence in lean hydrogen flames," *Combustion and Flame,* vol. 244, p. 112254, 2022/10/01/ 2022, doi: https://doi.org/10.1016/j.combustflame.2022.112254.

[133] A. Ehn, J. Zhu, X. Li, and J. Kiefer, "Advanced Laser-Based Techniques for Gas-Phase Diagnostics in Combustion and Aerospace Engineering," *Applied Spectroscopy,* vol. 71, no. 3, pp. 341-366, 2017/03/01 2017. [Online]. Available: https://opg.optica.org/as/abstract.cfm?URI=as-71-3-341.

[134] K. Suhling, P. M. French, and D. Phillips, "Time-resolved fluorescence microscopy," *Photochemical & Photobiological Sciences,* vol. 4, no. 1, pp. 13-22, 2005.

[135] K. Suhling *et al.*, "Fluorescence lifetime imaging (FLIM): Basic concepts and some recent developments," *Medical Photonics,* vol. 27, pp. 3-40, 2015/05/01/ 2015, doi: https://doi.org/10.1016/j.medpho.2014.12.001.

[136] A. Ehn, O. Johansson, J. Bood, A. Arvidsson, B. Li, and M. Aldén, "Fluorescence lifetime imaging in a flame," *Proceedings of the Combustion Institute,* vol. 33, no. 1, pp. 807-813, 2011/01/01/ 2011, doi: https://doi.org/10.1016/j.proci.2010.05.083.

[137] M. Hargather and G. Settles, "Recent Developments in Schlieren and Shadowgraphy," in *27th AIAA Aerodynamic Measurement Technology and Ground Testing Conference*, (Fluid Dynamics and Co-located Conferences: American Institute of Aeronautics and Astronautics, 2010.

[138] S. W. Allison and G. T. Gillies, "Remote thermometry with thermographic phosphors: Instrumentation and applications," *Review of Scientific Instruments,* vol. 68, no. 7, pp. 2615-2650, 1997, doi: 10.1063/1.1148174.

[139] William M. Yen, Shigeo Shionoya, and H. Yamamoto, S. S. William M. Yen, Hajime Yamamoto, Ed. *PHOSPHOR HANDBOOK*, 2nd ed. CRC Press laser and optical science and technology series: CRC Press, 2007.

[140] M. Aldén, A. Omrane, M. Richter, and G. Särner, "Thermographic phosphors for thermometry: A survey of combustion applications," *Progress in Energy and Combustion Science,* vol. 37, no. 4, pp. 422-461, 2011/08/01/ 2011, doi: https://doi.org/10.1016/j.pecs.2010.07.001.

[141] M. D. Chambers and D. R. Clarke, "Doped Oxides for High-Temperature Luminescence and Lifetime Thermometry," *Annual Review of Materials Research,* vol. 39, no. 1, pp. 325-359, 2009/08/01 2009, doi: 10.1146/annurev-matsci-112408-125237.

[142] J. Brübach, C. Pflitsch, A. Dreizler, and B. Atakan, "On surface temperature measurements with thermographic phosphors: A review," *Progress in Energy and Combustion Science,* vol. 39, no. 1, pp. 37-60, 2013/02/01/ 2013, doi: https://doi.org/10.1016/j.pecs.2012.06.001.

[143] S. W. Allison, D. L. Beshears, M. R. Cates, M. B. Scudiere, D. W. Shaw, and A. D. Ellis, "Luminescence of YAG:Dy and YAG:Dy,Er crystals to 1700 °C," *Measurement Science and Technology,* vol. 31, no. 4, p. 044001, 2020/01/06 2020, doi: 10.1088/1361-6501/ab4ebd.

[144] M. R. Cates, D. L. Beshears, S. W. Allison, and C. M. Simmons, "Phosphor thermometry at cryogenic temperatures," *Review of Scientific Instruments,* vol. 68, no. 6, pp. 2412-2417, 1997, doi: 10.1063/1.1148125.

[145] A. L. Heyes, "On the design of phosphors for high-temperature thermometry," *Journal of Luminescence,* vol. 129, no. 12, pp. 2004-2009, 2009/12/01/ 2009, doi: https://doi.org/10.1016/j.jlumin.2009.03.041.

[146] C. Knappe, J. Lindén, F. Abou Nada, M. Richter, and M. Aldén, "Investigation and compensation of the nonlinear response in photomultiplier tubes for quantitative single-shot measurements," *Review of Scientific Instruments,* vol. 83, no. 3, p. 034901, 2012, doi: 10.1063/1.3693618.

[147] J. Lindén, C. Knappe, M. Richter, and M. Aldén, "Limitations of ICCD detectors and optimized 2D phosphor thermometry," *Measurement Science and Technology,* vol. 23, no. 3, p. 035201, 2012/01/25 2012, doi: 10.1088/0957-0233/23/3/035201.

[148] C. Knappe, F. A. Nada, M. Richter, and M. Aldén, "Comparison of photo detectors and operating conditions for decay time determination in phosphor thermometry," *Review of Scientific Instruments,* vol. 83, no. 9, p. 094901, 2012, doi: 10.1063/1.4746990.

[149] F. Abou Nada, C. Knappe, M. Aldén, and M. Richter, "Improved measurement precision in decay time-based phosphor thermometry," *Applied Physics B,* vol. 122, no. 6, p. 170, 2016/06/01 2016, doi: 10.1007/s00340-016-6446-4.

[150] Ø. Persvik, T. B. Melø, and K. R. Naqvi, "Pulsed-source time-resolved phosphorimetry: comparison of a commercial gated photomultiplier with a specially wired ungated photomultiplier," *Photochemical & Photobiological Sciences,* vol. 12, no. 6, pp. 1110-1113, 2013.

[151] D. H. Hartman, "Pulse mode saturation properties of photomultiplier tubes," *Review of Scientific Instruments,* vol. 49, no. 8, pp. 1130-1133, 2008, doi: 10.1063/1.1135533.

[152] R. L. Vander Wal, P. A. Householder, and T. W. Wright, "Phosphor Thermometry in Combustion Applications," *Applied Spectroscopy,* vol. 53, no. 10, pp. 1251-1258, 1999/10/01 1999, doi: 10.1366/0003702991945498.

LUND
UNIVERSITY